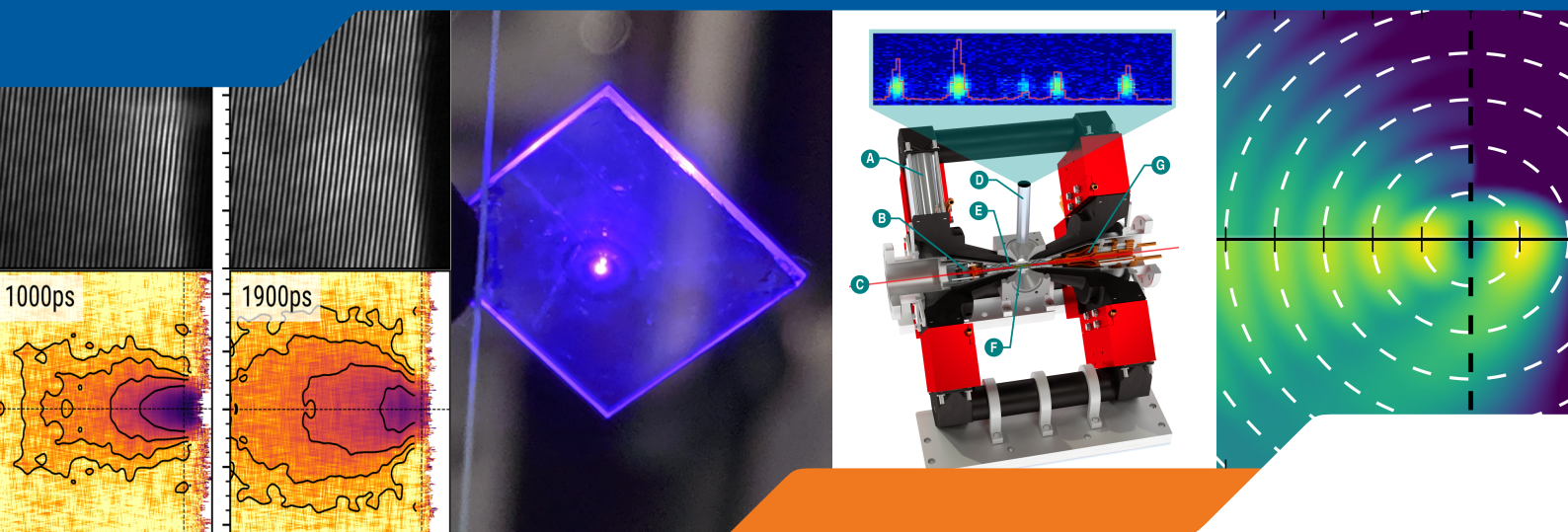


HI JENA

Helmholtz Institute Jena

ANNUAL REPORT 2019



FRIEDRICH-SCHILLER-
UNIVERSITÄT
JENA

HZDR
HELMHOLTZ ZENTRUM
DRESDEN ROSENDORF



Helmholtz Institute Jena

Annual Report 2019

Imprint

- Publisher:** Helmholtz-Institut Jena, Fröbelstieg 3, 07743 Jena, Germany
(<http://www.hi-jena.de>)
@ GSI Helmholtzzentrum für Schwerionenforschung GmbH
Darmstadt, Germany (<http://www.gsi.de>)
GSI is member of the Helmholtz association of national research
centers (<http://www.helmholtz.de>).
- Editors:** Daniel Seipt and Andrey Volotka
- DOI:** 10.15120/GSI-2020-00954 (<http://dx.doi.org/10.15120/GSI-2020-00954>)
- Publication date:** July 2020

The annual report 2019 of the Helmholtz-Institut Jena is licensed under the Creative Commons Attribution BY 4.0 (CC BY 4.0): <https://creativecommons.org/licenses/by/4.0/>

Contents

Foreword	11
Status of the Research School of Advanced Photon Science of the Helmholtz Institute Jena <i>R. Märtin, C. Hahn, Ch. Spielmann, G. Weber, and Th. Stöhlker</i>	13
High Power Laser Development	15
Generation of THz radiation from organic BNA crystals for plasma imaging <i>F. Roeder and A. Gopal</i>	16
ATHENA: An Ultra-High Temporal Contrast Frontend for PEnELOPE <i>M. Hornung, D. Albach, J. Hein, M. Hellwing, A. Kessler, M. Löser, F. Schorcht, M. Siebold, I. Tamer, U. Schramm and M. C. Kaluza</i>	17
Development and Characterization of a Cylindrical Offner-Stretcher <i>M. Hornung, I. Tamer, J. Hein, and M. C. Kaluza</i>	18
POLARIS: Towards Shorter Pulses and Improved Temporal Contrast <i>M. Hornung, I. Tamer, M. Hellwing, A. Kessler, J. Hein, and M. C. Kaluza</i> . . .	19
Post-CPA Pulse Compression using CR39 <i>I. Tamer, M. Hornung, L. Lukas, S. Keppler, M. Hellwing, R. Van Hull, J. Hein, M. Zepf, M. C. Kaluza</i>	20
Carrier-envelope phase stable few-cycle fiber laser system <i>E. Shestaev, D. Hoff, A. M. Saylor, A. Klenke, S. Hädrich, F. Just, T. Eidam, P. Jójárt, Z. Várallyay, K. Osvay, G. G. Paulus, A. Tünnermann, and J. Limpert</i> .	21
Generation of coherent broadband high photon flux continua in the XUV with a sub-two-cycle fiber laser <i>R. Klas, W. Eschen, A. Kirsche, J. Rothhardt, and J. Limpert</i>	22

Infrastructure upgrade at JETi200 Target Area I	
<i>A. Sävert, G. Schäfer, B. Beleites, F. Ronneberger, R. Große, H. Wöhl, and M. Zepf</i>	23
Commissioning of Target Area 2 at the JETI Laser	
<i>P. Hiltz, A. Sävert, T. Köhler, G. Schäfer, D. Klöpfel, Hendrik Wuerl, and M. Zepf</i>	24
108 W average power GW-level Tm-doped fiber CPA system	
<i>T. Heuermann, Z. Wang, M. Gebhardt, M. Lenski, C. Gaida, C. Jauregui, and J. Limpert</i>	25
Ultrafast lasers based on multi-pass post-compression	
<i>P. Balla, A. Bin Wahid, A. Schönberg, I. Hartl, C. M. Heyl</i>	26
Laser Particle Acceleration	29
NOPA-based Ultrashort Optical Probe Pulse for Laser-Plasma Interactions	
<i>I. Tamer, M. Hellwing, Y. Azamoum, M. Hornung, S. Keppler, F. Schorcht, J. Hein, and M. C. Kaluza</i>	30
Terahertz generation using two colour plasma filament	
<i>T. Kawde, S. Popruzhenko, G. G. Paulus, and A. Gopal</i>	31
A flexible X-ray source with tunable polarization and orbital angular momentum from Hermite-Gaussian laser modes driven plasma channel wakefields	
<i>B. Lei, T. Teter, J. Wang, M. Zepf, and S. G. Rykovanov</i>	32
Few-Cycle Microscopy of Stimulated Raman Side Scattering (SRSS) in a Laser Wakefield Accelerator	
<i>C. Zepf, A. Sävert, A. Seidel, M. Zepf, and M. C. Kaluza</i>	33
Detecting multi 100 MeV Electron Positron Pairs from Quantum Vacuum on Photon-Photon collision experiments at Astra Gemini	
<i>D. Hollatz, G. M. Samarin, E. Gerstmayr, B. Kettle, F. Salgado, S. P. Mangles, and M. Zepf</i>	34
Single Shot 1D Space-Time Resolved Transmission Diagnostic for Probing Relativistic Laser-Plasma Interaction	
<i>Y. Azamoum, G. A. Becker, S. Keppler, I. Tamer, M. Hornung, M. Hellwing, F. Schorcht, and M. C. Kaluza</i>	35
Establishment of a dedicated plasma characterization laboratory	
<i>S. Keppler, M. Hellwing, F. Schorcht, M. Mäusezahl, T. Weickhardt, M. Beyer, M. Nolte, J. Margraf, and M. C. Kaluza</i>	36

Intensity scaling limitations of laser proton acceleration in the TNSA-regime <i>S. Keppler, N. Elkina, G. A. Becker, J. Hein, M. Hellwing, M. Hornung, M. Mäusezahl, C. Rödel, F. Schorcht, I. Tamer, M. Zepf, and M. C. Kaluza</i>	37
Simulations on ion acceleration in laser-driven foam-like plasma targets <i>B. Liu and M. Zepf</i>	38
Single Particle Detection System for the Strong-Field QED Experiment (E-320) at FACET-II <i>F. Salgado, Harsh, S. Meuren, C. Nielsen, D. Reis, C. Rödel, W. Ziegler, and M. Zepf</i>	39
Photon and Particle Spectroscopy	41
X-ray polarimetry with artificial four bounces diamond channel cuts <i>H. Bernhardt, A. T. Schmitt, B. Grabiger, B. Marx-Glowna, R. Löttsch, H. C. Wille, D. Bessas, A. I. Chumakov, R. Ruffer, R. Roehlsberger, Th. Stöhlker, I. Uschmann, G. G. Paulus, and K. S. Schulze</i>	42
S-EBIT Facility: status report <i>S. Trotsenko, T. Morgenroth, O. Herdrich, F. Kröger, A. Gumberidze, G. Weber, A. Fleischmann, D. Hengstler, S. Allgeier, Ch. Enss, R. Schuch and Th. Stöhlker</i>	43
A high-photon-flux narrow bandwidth XUV source for experiments at ion storage rings <i>V. Hilbert, M. Tschernajew, R. Klas, H. Lin, P. Gierschke, J. Limpert, J. Rothhardt</i>	44
New Setup for X-Ray Spectroscopy at the CRYRING@ESR Electron Cooler <i>F. M. Kröger, G. Weber, O. Forstner, A. Gumberidze, M. O. Herdrich, M. Lestinsky, A. Kalinin, Th. Köhler, E. Menz, P. Pfäfflein, U. Spillmann, and Th. Stöhlker</i>	45
Resonant photoexcitation of highly charged ions at synchrotron light sources with the compact electron beam ion trap PolarX-EBIT <i>S. Bernitt, S. Kühn, R. Steinbrügge, C. Shah, P. Micke, M. Togawa, J. Stierhof, M. Leutenegger, N. Hell, G. V. Brown, J. R. Crespo López-Urrutia, and Th. Stöhlker</i>	46
Characterization of a YAP:Ce scintillator for ion detection <i>B. Zhu, P. Pfäfflein, C. Hahn, H. Lin, G. Weber, and Th. Stöhlker</i>	47
Phase-volume Effect for Few-cycle Light-matter Interactions <i>Y. Zhang, D. Zille, D. Hoff, P. Wustelt, D. Würzler, M. Möller, A. M. Saylor, and G. G. Paulus</i>	48
XUV source diagnostics with a single diffraction pattern <i>F. Tuitje, T. Helk, A. Dehlinger, H. Stiel and C. Spielmann</i>	49

Strong-field physics with phase-stable mid-IR pulses	
<i>M. Kübel, S. Skruszewicz, P. Wustelt, Y. Zhang, D. Hoff, D. Würzler, A. M. Sayler R. Hollinger, C. Spielmann, and G. G. Paulus</i>	50
Ultrafast Laser-Induced Fragmentation of Molecular Ion Beam Targets with a High-Repetition-Rate Laser Source	
<i>B. Ying, P. Wustelt, M. Kübel, A. M. Sayler, Th. Stöhlker, and G. G. Paulus</i>	51
Role of free carriers in the absorption of intense long wavelength light	
<i>R. Hollinger, E. Haddad, M. Zapf, R. Röder, I. Uschmann, M. Zürich, D. Kartashov, F. Légaré, C. Ronning, C. Spielmann</i>	52
Improving the contrast of ghost image based on the speckles' histogram	
<i>Z. Sun, F. Tuitje, and C. Spielmann</i>	53
Storage of Highly Charged Ions for Non-Linear Laser Experiments at the HILITE Penning Trap	
<i>M. Kiffer, S. Ringleb, N. Stallkamp, B. Arndt, S. Kumar, G. G. Paulus, W. Quint, B. Reich, Th. Stöhlker, and M. Vogel</i>	54
X-ray and particle emission from titanium foils irradiated by ultra-relativistic near-infrared ultrashort laser pulses	
<i>E. Eftekhari Zadeh, R. Löttsch, L. Manganelli, S. Blümke, D. Kartashov, I. Uschmann, O. Rosmej, C. Spielmann</i>	55
Extreme ultraviolet interferometry for artefact-free coherence tomography driven by a high-harmonic source	
<i>J. Nathanael, S. Fuchs, M. Wiünsche, J. J. Abel, J. Reinhard, F. Wiesner, C. Rödel, and G. G. Paulus</i>	56
High Density Ion Beam Targets for Ultrafast Laser-Induced Processes using High Brightness Ion Sources	
<i>F. Machalett, P. Wustelt, V. Huth, T. Weber, Th. Stöhlker, and G.G. Paulus</i>	57
Setup for a study on the polarization transfer in elastic scattering of hard x-rays	
<i>W. Middents, G. Weber, M. Vockert, U. Spillmann, A. Volotka, and Th. Stöhlker</i>	58
Detector support frames for the 1s Lamb shift study at CRYRING@ESR	
<i>P. Pfäfflein, M. O. Herdrich, T. Köhler, G. Weber, and Th. Stöhlker</i>	59
Energy resolution of maXs, a metallic magnetic micro-calorimeter	
<i>P. Pfäfflein, M. O. Herdrich, J. Geist, D. Hengstler, A. Fleischmann, G. Weber, C. Enss, and Th. Stöhlker</i>	60
Commissioning of a SiPM-based ion detector for CRYRING@ESR	
<i>G. Weber, A. Borovik Jr., V. Hilbert, H. Lin, P. Pfäfflein, B. Zhu, C. Hahn, M. Lestinsky, S. Schippers, J. Rothhardt, and Th. Stöhlker</i>	61

First measurements of a new type of Coreless Cryogenic Current Comparators (4C) for non-destructive intensity diagnostics of charged particles <i>V. Tympel, Th. Stöhlker, J. Tan, H. De Gerssem, N. Marsic, W. Müller, D. Haider, M. Schwickert, T. Sieber, J. Golm, M. Stapelfeld, F. Schmidl, P. Seidel, M. Schmelz, R. Stolz, T. Schönau, S. Anders, J. Kunert, and V. Zakosarenk</i>	62
Analysis of Fe X-Ray Spectra from the S-EBIT-I taken with a maXs-30 Detector <i>M. O. Herdrich, A. Fleischmann, D. Hengstler, C. Enss, S. Trotsenko, T. Morgenroth, R. Schuch, G. Weber, and Th. Stöhlker</i>	63
Theory	65
Elastic Photon Scattering on Hydrogenic Atoms Near Resonances <i>D. Samoilenko, A. V. Volotka, and S. Fritzsche</i>	66
Characterization of opening angle correlations of a biphoton state decomposed in Bessel modes <i>B. Baghdasaryan, F. Steinlechner, and S. Fritzsche</i>	67
Polarization-dependent high-intensity Kapitza-Dirac effect in strong laser fields <i>B. Böning, W. Paufler, and S. Fritzsche</i>	68
All-Loop Result for the Strong Magnetic Field Limit of the Heisenberg-Euler Effective Lagrangian <i>F. Karbstein</i>	69
Boosting Quantum Vacuum Signatures by Coherent Harmonic Focusing <i>F. Karbstein, A. Blinne, H. Gies, and M. Zepf</i>	70
X-ray photon scattering at a focused high-intensity laser beam <i>F. Karbstein and E. A. Mosman</i>	71
Breakdown of the electric dipole approximation in direct two-photon ionization <i>J. Hofbrucker, A. V. Volotka, and S. Fritzsche</i>	72
Optimized Chirped Laser Pulses for Narrowband Inverse Compton Sources in the High-Intensity Regime <i>D. Seipt, V. Yu. Kharin, and S. G. Rykovanov</i>	73
Propagation effects in multipass HHG from plasma surfaces <i>S. Tietze, M. Zepf, and M. Yeung</i>	74
Propagator from Nonperturbative Worldline Dynamics <i>S. Franchino-Viñas and H. Gies</i>	75

Ponderomotive Scattering of Electrons for High-Intensity Laser Pulse Characterization	
<i>T. Teter, D. Seipt, and M. Zepf</i>	76
Two-photon sequential ionization of atoms by twisted- and plane-wave light	
<i>V. P. Kosheleva, V. A. Zaytsev, R. A. Müller, A. Surzhykov, and S. Fritzsche</i> . . .	77
Publications	79
Theses	95

Foreword

Dear friends and members of the Helmholtz Institute Jena,

The Helmholtz Institute Jena was founded more than 10 years ago as an institute of GSI Darmstadt on the campus of the Friedrich Schiller University (FSU), with the University of Jena and the Helmholtz centers DESY and HZDR as additional partners. It combines established scientific expertise of the university and of our partners with the strategic mission of GSI.

The institute's mission is excellence in fundamental and applied research based on high-power lasers, particle accelerators, and x-ray science. In the pursuit of this, it addresses the coupling of intense light with matter, and conducts various research and development efforts of advanced instrumentation for dedicated experiments at the flagship facilities for extreme matter research, the EU-XFEL at Hamburg and the international FAIR project at Darmstadt. Indeed, during the last 10 years a multitude of research highlights has been achieved and substantial progress has been reported related to the development of novel instrumentation for the realm of x-ray science and research into extreme states of matter. This scientific excellence has been proven in 2018 by the scientific center evaluation of GSI in the framework of the Helmholtz Association, where all scientific activities of the Helmholtz Institute Jena have been rated as "outstanding".

Key to this success are the young researchers, postdocs and PhD students, who are actively engaged in research and the close cooperation with our partners, in particular the colleagues from the University of Jena. In this context, one must highlight the important role of the world-renowned experts, Prof. Dr. Matt Zepf for the field of relativistic plasma physics and Prof. Dr. Stephan Fritzsche for the theory of the dynamics of electrons and strong fields, who both could be attracted for joint professor positions at the Helmholtz Institute and the FSU Jena. Their research expertise and engagement has strongly influenced the scientific program and activities during the recent years. Finally, in 2019, HI Jena was able to attract Prof. Dr. Ralf Röhlsberger for the still vacant W3 position "x-ray science", whose expertise and research group further strengthen the research portfolio of the institute. For the latter purpose an important prerequisite is additional laboratory and office space, considering the institute's continuous growth over the years to currently about 100 scientists, including PhD students and supporting personnel. In this regard, essential progress has been achieved in 2019.

In October 2019, the "Spatenstich" for the new, additional institute building, financed by the Federal State of Thuringia (8 M€), took place. The new building is located at the campus of the FSU Jena in direct neighborhood to the institute building at Fröbelstieg 3. The civil construction will start in March 2020 and it is expected that the building will be available for occupancy in 2022. With the additional institute building, which directly connects to the target laboratories in the basement of the existing institute building, the infrastructural conditions for cutting-edge research will be further improved.



“Spatenstich” for the extension building of the HI Jena in October 2019.

2019 was also a very important year with respect to the strategic developments at Helmholtz, which were characterized by the preparation of the upcoming strategic evaluation of the research field “Matter”, which HI Jena is part of. The subject of the evaluation are the research goals and central research topics of the research field in the context of the next funding period POF IV (2021–2027).

With this Annual Report for 2019, we present an overview on the accomplishments in science and technology made at the institute over the last year. Various research highlights have been achieved using the institute’s own experimental facilities at Jena (the high-power lasers POLARIS and JETi200), the ion storage rings and the PHELIX laser at GSI campus Darmstadt, the photon facilities at DESY as well as the facilities of collaborative partners.

Finally, a particularly important task of HI Jena is the education and promotion of the next generation of scientists with a focus on the physics of matter in extreme states. Meanwhile a structured PhD education program, including both scientific and soft-skills training adapted to the research profile and organizational structure of the institute, is well established within the framework of the “Research School of Advanced Photon Science” (RS-APS). The school interacts closely with the GSI Graduate School HGS-HIRE as well as with the local Graduate Schools at FSU Jena under the umbrella of the Graduate Academy of the university. Many students make use of the benefits offered by the research school, e.g. most students regularly use the personal travel money offered to attend conferences to present their own research work. The Research School has now close to 60 participating doctoral students, of whom more than 50 % are financed via 3rd party funding. In the future, RS-APS will further increase its efforts to foster the exchange of PhD students with our research partners located at other institutes in Germany and abroad.

Status of the Research School of Advanced Photon Science of the Helmholtz Institute Jena

R. Märtin¹, C. Hahn^{1,2}, Ch. Spielmann^{1,2}, G. Weber¹, and Th. Stöhlker^{1,2,3}

¹HI-Jena, Jena, Germany; ²University Jena, Jena, Germany; ³GSI, Darmstadt, Germany

Since 2012 all PhD students associated with the Helmholtz Institute Jena and its research mission are supported by the Research School of Advanced Photon Science (RS-APS) of the Helmholtz Institute Jena part of Helmholtz Center GSI Darmstadt at the Campus of the FSU Jena with the university, and DESY and HZDR as additional partners. Although there were already existing PhD programs at the Helmholtz partner centers, there was the need for a dedicated local structured PhD education programme, prompted by both the distance of the Friedrich Schiller University from GSI and the specific research focus at the interface of optics, lasers and accelerator technology.

Since its foundation in 2012 the number of students participating in RS-APS has steadily increased. In the year 2019 almost 60 students working directly at the institute or the partner centers GSI, DESY or HZDR took part in the programme of the school. More than half of the students is third party funded, while the rest of the doctoral students either receive a scholarship or have a doctoral position supported by the Helmholtz Institute Jena. In addition every participant has its own annual travel allowance to visit conferences and workshops. The offered travel budget is of great importance for the professional and international network of the future researchers and most of the students take advantage of their yearly budget.

The financial support is among other things an incentive to participate actively in the academic and soft skill program offered by the research school of the Helmholtz Institute Jena and its collaborating partners, the HGS-HIRE Graduate School for FAIR and the Graduate Academy of the FSU Jena.

Together with HGS-HIRE, RS-APS has been organizing annual Lecture Weeks for seven years. In 2019 the Lecture Week addressed various photon imaging techniques available from the optical to the XUV regime. Hosted by the “Kloster Hardehausen” with its stimulating atmosphere, Christian Eggeling (FSU Jena), Tatiana Latychevskaia (PSI, Switzerland), Gerd Schneider (HZ Berlin), Silvio Fuchs (HI Jena) and the participating students discussed together various aspects of this crossdisciplinary topic.

The internationalization of the school is developing well, with now 44% of the doctoral students having non-German citizenship. The percentage of female members of our research school increased to 12%, from 5% in 2018. Ten members of the Graduate School successfully completed their doctoral studies in 2019.



Figure 1: The participants of the seventh joint Lecture Week of HGS-HIRE and RS-APS in Kloster Hardehausen.

High Power Laser Development

Generation of THz radiation from organic BNA crystals for plasma imaging

F. Roeder^{1,2} and A. Gopal^{1,2}

¹Institut für Optik und Quantenelektronik, Physikalisch-Astronomische Fakultät, Friedrich-Schiller-Universität, 07743 Jena, Germany; ²Helmholtz Institute Jena, 07743 Jena, Germany

We report on our studies on THz generation process in organic N-benzyl-2-methyl-4-nitroaniline (BNA) via optical rectification (OR). The generated radiation will be employed for the characterization of optical window materials, nonlinear spectroscopy and imaging of low density plasmas with an aim to visualize wake fields at the AWAKE project at CERN.

THz radiation was generated by OR of a laser pulse with a central wavelength centered around 800 nm in an organic BNA crystal. Even though conversion efficiencies from optical to THz up to 0.2% have been observed at wavelengths longer than 800 nm [1] no systematic work has been reported on the performance of these crystals at Ti:Saph wavelengths which is the workhorse of standard university scale laboratories. At first, the influence of the incident pump laser fluence on THz generation in the BNA crystal was investigated. The results shows that the maximum fluence at room temperature for optimum THz yield is around 10.5 mJ/cm^2 . While the complex electric field of the THz pulse measured with a $500 \mu\text{m}$ thick ZnTe crystal in the spatially resolved electro-optic (EO) detection scheme showed that the THz pulses have a temporal duration of 500 fs with mexican hat like feature and with spectral components ranging from 0.5 to 2.5 THz.

To investigate the transmission of different window materials used in plasma accelerators, THz beamlines and at FELs, they were placed in the collimated THz beam. Temporal and spectral changes of the transmitted THz pulse were recoded using the EO scheme as depicted in Figure 1. The transmitted THz spectra through dif-

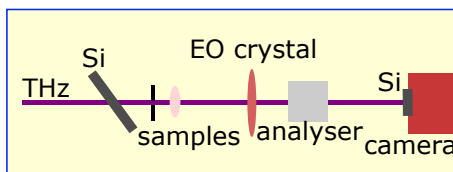


Figure 1: Schematic experimental setup to determine THz transmission through different window material samples.

ferent window materials is shown in Fig. 2. We tested both mounted and unmounted sapphire which showed the similar absorption patterns at higher frequencies. A polycarbonate window which is suitable as a shock proof outer material in beamline shows strong spectral absorption. These findings forced us to test alternative options such as highly durable and resistant diamond as a window material. While employing a diamond window

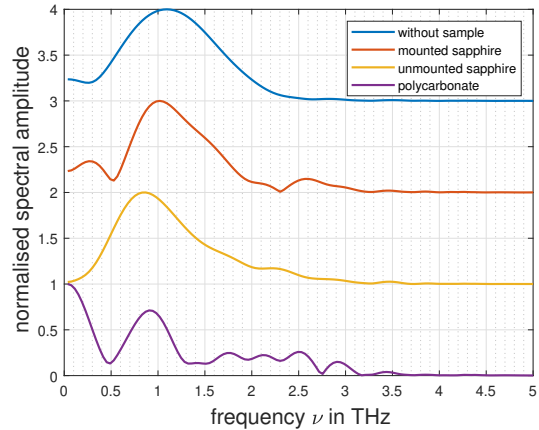


Figure 2: Normalised transmission spectra of THz radiation through different samples.

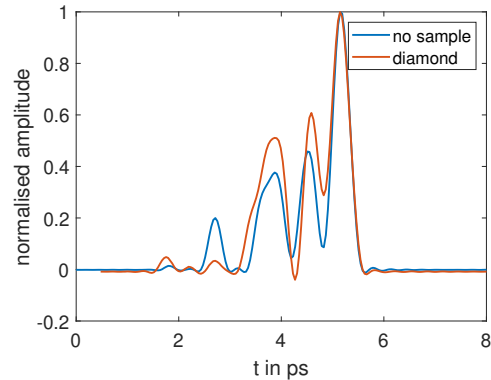


Figure 3: Temporal profile of the normalised THz field amplitude without a sample (blue) and after the diamond window (red) shifted in time.

shows less dispersion and Subsequent measurements show (Figure 3), that there significantly lower dispersion of the THz pulse compared to other window materials. Diamond therefore stands out as a window material transmitting the THz beam undisturbed, which is needed for imaging applications requiring good temporal resolution.

References

- [1] M. Shalaby et al., Opt. Lett. **41**, pp. 1777-1780 (2016).

ATHENA: An Ultra-High Temporal Contrast Frontend for PEnELOPE

M. Hornung^{1,2,#}, D. Albach³, J. Hein^{1,2}, M. Hellwing², A. Kessler¹, M. Löser³, F. Schorcht¹, M. Siebold³, I. Tamer¹, U. Schramm³ and M. C. Kaluza^{1,2}

¹Helmholtz Institute Jena, Germany; ²Institute of Optics and Quantum Electronics, FSU Jena, Germany, ³Helmholtz Center Dresden-Rossendorf, Germany

We present the status of the development of an ultra-high temporal contrast frontend for 1 mJ laser pulses at a center wavelength of 1033 nm. The frontend is intended to be delivered and used for temporal contrast enhancement at the PEnELOPE laser facility (Helmholtz Center Dresden-Rossendorf, HZDR).

Within the ATHENA (Accelerator Technology HELmholtz iNfrAstructure) project a frontend [1] is designed and built for the PEnELOPE laser system [2] based on the current POLARIS frontend. The basic parameters were fixed in cooperation with HZDR to meet the requirements of the PEnELOPE laser system to enhance the temporal contrast. The frontend laser system (FE) is currently under construction and should deliver sub-100 fs pulses at a center wavelength of 1033 nm and a pulse energy of up to 1 mJ. As one of the most important parameters the temporal pulse contrast should be as high as possible (e.g. for ASE better 10^{12}) and the pulses should be generated as far as possible without additional pre- and post-pulses. Furthermore, the system should fit into PEnELOPE's technical architecture (e.g. trigger, space, electronics, vacuum, ...) for ease of implementation and operation.

The FE architecture is based on the CPA concept and consists of an oscillator, stretcher, amplifier and pulse compressor. Finally, the pulses which were amplified by the CPA system are generating new high-contrast pulses in-between two crossed polarizers with use of the XPW process [1]. The CPA system is fully operational already whereas the XPW system is still under construction. The oscillator (Flint, LightConversion) delivers laser pulses with 60 nJ pulse energy and a repetition rate of 76 MHz. The repetition rate is reduced to 1 Hz with a Pockels-cell and polarizer system and the pulse are stretched from 80 fs to 55 ps with a spherical Offner-type stretcher. The stretcher was designed to support flexibility with spherical and cylindrical telescope optics as well as different line densities for the gratings with high mechanical accuracy. The stretching ratio and therewith the stretched pulse duration could be changed between 150 ps and 0.1 ps (zero-

dispersion) by stepper motors for the virtual grating separation and the desired diffraction angle. The corresponding compressor system and the pulse stretcher use gold gratings with a line density of 1480 l/mm. The compressor is able to compress laser pulses with more than 10 mJ.

The amplifier for the FE is based on the POLARIS amplifiers 1 and 2 (A1, A2 [3]) and is currently operating with pulse energies up to 4 mJ. The compressed pulse duration was measured with a SPIDER to 150 fs and a spectral bandwidth of 10 nm (FWHM). The temporal contrast of the compressed pulses is shown in Figure 1 measured with a THG-cross-correlator.

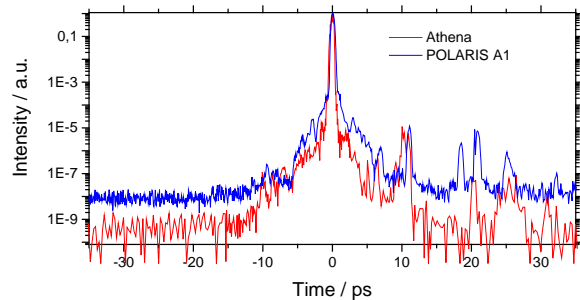


Figure 1: Temporal contrast measurement (measured with Sequoia, Amplitude Technologies) of the newly developed frontend in comparison to the existing POLARIS frontend (both without XPW, detection limit at $1E-9$).

Compared to the pulses from the original and currently used POLARIS frontend (blue curve in Fig. 1) the ASE-level is improved by one order of magnitude and the rising edge of the laser pulses is slightly better. This report presents an intermediate status of the development, the temporal contrast and the temporal pulse quality will be further increased with the XPW system in the near future.

References

- [1] H. Liebetrau et al., *OE* **22**, 20, p. 24776 (2014).
- [2] D. Albach et al., *HPLSE* **7**, e1 (2019).
- [3] M. Hornung et al., *OL*, **41**, 22, pp. 5413-5416 (2016).

[#]M.Hornung@gsi.de

Development and Characterization of a Cylindrical Offner-Stretcher

M. Hornung^{1,2,#}, I. Tamer¹, J. Hein^{1,2} and M. C. Kaluza^{1,2}

¹Helmholtz Institute Jena, Germany; ²Institute of Optics and Quantum Electronics, FSU Jena, Germany

We show first measurements of a newly developed Offner-type CPA-pulse stretcher facilitating a cylindrical Offner telescope. Within this project the optical performance of a cylindrical Offner stretcher (COS) is theoretically and experimentally compared to a pulse stretcher using a spherical Offner telescope.

The temporal rising edge (RE) of CPA generated high intensity laser pulses is currently an object of research. Sophisticated laser-matter experiments are requiring temporal clean laser pulses, most importantly with a RE as steep as possible (c.f. Fig. 1) to avoid unwanted pre-ionization of the targets. One suspected candidate for deteriorating the temporal rising edge are phase-amplitude couplings of far-field stretcher optics [1,2]. Compared to a spherical Offner stretcher (SOS) a COS avoids the usage of such far-field optics. In order to further increase the experimental performance of the POLARIS laser pulses [3] we investigate the feasibility of a COS. As soon as a COS is a promising candidate to optimize the RE we have set up a separate CPA system generating laser pulses with 150 fs pulse duration and multi-mJ pulse energies. Within the used Offner stretcher we have the capability to change between spherical and cylindrical Offner-telescopes while keeping all other parameters comparable and as constant as possible.

This report represents an intermediate status of the project where the measurements of the temporal intensity contrast of the SOS and COS amplified pulses are shown in Fig. 1. Clearly visible and contrary to expectations, the RE of the COS pulses is slightly worse compared to the SOS pulses.

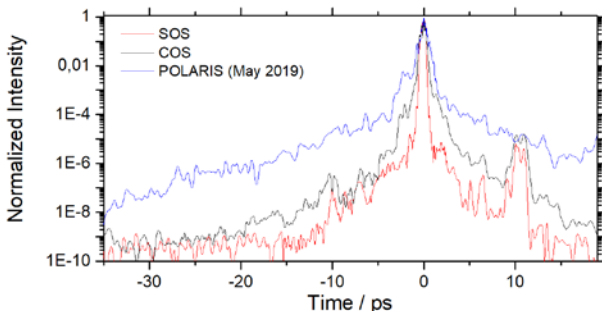


Figure 1: Temporal contrast measurements using different Offner-telescopes: SOS = spherical Offner (red), COS = cylindrical Offner (black) and for comparison POLARIS A2-amplified pulses in blue (detection limit at 1E-9).

[#]M.Hornung@gsi.de

As far as we know, this slightly worse, and so far still not improved, RE is explained by non-compensated spectral phase aberrations originating from the surface errors of the used stretcher and cylindrical optics. This hypothesis is supported by measurements of the spectral phase and temporal structure of the compressed pulses shown in Fig. 2.

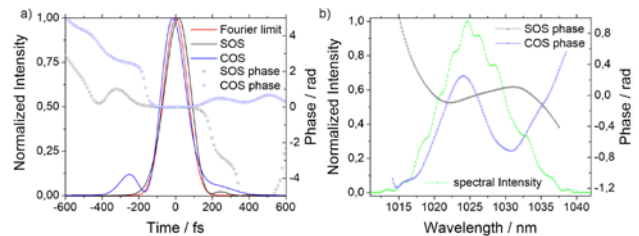


Figure 2: Temporal and spectral characterization of the SOS and COS amplified pulses. a) Temporal pulse shape and corresponding phase. b) Spectral intensity distribution and corresponding spectral phase.

As seen in Fig. 2 the spectral phase and hence the temporal pulse shape of the COS amplified pulses is deteriorated compared to the SOS amplified pulses and ideal compressed pulses (Fourier transform limited). Due to the different aspect ratios of the cylindrical optics (1:10) compared to the spherical optics (6:10) the surface quality of the COS-optics is slightly worse due to the challenging manufacturing process. This leads, in connection with more stringent alignment tolerances, to an, even on a linear scale visible, time structure which degrades the temporal pulse shape and the RE of these laser pulses.

In order to further improve the setup and most likely to demonstrate a beneficial operation with an improved RE of the laser pulses with a cylindrical Offner stretcher we will implement an acousto-optic modulator (Dazzler, Fastlite). The Dazzler is intended to compensate for the residual spectral phase aberrations and a direct comparison of SOS vs. COS stretched pulses with respect to the RE in the demonstrated setup should be feasible.

References

- [1] V.A. Schanz et al., JOSA A **36**, 10, (2019).
- [2] J. Bromage et al., CLEO, San Jose CA, p. 1-2, (2012).
- [3] M. Hornung et al., OL, **41**, 22, pp. 5413-5416 (2016).

POLARIS: Towards Shorter Pulses and Improved Temporal Contrast

M. Hornung^{1,2,#}, I. Tamer¹, M. Hellwing², A. Kessler², J. Hein^{1,2} and M. C. Kaluza^{1,2}

¹Helmholtz Institute Jena, Germany; ²Institute of Optics and Quantum Electronics, FSU Jena, Germany

Within this project the performance of the POLARIS laser pulses will be optimized with respect to the pulse duration and the temporal contrast, especially the rising edge of the pulses.

The POLARIS laser [1] is continuously used for HI Jena's laser particle acceleration program. Since sophisticated experiments do not only require high intensity laser pulses but also pulses with a very high temporal contrast a plasma mirror is used to enhance the contrast and here especially the rising edge of the laser pulses. A measurement of POLARIS's laser pulse contrast without plasma-mirror is shown in Figure 1. The black curve shows a measurement of the nanosecond-CPA system with a frontend amplifier A2 and the blue curve a measurement with all amplifiers up to the fifth stage A5. Comparing these measure-

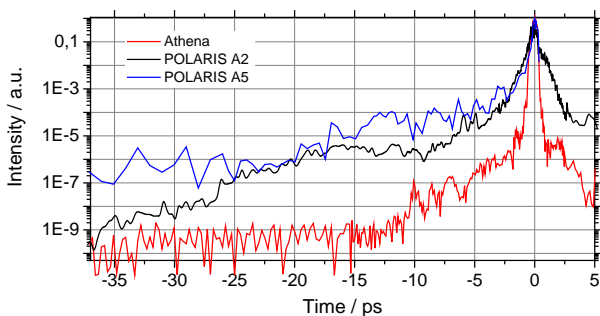


Figure 1: Temporal contrast measurements of POLARIS A2-amplified pulses in black and A5-amplified pulses in blue. The red curve shows a measurement of the newly developed PENELOPE frontend (detection limit at 1E-9).

ments to the red curve, which shows a measurement of the newly developed PENELOPE frontend (cf. this annual report) within the ATHENA project reveals huge potential for improvement. Furthermore, since the spectral bandwidth of the POLARIS laser was enhanced in 2016 from formerly 10-15 nm FWHM to 20-25 nm FWHM with tunable spectral filters [2] the compressed pulses are not Fourier-limited. With fully amplified pulses a bandwidth exceeding 23 nm FWHM could be shown [2], but the compressed minimal pulse duration is still around 100 fs FWHM, which is 20-25 fs too long and also manifests itself in the limited quality of the rising edge of the laser pulses.

To improve the aforementioned facts a couple of components and measurement methods were developed with respect to the experimental operation of POLARIS, which means that the laser system itself must not be used for the characterization and optimization. An active stretcher and a monolithic pulse compressor (without a tiled-grating array) for the compression of 1.5 ns-stretched pulses were constructed and commissioned. Both devices are basically identical to the POLARIS devices and can be used as a testbed since they are not necessary, but can be fully implemented in the POLARIS architecture with only some flip-mirrors. Using this stretcher-compressor system and searching dedicated for spectral-phase aberrations reveals multifold limiting components which are in sum far beyond the phase-compensation capability of the used acousto-optic modulator (DAZZLER). In parallel to the above mentioned active stretcher-compressor system an alternative CPA laser within the framework of the Helmholtz ATHENA project was constructed and commissioned (cf. this annual report). This very flexible system serves as an on-site measurement and testbed system during experimental operation of POLARIS. As mentioned before a variety of components (e.g. wavelength couplers, TFP's, stretcher telescope optics, ...) with non-ideal spectral-phase properties were localized and characterized. The procedure of optimizing these components with respect to the spectral phase is still ongoing. An optimized Offner telescope for the pulse stretcher was ordered and will be installed and tested in 2020. Due to currently enhanced manufacturing capabilities the stray light behavior is most likely enhanced for this optics. Finally, if broad-bandwidth pulses with a flat spectral phase and an improved temporal contrast are shown with the active stretcher and the monolithic nanosecond compressor system, this project will result in the permanent use of the active stretcher and the exchange of the tiled-grating array used in the POLARIS pulse compressor with a monolithic grating which was ordered and will be delivered in the future.

References

- [1] M. Hornung et al., OL, **41**, 22, pp. 5413-5416 (2016).
- [2] S. Keppler et al., OL **41**, 20, p. 4708 (2016).

#M.Hornung@gsi.de

Post-CPA Pulse Compression using CR39

*I. Tamer^{1,2}, M. Hornung^{1,2}, L. Lukas², S. Keppler^{1,2}, M. Hellwing²,
R. Van Hull², J. Hein^{1,2}, M. Zepf^{1,2}, M.C. Kaluza^{1,2}*

¹Helmholtz-Institute Jena, Germany; ²Institute of Optics and Quantum Electronics, Jena, Germany.

An optimization of the POLARIS [1] laser system towards higher laser pulse peak powers – in addition to the installation of a unique optical probing system [2] – is necessary for ongoing and upcoming investigations on laser-based ion acceleration regimes such as Target Normal Sheath Acceleration (TNSA) and Radiation Pressure Acceleration (RPA) at the Helmholtz-Institute Jena. Due to the spectral acceptance of the operational CPA system and the limiting laser-induced damage threshold (LIDT) of the active materials, an improvement in the peak power is often accomplished solely via an increase of the laser pulse energy, following a costly aperture scaling of the back-end of the laser system. However, the high transport intensities – in excess of 1 TW/cm^2 – achieved by the POLARIS laser pulse may now enable an additional method to enhance the peak power, without requiring modifications to the existing CPA system. Here, even in the near field [3], self-phase modulation (SPM) can be employed within a thin, highly nonlinear material after the CPA chain to significantly broaden the spectral bandwidth and allow for further pulse compression with, e.g., a chirped mirror pair.

Numerical simulations of the post-CPA pulse compression technique with the POLARIS laser pulse indicate that a pulse duration shortening by a factor of 3 – corresponding to an increase in the laser pulse peak power at POLARIS by the same factor – in a single-pass setup would require a 1 mm thick, transparent material with a nonlinear refractive index $n_2 \geq 6 \times 10^{-7} \text{ cm}^2/\text{GW}$. Using degenerate four-wave-mixing and a broadband spectrophotometer, the nonlinear refractive indices and optical transmission of multiple nonlinear samples – allyl diglycol carbonate (CR39), polyethylene terephthalate (amorphous PET), polymethyl methacrylate (PMMA), and cellulose acetate (CA) – were characterized [4], with the results summarized in Table 1. While the nonlinear refractive index n_2 of PET exceeds that of the other designated materials, the relatively high absorption hinders its use within the post-CPA pulse compression technique for the joule-class POLARIS laser pulses. Here, the thermally induced material deformation would lead to spatially inhomogeneous spectral and temporal profiles that worsen with each subsequent laser pulse.

For the post-CPA pulse compression technique, CR39 was selected as the optimal material, due to its combination of a high n_2 and near-zero absorption ($18\times$ lower than that of PET). In a proof-of-principle test, a single 1 mm CR39

Table 1: Relevant material properties ($\lambda = 1030 \text{ nm}$)

Material	CR39	PET	PMMA	CA
Refractive index n	1.495	1.551	1.483	1.470
$ n_2 [\times 10^{-7} \frac{\text{cm}^2}{\text{GW}}]$	6.24	13.10	5.13	5.85
Absorption A	0.04%	0.73%	0.03%	3.64%

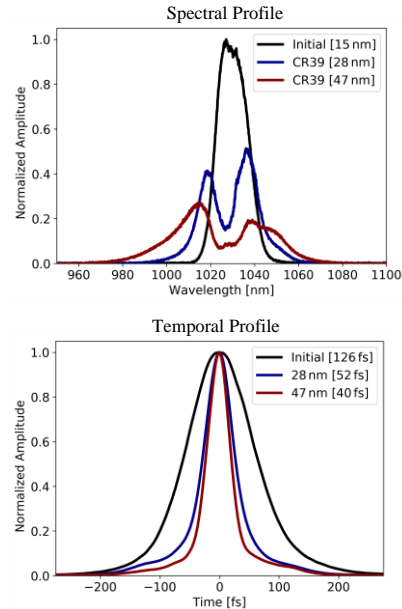


Figure 1: Spectral (top) and temporal (bottom) profiles before (black) and after post-CPA pulse compression in 1 mm CR39 at 1 TW/cm^2 (blue) and 2 TW/cm^2 (red).

sample was placed directly in the optical path of the POLARIS laser pulse after the 1st CPA. As seen in Fig. 1, the near field SPM induced within the transparent nonlinear material using intensities of 1 and 2 TW/cm^2 , adjusted via the beam radius, resulted in a doubling and tripling of the spectral bandwidth, respectively. Installing a compact chirped mirror pair ($-250 \text{ fs}^2/\text{bounce}$) into the measurement setup allowed for pulse compression from 126 fs to 40 fs, corresponding to an increase in the peak power by a factor of 3.2 in a single pass of 1 mm CR39 without modifying the operational CPA setup [4]. With the verification of post-CPA pulse compression using CR39, the scalability of this method can now be tested after the 2nd CPA using the full power POLARIS laser pulse, along with a novel technique to obtain a flat-top spatio-spectral profile, even with a spatially inhomogeneous beam.

References

- [1] M. Hornung, H. Liebetrau, S. Keppler, A. Kessler, M. Hellwing, F. Schorcht, G. A. Becker, M. Reuter, J. Polz, J. Körner, J. Hein, and M. C. Kaluza, *Opt. Lett.* 41, 5413–5416 (2016).
- [2] I. Tamer, M. Hellwing, Y. Azamoum, M. Hornung, S. Keppler, F. Schorcht, J. Hein, and M. C. Kaluza, *Opt. Express*, accepted for publication (2020).
- [3] G. Mourou, S. Mironov, E. Khazanov, and A. Sergeev, *Eur. Phys. J. Special Top.* 223, 1181 (2014).
- [4] I. Tamer, M. Hornung, L. Lukas, S. Keppler, M. Hellwing, R. Van Hull, J. Hein, M. Zepf, and M. C. Kaluza, *Opt. Lett.*, submitted for publication (2020).

Carrier-envelope phase stable few-cycle fiber laser system

E. Shestaev², D. Hoff^{1,3}, A. M. Sayle^{1,3}, A. Klenke^{1,2}, S. Hädrich⁵, F. Just⁵, T. Eidam⁵, P. Jójárt⁶, Z. Várallyay⁶, K. Osvay⁶, G. G. Paulus^{1,3}, A. Tünnermann^{1,2,4} and J. Limpert^{1,2,4,5}

¹Helmholtz-Institute Jena, Fröbelstieg 3, 07743 Jena, Germany

²Institute of Applied Physics, Abbe Center of Photonics, Friedrich-Schiller-Universität Jena, Albert-Einstein-Str. 15, 07745 Jena, Germany

³Friedrich-Schiller-Universität Jena, Institut für Optik und Quantenelektronik, Max-Wien-Platz 1, 07743 Jena, Germany

⁴Fraunhofer Institute for Applied Optics and Precision Engineering, Albert-Einstein-Str. 7, 07745 Jena, Germany

⁵Active Fiber Systems GmbH, Ernst-Ruska-Ring 11, 07745 Jena, Germany

⁶ELI-ALPS, ELI-HU Non-Profit Ltd., H-6720 Szeged, Dugonics tér 13, Hungary

Emerging applications in the field of strong-field and attosecond physics rely on the availability of few-cycle carrier-envelope (CE) phase stable laser sources. This means that there is a stable relationship between the temporal envelope of the laser systems and the underlying carrier oscillations and the fundamental wavelengths. State-of-the-art laser systems providing these pulses are currently mostly based on Ti:Sa or OPCPA technology.

Fiber laser systems with subsequent non-linear pulse compression have already proven that they can provide few-cycle pulses with average powers of multiple 100W. By using advanced technologies like synchronous pulse-picking [1], we have demonstrated that CE-phase stability is also achievable with these systems [2]. To the best of our knowledge, this is the first demonstration using a few-cycle fiber laser system. The increased average-power level has the potential to drastically increase the viability for following scientific experiments.

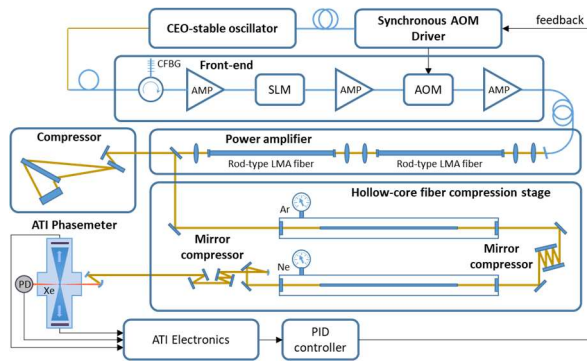


Fig. 1: Schematic experimental setup.

The schematic experimental setup is shown in figure 1. It consists of a actively CE stabilized oscillator, followed by a pulse stretcher, multiple pre-amplifiers, a pulse picker, two rod-type large-area-mode fibers and, finally, a pulse compressor. At this stage, the system provides pulses with 240 fs pulse duration and 300 μ J energy and a repetition rate of 100 kHz. The pulse-picker is based on an acousto-optical modulator (AOM), whereby the acoustic wave is synchronized with the fundamental laser repetition rate. This is necessary to avoid scrambling the CE-phase of the laser pulses. The pulses are further compressed down in a two nonlinear compression stages, both consisting of a hollow-core fiber and a chirped-mirror compressor. A final

pulse duration of 7.6 fs is achieved with this setup. The CE-stability of the pulses was extensively investigated at different points of the system using technologies like f-2f interferometers and a Stereo-ATI phase meter. Great care was taken to characterize CEP noise up to the Nyquist frequency, which is very important in the presence of white noise and high-frequency contributions. The ATI was also employed as a feedback mechanism to the AOM to further reduce slow drifts of the CE-phase.

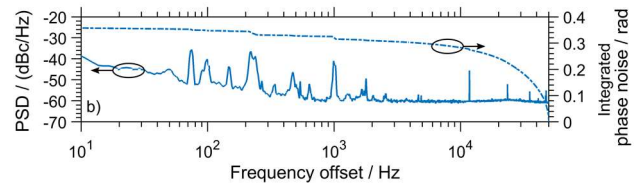


Fig. 2: CEP noise spectrum of the laser system output.

The power spectral density (PSD) plot of the CEP noise of the system without this feedback loop enabled is shown in Fig. 2. The integrated CEP noise amounts to 360 mrad in the frequency range of 10 Hz to 50 kHz. Only 40 mrad are contributed within 10 Hz to 1 kHz and 40 mrad below 10 Hz (not shown). The largest part is accumulated above 10 kHz due to white noise. This high stability is achieved despite the large frequency broadening factor of 45 in the nonlinear compression stage, which is very sensitive towards amplitude fluctuations of the input laser pulses. The very low amplitude noise of the driving laser system of only 0.13% RIN (10 Hz – 50 kHz) makes this possible.

The ongoing research is focused on reducing the high frequency CE-phase fluctuations, as well as investigating additional phase measurement concepts. Work is currently underway to implement these techniques into systems targeting multi-mJ pulse energies and > 1kW average power.

References

- [1] O. de Vries, T. Saule, M. Plötner, F. Lücking, T. Eidam, A. Hoffmann, A. Klenke, S. Hädrich, J. Limpert, S. Holzberger, T. Schreiber, R. Eberhardt, I. Pupeza, and A. Tünnermann, *Opt. Express* **23**(15), 19586–19595 (2015)
- [2] E. Shestaev, D. Hoff, A. M. Sayler, A. Klenke, S. Hädrich, F. Just, T. Eidam, P. Jójárt, Z. Várallyay, K. Osvay, G. G. Paulus, A. Tünnermann, and J. Limpert, *Opt. Lett.* **45**, 97 (2020).

* E. Shestaev acknowledges support by the German Research Foundation (DFG) within the International Research Training Group 2101. We thank P. T. Guerreiro and R. Romero from Sphere Ultrafast Photonics for providing the D-Scan device and assistance with the corresponding measurement. † jens.limpert@uni-jena.de

Generation of coherent broadband high photon flux continua in the XUV with a sub-two-cycle fiber laser

Robert Klas^{1,2, #}, Wilhelm Eschen^{1,2}, Alexander Kirsche^{1,2}, Jan Rothhardt^{1,2,3}
and Jens Limpert^{1,2,3}

¹Helmholtz Institute Jena, Germany; ²Institute of Applied Physics, Jena, Germany; ³Fraunhofer Institute for Applied Optics and Precision Engineering, Jena, Germany

A coherent extreme ultraviolet light source based on high harmonic generation of an average power scalable fiber laser is presented. It generates a broadband continuum from 80 eV to beyond 160 eV with a flux of 10^{11} ph/s. At 92 eV (13.5 nm) $7 \cdot 10^9$ ph/s/eV are generated with an rms deviation of 0.8% over 20 minutes.

Over the past decade, lab-scale extreme ultraviolet (XUV) light sources, based on higher order harmonic generation (HHG) have seen a rapid development [1]. Thus, such sources enabled groundbreaking studies of matter on atomic length (nm) and time (fs) scale [2, 3].

Until now Ti:Sa based driving laser systems have been the workhorse for HHG [4]. However, they are limited in average output power. In contrast, novel Yb-based laser systems allow for femtosecond laser systems with output powers beyond 1 kW. Such lasers have the potential to be a driver for high average power high repetition rate XUV sources with an unprecedented photon flux.

Fiber laser driven sources already have proven their high potential in lens-less imaging experiments with photon energies of ~ 70 eV [3]. However, many applications demand higher photon energies of up to 150 eV. Many important elements, such as Cr, Mn, Fe, Co, Ni and Si have absorption edges in this spectral region. Therefore, experiments in fundamental physics need ultrashort pulse durations as well as a high photon flux to investigate electronic, optical and magnetic properties of complex materials. Furthermore, semiconductor industry is looking for an actinic mask inspection tool for the latest EUV lithography technology at 92 eV (13.5 nm). A coherent high flux source in combination with lens-less imaging is a promising candidate for high resolution, table-top actinic mask inspection [5].

Therefore, a lab-scale XUV source, based on a few cycle laser driven HHG was developed [6]. The driving laser for this XUV source is a fiber laser with subsequent hollow core compression. This result in 400 μ J, 7fs pulses at 30 W average power. These pulses are focused into a gas jet for HHG and result in spectra shown in Fig. 1.

Using neon a broad-bandwidth continuum from 80 eV to 160 eV with a flux 10^{11} ph/s/eV of over this spectral region is generated, which theoretically supports <100 as pulses.

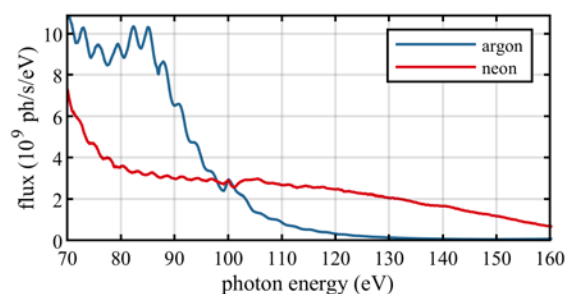


Figure 1: HHG spectra generated with argon (700 μ m jet, 0.6 bar) and neon (150 μ m jet, 13 bar) [5].

Using argon the cutoff energy is lower, however a higher photon flux can be generated, resulting in $7 \cdot 10^9$ ph/s/eV at 92 eV (13.5 nm). Even though this photon energy is in the cutoff region of the spectrum, it still shows a very good long-term stability with an rms deviation of 0.8% over 20 minutes

This source has a great potential for nanoscale imaging experiments at 13.5 nm and due to the broad bandwidth also for XCT experiments [7]. Since fiber lasers have demonstrated average powers up to the kW regime and the components for nonlinear compression and separation of IR and XUV have been proven to handle kW average powers, we are confident that the presented XUV source can be scaled to 10^{11} ph/s/eV in the near future.

References

- [1] S. Hädrich, et al. J. Phys. B 49 (17) (2016).
- [2] F. Krausz et al., Rev. Mod. Phys. 81(1) (2009).
- [3] J. Rothhardt et al., J. Opt. (UK) 20(11) (2018).
- [4] C. Ding et al., Opt. Express 22(5) (2014).
- [5] H. Kinoshita et al., Jpn. J. Appl. Phys. 53 (2014).
- [6] R. Klas et al., Opt. Express, 28(5) (2020).
- [7] S. Fuchs et al., Optica 4 (2017).

[#]robert.klas@uni-jena.de

Infrastructure upgrade at JETi200 Target Area I

Alexander Sävert¹, Georg Schäfer¹, Burgard Beleites², Falk Ronneberger², Ronny Große², Hendrik Wöhl², Matt Zepf^{1,2}

¹Helmholtz Institute Jena, Germany; ²Institute of Optics and Quantum Electronics, Germany

The JETi200 laser system provides high intensity laser pulse for studying laser-plasma-interactions. Over the last years electron bunches were accelerated to energies exceeding the GeV level. At the same time, High Harmonics were generated from solid surfaces with bright beam properties. The energy upgrade of JETi200 in 2018 now enables dual beam experiments with sufficient peak power in each arm. This required a redesign of Target Area I.

Due to the increasing complexity of the experiments carried out over the last years, a number of extensions to the target chamber were made. This has limited the space within the laboratory and restricted the access to the target chamber. Furthermore, the close proximity of the vacuum pumps and the mounting of the target chamber resulted in strong vibration and thus a jitter of the focal spot. When conducting two beam experiments, the spatial and temporal overlap of the two beams is of crucial importance.

A central part was the shift of the target chamber by 1 m in the plane. This required the disassembling of the beam-line leading to the target chamber. After the shift, the inner chamber breadboard was set on preloaded plinths filled with quartz sand. The same was done for the external extension chamber housing the long focal length parabola. This has drastically increased the pointing stability of the laser pulses down to one focal spot diameter. In turn, the beam pointing of the electron bunches generated in laser wake field experiments has decreased to below 1 mrad. Further improvements were achieved by moving the vacuum pumps one level above. Additional increase of the pumping power results in shorter evacuating times despite the further distance. The new position of the pumps made a controls system necessary. Now full control of the vacuum system in the laser laboratory as well as in the target area is possible. Due to the shift of the target chamber now the beam enters from the top giving a wide option to use the input beam in s- or p- polarization. For experiments using the long focal length parabola, p-polarization in the chamber is preferred, which requires s-polarization in the beamline. Changing the polarization was done in an all-reflective way via a periscope in the upstairs laser laboratory. As a further benefit, the dispersion of the used mirrors is up to a factor 5 less in s-polarization than in p-polarization.

At the same time, the reflected bandwidth increases as



Figure 1: View into Target area I with the new setup.

well. The total acquired spectral phase after passing the 20 beam line mirrors is significant reduced and now the pulse compression in the target chamber has improved. The pulse duration is now the same in the laser lab and the target area despite the long distance.

In a next step, different beam splitting techniques are tested. Two options are available. First, using a thin beam splitter. To reduce the induced B-integral for the transmitted beam its thickness is just a couple of millimeter. However, the mechanical properties concerning the reflective and transmitted wave front are quite challenging. The second option is to split the beam into a left and right part using a d-cut mirror. To reduce the occurring diffraction pattern on the subsequent optics, a beam-shaping device will be in use within the laser amplification chain.

After a successful test, a new class of experiments can be performed. This involves high intensity laser-laser interactions as well as generating GeV class electrons and either colliding these directly with a high intensity laser pulse or converting the fast electrons to γ -rays and colliding these with the second beam. This opens the path of a number of experiments that have to take novel physical effects like radiation reaction and pair creation from vacuum into account.

We appreciate the help from the M1, M2, and M3, E1 and E2 workshops and the construction.

a.saevert@gsi.de

Commissioning of Target Area 2 at the JETI Laser

*Peter Hiliz¹, Alexander Sävert¹, Thomas Köhler¹, Georg Schäfer¹, Diethardt Klöppfel¹,
Hendrik Wuerl¹ and Matt Zepf¹*

¹Helmholtz Institute Jena, Germany

JETI 200 is designed to deliver beams into multiple target areas. Initial operation has concentrated on the long focal length target area – TA1. During the past year TA2 has been commissioned as flexible short/intermediate focal length target area. The design of the area includes a distinct design with a target chamber and beam preparation chamber – allowing for complex experiments and beam manipulation prior to the final interaction experiment. The availability of two separate target areas significantly increases the available beam time and range of experiments that can be performed.

The design of the JETI facility included two target areas with different scientific goals. TA1 was designed with long focal lengths and electron beam-lines in mind and therefore well suited for laser wakefield experiments. TA2 smaller foot-print is suited for high intensity, short focal length experiments, such as SHHG, terahertz generation or proton acceleration.

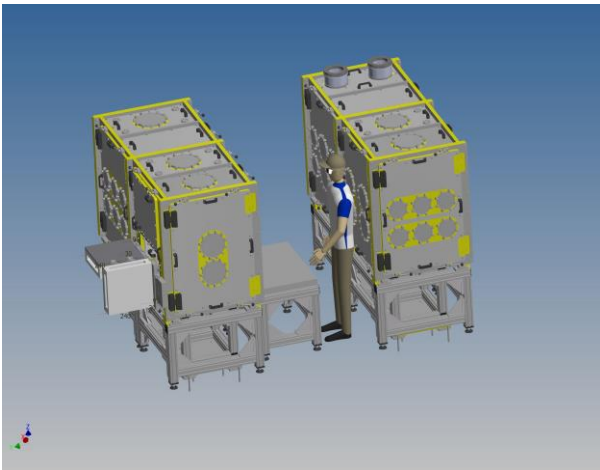


Figure 1: 3D drawing of the experimental chambers. Clearly visible is the split in two distinct chambers allowing for multi-beam and beam preparation.

A key feature of the increasing complexity of high-power laser experiments is the ability to perform beam manipulation after compression. The ability to do this in a single chamber where both plasma/experimental diagnostics and the laser manipulation are present is often limited.

A special feature of TA2 is its dual chamber layout based on the CALA chambers in Munich. The beam first propagates through the common beam line in the laser area (including diagnostics and plasma mirror) and is then directed into the beam manipulation chamber (Fig. 1 on right). This allows the manipulation of the beam at full size (12 cm). Beam parameters such as frequency, pulse duration, polarization etc. or the generation of secondary beams such as probe beams are envisaged through non-linear techniques. In particular pulse broadening/compression of JETI using an intermediate focus and gas targets and the production of phase controlled, multi-harmonic beams are features that will be pursued in the immediate future.

The beam is then handed over to the second chamber which is dedicated to experiments and allows a high degree of experimenter/diagnostic access due to the full-scale door design. The chambers have been designed in such a way that pre-aligned setups on breadboards can be loaded into the chamber as a whole. This will allow to change between different experiments on a short timescale and further increase the efficiency.



Figure 2: Delivery of one vacuum-module

The first experiments in target area II are planned for July 2020. The initial experiment will be a test-bed for for future photon-photon scattering experiments. The first ion acceleration experiments are scheduled right afterwards.

We appreciate the help from the M1, M2, and M3, E1 and E2 workshops and the construction.

p.hiliz@gsi.de

108 W average power GW-level Tm-doped fiber CPA system

T. Heuermann^{1,2,#}, Z. Wang¹, M. Gebhardt¹, M. Lenski¹, C. Gaida³, C. Jauregui¹,
and J. Limpert^{1,2,4}

¹FSU Jena, Germany; ²HI Jena, Germany; ³Active Fiber systems GmbH, Germany; ⁴Fraunhofer IOF Jena, Germany

Scaling average and peak power of laser sources simultaneously is one of the most demanded development in today's laser engineering. In this contribution, we report on the first demonstration of a 100 W average power Tm-doped fiber chirped pulse amplifier system, emitting GW-level peak power at 2 μm wavelength. This shows the great potential of Tm doped fiber lasers toward high average and peak power emission in this highly interesting wavelength region.

In recent years, laser sources with an emission around 2 μm wavelength have attracted significant attention in industry, life- and fundamental sciences. Especially in high-field sciences, these sources are an enabling tool as they allow for the scaling of the cut-off photon energy (up to and beyond the water window, 2 nm – 5 nm [1]) in phase-matched high-harmonic generation (HHG). Since water is transparent in this region of the soft X-ray spectrum, combining tabletop laser driven water window HHG sources, with modern spectroscopic methods would be a game changer for research in life sciences, allowing for accessing time-resolved spectroscopy [2] and even element-specific coherent diffractive imaging [3] of biologic specimens for a broad scientific audience. Since the conversion efficiency of fundamental laser radiation to high order harmonics scales unfavorably with increasing wavelength, this poses high demands on the laser source in terms of peak and average power to reach an application relevant photon flux. An ideal candidate for this could be Tm-doped fiber amplifiers, which have in recent years already proven to be on par with well-established Yb-doped fiber laser technology emitting either peak powers in the excess of 1 GW [4] or average powers of >1 kW [5] in ultrafast operation. The system reported here resembles the first step in combining these properties, which is an important evolution toward the motivation to counterbalance a reduced HHG efficiency at longer driving wavelengths with a higher laser average power. It consists of 4 amplifiers, seeded by a commercial seed laser source. After preamplification the repetition rate is reduced to 417 kHz. The main amplifier consisted of a Tm-doped large pitch fiber [6], with a core diameter of 81 μm and a length of 1.2 m. Utilizing state of the art high efficiency multimode pump combiners, 500 W of cw light at 793 nm was launched to cladding pump the main amplifier from the counter propagating direction. At highest pump power, this led to an average output power

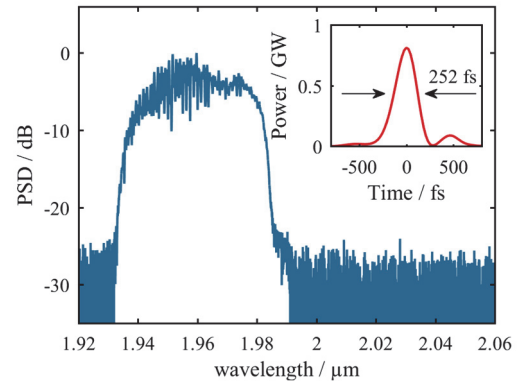


Fig. 1: Spectrum and reconstructed pulse profile (inlet) of the laser system at highest average output power.

of 132 W from the main amplifier. The pulses were afterwards compressed by a Treacy-type compressor with an efficiency of >80%. In order to prevent propagation effects associated with the absorption of water vapor [7], all high-power parts of the system were placed in dry air atmosphere. This led to an overall system performance of 108 W at 417 kHz with an output pulse energy of 260 μJ . The spectrum and the reconstructed pulse profile are shown in Fig. 1. Even though the modulations apparent in the spectrum are a signature of the onset of nonlinear propagation effects in the main amplifier, the output pulses have an acceptable contrast and are only 250 fs long. With a peak power of 0.8 GW, this is the highest average power, GW-class 2 μm fiber laser system ever demonstrated. Regarding future work on the laser side, we see promising performance enhancement prospects and further development in this direction will thereby pave the way towards high flux tabletop emission of harmonic radiation in the water window.

References

- [1] D. Popmintchev et al., Phys. Rev Lett. 120, 9 (2018).
- [2] N. Saito et al., Optica 6, 12 (2019).
- [3] M. Rose et al., Opt. Express 26, 2 (2018).
- [4] C. Gaida et al., Opt. Lett. 41, 17 (2016).
- [5] C. Gaida et al., Opt. Lett. 43, 23 (2018).
- [6] J. Limpert et al., Light Sci. Appl. 1, e8 (2012).
- [7] M. Gebhardt et al., Opt. Express 23, 11 (2015).

tobias.heuermann@uni-jena.de

Ultrafast lasers based on multi-pass post-compression

P. Balla^{1,2}, Ammar Bin Wahid², Arthur Schönberg^{1,2}, Ingmar Hartl², Christoph M. Heyl^{1,2,#}
and collaborators from DESY/University of Hamburg/Lund University/Ecole Polytechnique

¹Helmholtz Institute Jena, Germany; ²DESY, Hamburg, Germany

This progress report discusses recent efforts carried out at DESY aiming at exploring new laser concepts for Free-Electron Laser (FEL) sciences, spectroscopy and particle acceleration. Our efforts are based on multi-pass spectral broadening of Yb:YAG lasers followed by post-compression. We demonstrate the compression of picosecond laser pulses reaching a record compression factor in a single post-compression stage. Moreover, a second compression stage enables the generation of few-cycle laser pulses directly by post-compression of picosecond pulses.

The demand for higher average power ultrafast lasers as drivers for a wide range of applications, ranging from AMO physics to laser-based particle acceleration, has brought along alternative solutions to Ti:Sapphire amplifiers including Ytterbium (Yb)-based systems. While Ti:Sapphire-based systems, representing a working horse ultrafast laser platform since many years, easily reach pulse durations around 30 fs, their average power is typically limited to the few-Watt regime. Contrarily, Yb amplifiers are easily power-scalable into the kW regime [1]; however, their output pulse duration is limited to a few 100 fs up to 1 ps. This limitation can be circumvented by external spectral broadening e.g. in hollow-core fibers followed by post-compression, combining ultrashort pulse durations and high repetition rates with mJ-level pulse energies [2]. An alternative spectral broadening technique relies on Herriott-type multi-pass cells (MPCs), offering high throughput, large compression ratios and excellent beam quality while allowing for compact setups [3, 4]. In this scheme, a laser pulse is sent multiple times through a MPC, undergoing self-phase modulation causing spectral broadening. A simple compressor can then be employed to post-compress the spectrally broadened pulses.

We here demonstrate MPC-based post-compression reaching the few-cycle regime directly driven with 1.2 ps pulses generated by an Innoslab Yb:YAG laser system. Using a single MPC, we broaden and compress 2 mJ pulses at 200 W in-burst average power down to 32 fs. A second post-compression stage yields 13 fs at reduced pulse energy (Figure 1). These results demonstrate few-cycle pulse generation via direct post-compression of picosecond pulses for the first time, opening a route towards high-average power few-cycle sources. Moreover,

we push the single-stage compression factor achieved via mJ-level post-compression to ~ 40 with $>80\%$ throughput [5], surpassing latest record compression factors achieved using stretched hollow-core fibers [2, 6] and MPCs [7].

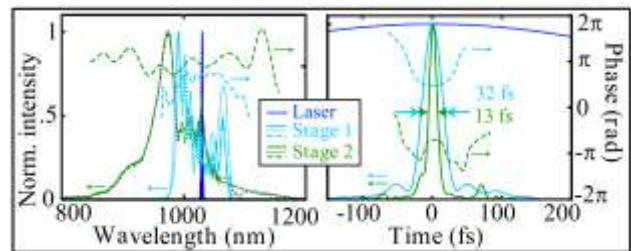


Figure 1: Reconstructed spectral and temporal intensity (solid) and phase (dashed) profiles together with the corresponding spectra measured after compression stage 1 and 2 (dotted) and at the laser output (blue area).

Our results already triggered further development efforts at DESY including novel laser platforms for FEL pump-probe experiments as well as laser plasma accelerator R&D. As the employed laser and compression scheme is known for excellent pulse energy and average power scalability, the demonstrated method promises further pulse energy upscaling potential and may thus enable future terawatt (TW)-class, few-cycle laser sources driven by industrial-grade kW-scale picosecond lasers.

This work was supported by PIER Seed Projects grant (partnership of Universität Hamburg and DESY) (PIF-2018-85); Cluster of Excellence “CUI: Advanced Imaging of Matter” of the Deutsche Forschungsgemeinschaft (EXC 2056 (390715994)); Swedish Research Council; European Research Council (339253 PALP).

References

- [1] M. Müller *et al.*, Opt. Lett. **43**, 6037 (2018).
- [2] T. Nagy *et al.*, Optica **6**, 1423 (2019).
- [3] J. Schulte *et al.*, Opt. Lett. **41**, 4511 (2016).
- [4] M. Hanna *et al.*, JOSA B **34**, 1340 (2017).
- [5] P. Balla *et al.*, Opt. Lett. **45**, 2572 (2020).
- [6] Y.-G. Jeong, *et al.*, Sci. Rep. **8**, 11794 (2018).
- [7] M. Kaumanns *et al.*, Opt. Lett. **43**, 5877 (2018).

[#] c.hey@gsi.de

Laser Particle Acceleration

NOPA-based Ultrashort Optical Probe Pulse for Laser-Plasma Interactions

I. Tamer^{1,2}, M. Hellwing², Y. Azamoum¹, M. Hornung^{1,2}, S. Keppler^{1,2},
F. Schorcht¹, J. Hein^{1,2}, M.C. Kaluza^{1,2}

¹Helmholtz-Institute Jena, Germany; ²Institute of Optics and Quantum Electronics, Jena, Germany.

The laser pulses delivered by the POLARIS [1] system at the Helmholtz-Institute Jena are focused to achieve intensities on the order of 10^{20} W/cm², and are utilized in laser-plasma experiments to generate relativistic electrons and energetic ion beams. An improvement in the accelerated particle energies requires not only an enhancement of the laser system parameters (e.g., the peak power [2]), but also advanced optical diagnostics that can reveal the intricate details of the underlying acceleration mechanisms with a high spatial and temporal resolution. For this purpose, the POLARIS laser system has been equipped with a unique ultrashort optical probing system [3], capable of fulfilling the stringent design criteria established by the current and upcoming experimental campaigns.

The ultrashort optical probe pulse originates at the POLARIS oscillator, after which a single pulse is selected and coupled into a dedicated CPA system comprising a grating stretcher, a regenerative amplifier with Yb:FP15-glass as the active material, and a grating compressor. The output 2 mJ, 120 fs laser pulse is then utilized, as seen in Fig. 1, to produce both the signal and pump pulses for a noncollinear optical parametric amplifier (NOPA). Enabling a high temporal resolution for the NOPA-based optical probe requires an ultrabroadband signal pulse to allow for a compressed pulse duration in the few-cycle regime. Here, a nJ-level white light supercontinuum (WLC) was generated by focusing the attenuated (720 nJ) laser pulse into a 5 mm YAG crystal. To satisfy the phase-matching conditions for the NOPA process, the nearly 2 mJ, 120 fs pulse from the CPA system was converted into the second harmonic (SH), with a central wavelength of 515 nm, in a 3 mm KDP crystal. The WLC and SH pulses were then temporally aligned within a 2 mm BBO crystal for NOPA. The influence of the group velocity dispersion from the YAG and BBO crystals on the WLC pulse were compensated with a chirped mirror pair placed before the NOPA stage, leading to a matching of the WLC and SH pulse durations at the start of the BBO crystal and a near-FTL NOPA output.

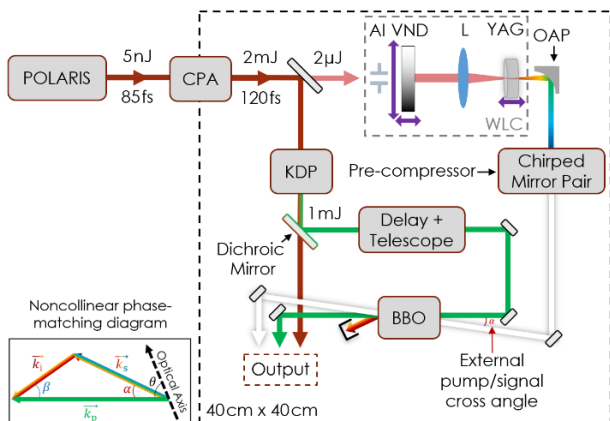


Figure 1: Schematic of the NOPA-based probing system.

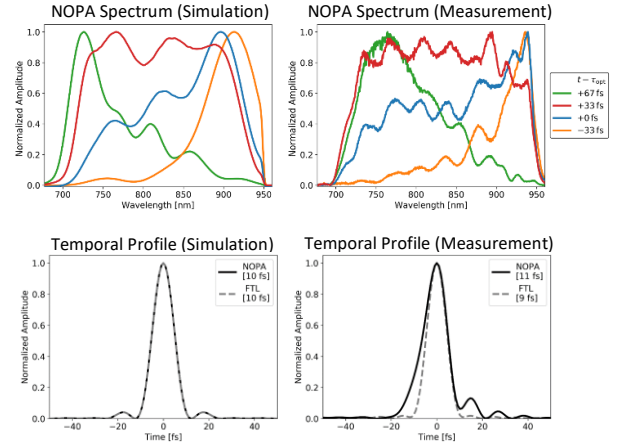


Figure 2: Simulated (left) and experimental (right) NOPA optimization results. By properly adjusting the signal pre-chirp, pump/signal cross angle, and pump/signal delay, a flat-top-like output spectrum (top) and near-FTL output pulse duration (bottom, $\tau = \tau_{\text{opt}} + 33$ fs) can be achieved.

The inhomogeneous, ultrabroadband WLC spectrum could be simultaneously shaped, as depicted in Fig. 2, and amplified through a precise optimization of the signal pre-chirp ($\text{GDD} = -150$ fs²), pump/signal cross angle ($\alpha = 2.65^\circ$), and pump/signal delay ($\tau_{\text{opt}} + 33$ fs). The fs-pumped, direct NOPA setup produces a record 20 μ J, 11 fs pulses at the output of a single BBO crystal with 230 nm FWHM bandwidth at 820 nm central wavelength. The flat-top-like spectrum and minimal shot-to-shot spectral fluctuation of 0.46% RMS are ideal for enabling a stable and homogeneous illumination throughout the temporal window of the probed laser-plasma interaction. The multi-beam output of the ultrashort optical probe has been temporally synchronized with the POLARIS main laser pulse using a dedicated diagnostic stage that spans multiple orders of magnitude of delay, and the NOPA output of the probing system is currently being employed in a chirped pulse probing configuration to explore the complex dynamics of laser-plasma interactions at the petawatt-class POLARIS laser system.

References

- [1] M. Hornung, H. Liebetrau, S. Keppler, A. Kessler, M. Hellwing, F. Schorcht, G. A. Becker, M. Reuter, J. Polz, J. Körner, J. Hein, and M. C. Kaluza, *Opt. Lett.* 41, 5413–5416 (2016).
- [2] I. Tamer, M. Hornung, L. Lukas, S. Keppler, M. Hellwing, R. Van Hull, J. Hein, M. Zepf, and M. C. Kaluza, *Opt. Lett.*, submitted for publication (2020).
- [3] I. Tamer, M. Hellwing, Y. Azamoum, M. Hornung, S. Keppler, F. Schorcht, J. Hein, and M. C. Kaluza, *Opt. Express*, accepted for publication (2020).

Terahertz generation using two colour plasma filament

T.Kawde¹, S.Popruzhenko², G. G. Paulus^{1,3}, and A.Gopal^{1,3}

¹Helmholtz Institute Jena, Germany; ²Prokhorov General Physics Institute, Moscow,Russia; ³Institut für Optik und Quantenelektronik, Friedrich-Schiller-Universität Jena

Terahertz radiation generation in air by mixing two-color femtosecond laser pulses is investigated. Optical to terahertz conversion efficiency is optimized by enhancing the photocurrent in the plasma by varying incident laser polarizations.

Frequency mixing in materials can synthesize new frequencies by nonlinear interaction of light with matter. Observation of terahertz generation from intense laser produced air plasma was initially thought to be due to four wave mixing process[1]. However, the four-wave mixing model could not explain all of the observed phenomena, in particular, the intensity threshold coincident with the threshold for ionization of the gas. Thus the photocurrent model was proposed using the strong field approximation and classical electrodynamics[2]. A photocurrent is formed due to the average drift velocity of the electrons, which is determined by the laser vector potential at the moment when they are ionized. This photocurrent could be enhanced by employing dual or multi color color schemes or by few cycle pulses[2, 3]. Recent works proposed new schemes to increase the THz pulse energy by employing circularly polarised mid infrared pulses [4, 5]. The exper-

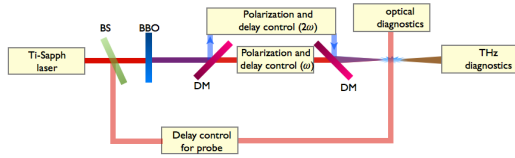


Figure 1: *Experimental scheme for investigating THz generation from dual color plasma filaments. BS: beam splitter, DM: dichroic mirror*

imental scheme presented in Figure 1 comprises of a two color generation set up driven by a Ti-Sapph laser operating at 1 kHz emitting short pulses at 800 nm wavelength and 30 fs duration. The polarization and temporal delay between the laser pulses are controlled by a Mach-Zehnder interferometer. The generated THz radiation from air plasma channel is recorded with a pyrometer equipped with a silicon window. The plasma channel is characterized with orthogonal probing by sending a temporally delayed leakage beam of the main laser pulse across the plasma channel. Furthermore, the transmitted laser pulses were collected and send to a high resolution spectrometer. We measured the THz pulse generated with an fundamental energy $E_{\omega} = 1.3$ mJ and second harmonic $E_{2\omega} = 180$ μ J. The temporal delay between the pulses was measured relative to the position of maximum 3rd harmonic signal correspond-

ing to maximum overlap between ω and 2ω . We observed

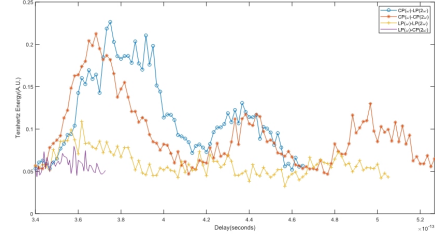


Figure 2: *Terahertz yield for different laser polarisations for different temporal delay between ω and 2ω pulses*

the maximum THz emission for circular polarization of ω irrespective of 2ω polarization state. The emission lasted for 80 fs as seen in Figure 2. While the transmitted spectrum of the pump pulses observed a blue shift for the fundamental in case of CP(ω)-LP(2ω) and an enhancement of the second harmonic in the transmission spectrum with increase in THz generation as shown in Figure 3. This change could be attributed to sum frequency mixing between the ω and the generated THz waves. Beyond the time window be-

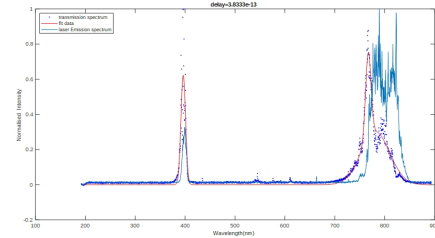


Figure 3: *Transmission spectrum of CP(ω)-CP(2ω) with enhancement of second harmonic*

tween ω and 2ω for THz generation, no significant shift is observed in the transmitted laser spectrum compared to input spectrum. This implies our interaction intensities is below the whitelight generation regime.

References

- [1] D. J. Cook and R. M. Hochstrasser 2000 Opt. Lett. 25, 1210
- [2] K. Y. Kim et al., 2008 Nat. Photon. 2, 605 and references therein.
- [3] M. Kress, et al., 2008, Nat. Phys 2, 327
- [4] Chao Meng et al. 2016 Appl. Phys. Lett. 109, 131105
- [5] V. A. Tulsy et al. 2011 Phys. Rev. A 98, 053415

A flexible X-ray source with tunable polarization and orbital angular momentum from Hermite-Gaussian laser modes driven plasma channel wakefields

Bifeng Lei^{*1,2}, Tom Teter^{1,2}, Jingwei Wang³, Matt Zepf^{4,2}, and Sergey G. Rykovanov^{†4}

¹Helmholtz Institute Jena, Germany; ²IOQ, Germany; ³SIOM, China; ⁴Skoltech, Russia

We are reporting a new scheme of plasma undulator/wiggler produced by the beating of several different Hermite-Gaussian (HG) laser pulses inside a parabolic plasma channel [1, 2]. The oscillation of the excited plasma wakefield is caused by the interference between each set of two pulses. Control over both the betatron and undulator forces is conveniently achieved by tuning the amplitude ratios, colors, and order numbers of the modes. A special structure of the undulator/wiggler field without the focusing force near the propagation axis enables the generation high-quality radiation beam with tunable polarization and OAM.

A parabolic plasma channel supports the propagation of a linearly polarized laser pulse in a HG mode of order m and n , $\tilde{a}_\perp(\tau, x, y) = \frac{a_0}{2}\eta\chi(x, y)e^{-i\theta\tau+i\varphi}$, where a_0 is the normalized amplitude of the mode and φ is its phase. $\eta = 1/\sqrt{2^{m+n}m!n!}$ is a normalization coefficient, where m and n are the numbers of modes in \hat{x} and \hat{y} directions respectively. $\chi(x, y) = H_m(x/\sqrt{R})H_n(y/\sqrt{R})\exp\{-(x^2 + y^2)/2R\}$, $\theta = (1/2M_p + (m+n+1)/M_pR)$, where $H_n(x)$ is a Hermite polynomial of n -th order, and R is the normalized plasma channel depth and $M_p = \lambda_l/\lambda_p$ with λ_l and λ_p as the wave length of laser pulse and plasma wave respectively.

In the case of the superposition of various HG modes, due to the difference in the phase velocity, the intensity profile $I = a_\perp(\tau, x, y, \zeta)a_\perp(\tau, x, y, \zeta)^*$ will contain interference terms and can lead to the oscillatory structure which is dependent on the mode numbers. The wakefield driven by such super pulse can oscillate around the axis of the channel due to the interference between different HG modes. For example, as shown in Fig.1, the wakefield is excited by beating fundamental and first-order modes together. It is easily shown that, if these modes strength a_0 and a_1 can be matched as

$$a_0^2 - 2a_1^2 = 0, \quad (1)$$

the inner structure of the wakefield field is dramatically changed, as seen in Fig.1(b), and independent of the spatial coordinates near the propagation axis \hat{z} . Such a special wakefield will reduce the spread of momentum and energy of the electron beam, and subsequently be very beneficial for the generation of a narrow radiation spectrum.

* B.Lei@gsi.de

† S.Rykovanov@skoltech.ru

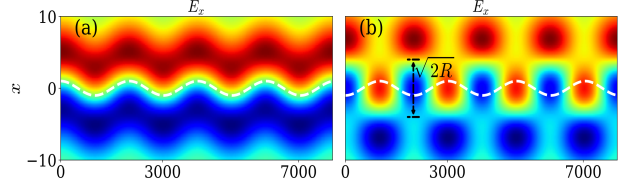


Figure 1: (a), (b) Projection of the transverse wakefield E_x , generated by two different modes without and with the condition (1), as a function of time τ on $\hat{x}\hat{z}$ plane. The dashed white lines show the trajectories of an electron in the wakefield.

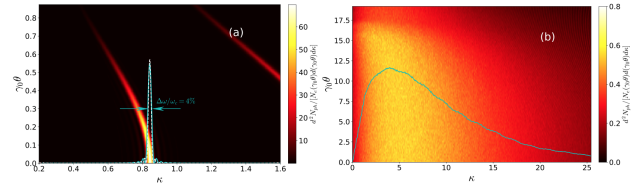


Figure 2: Radiation spectrum from plasma-based undulator/wiggler with (a) $a_u \simeq 0.62$ and (b) $a_u \simeq 16$. Dashed white line is the theoretical on-axis solution and solid cyan lines in both plots are for the numerical on-axis radiation with $\gamma_0\theta = 0$.

For a relativistic electron injected on-axis into the special wakefield as shown in Fig.1(b), the motion is described by a linear harmonically driven oscillator equation and then the radiation is calculated. As shown in Fig.2, the spectrum depends on the undulator strength of the electron beam $0 < a_u < \gamma_0\Omega\sqrt{2R}$. As a result, it is capable of generating a narrow X-ray radiation spectrum for $a_u < 1$ as well as synchrotron-like X/γ -ray radiation with higher-order emitted harmonics containing OAM for $a_u > 1$.

References

- [1] B. Lei, et al. Phys. Rev. Accel. Beams **22**, 071302 (2019)
- [2] B. Lei, Ph.D thesis, FSU, Jena (2019)

This work was supported by the Helmholtz Association (Young Investigator's Group VH-NG-1037). The authors are grateful to D. Seipt, I. Andriyash, S. Kuschel, and M. Zolotarev for fruitful discussions. The Authors acknowledge the usage of the Skoltech CDISE HPC cluster Zhores.

Few-Cycle Microscopy of Stimulated Raman Side Scattering (SRSS) in a Laser Wakefield Accelerator

C. Zepter^{*1}, A. Sävert^{1,2}, A. Seidel¹, M. Zepf^{1,2}, and M.C. Kaluza^{1,2}

¹Institute of Optics and Quantum Electronics, Jena, Germany; ²Helmholtz Institute Jena, Germany

We report on (stimulated) Raman Side Scattering results obtained during a laser wakefield acceleration experiment carried out with the JeTi-200 laser system at the Helmholtz-Institute Jena using Few-Cycle Microscopy on a micrometre scale.

One of the possible instabilities arising during laser wakefield acceleration of electrons is Stimulated Raman Side Scattering (SRSS) in which the intense driving laser pulse with frequency ω_0 and wave vector \vec{k}_0 decays into an electron plasma wave (ω_p, \vec{k}_p) and a scattered light wave (ω_s, \vec{k}_s) with the amplitude of the instability eventually growing in time. The angle φ under which the fundamental wave is scattered in SRSS (\vec{k}_s , cf. Fig.1) can be calculated via [1]

$$\sin(\varphi) = \cos(\theta) = \sqrt{\frac{2 \cdot \omega_p}{\omega_0 \cdot \gamma}} \quad \text{with } \gamma = \sqrt{1 + \frac{a_0^2}{2}}$$

($a_0 \dots$ normalized vector potential of fundamental wave)

In an experiment at the JeTi-200 laser, the scattering process was imaged using an ultrashort probe pulse ($\tau < 8$ fs) and a high resolution imaging set up with a 12.5x magnification and a resolution of $0.5 \mu\text{m}/\text{pixel}$ in a transverse pump-probe geometry [2].

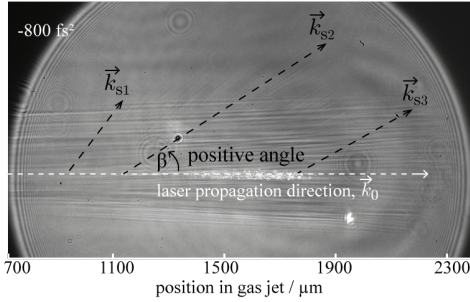


Figure 1: Raw Image of the SRSS process.

Fig.1 is a Few-Cycle Microscopy image taken from a negatively chirped pump pulse at an electron densities of $n_e = 1.04 \cdot 10^{19} \text{ cm}^{-3}$ in the middle of a 3 mm gas jet. One can clearly observe the k-vectors becoming flatter in propagation direction of the pump and the angle β becoming smaller, respectively. Furthermore, the direction of the scattered light (up or down) changes with the sign of the applied GDD (not shown here). In each image the maximum and minimum angle of the scattered light from the laser propagation axis was measured (grey bars in Fig. 2). In Fig.2 the absolute value of the measured angles β are plotted over the GDD applied to the main laser pulse. Fitting the theoretical scattering angle φ into the graph

shows that φ due to SRSS alone does not fit the measured data. The scattering angle β is significantly larger.

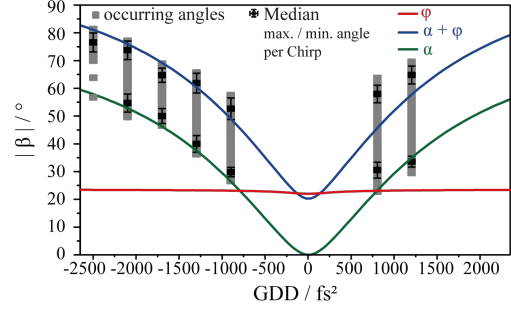


Figure 2: Measured scattering angles over applied GDD.

In Fig.3(a) the lateral intensity distribution of the laser focus at the beginning of the gas jet is illustrated. The dashed circles indicate the position of the focal spot taken with a short (blue)- and longpass (red)-filter on the camera.

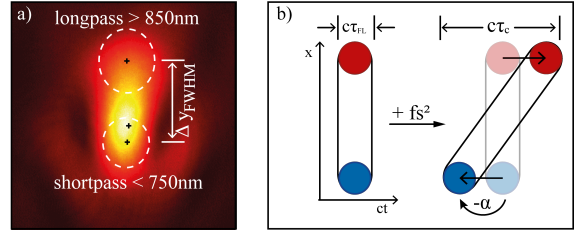


Figure 3: (a) Vacuum focus of the pump pulse. (b) Pulse front tilt due to temporal chirp realized by changing the GDD.

This lateral displacement of the different colours in the focal plane is a direct consequence of an angular chirp due to a misalignment in the compressor. When applying GDD, the pulse thus is not only temporally broadened but also its front is tilted by an angle α due to the lateral displacement (cf. Fig. 3(b)). This angle can be calculated via

$$\alpha = \frac{c \cdot \tau_c}{\Delta y_{\text{FWHM}}} \quad \text{with } \tau_c \approx \tau_{\text{FL}} \cdot \sqrt{1 + (4 \ln 2)^2 \left(\frac{\text{GDD}}{\tau_{\text{FL}}^2} \right)^2}$$

The curve in Fig. 2 combining both angles ($\alpha + \varphi$, blue) is in good agreement with the medians of the measured maximum scattering angles at the beginning of the gas jet. This shows that SRSS alone cannot explain the data and that the tilted pulse front of the pump pulse needs to be taken into account as well. Numerical simulations corroborating this interpretation are currently under way.

References

- [1] T. Matsuoka et al., Phys. Rev. Lett. **105**, 034801 (2010)
- [2] M. B. Schwab et al., Appl. Phys. Lett. **103**, 191118 (2013).

* carola.zepter@uni-jena.de

Detecting multi 100 MeV Electron Positron Pairs from Quantum Vacuum on Photon-Photon collision experiments at Astra Gemini

D. Hollatz^{*1,2,3}, *G. M. Samarin*⁴, *E. Gerstmayr*⁵, *B. Kettle*⁵, *F. Salgado*^{1,2,3}, *S. P. Mangles*⁵, and *M. Zepf*^{1,2,3}

¹HI Jena; ²GSI, Darmstadt; ³IOQ, FSU Jena; ⁴Queen's Univ. Belfast; ⁵Imperial College London

We present the development and experimental testing of a detection system for electron positron pairs on high intensity laser experiments at Astra Gemini, produced by pure photon-photon collision from quantum vacuum. The system is composed of permanent magnets, lead shielding and sensitive Caesium Iodide crystal detectors. The performance has been measured and the required sample size for a statistical significance of 4σ is calculated to be 153 shots at nominal laser accelerator performance of 300pC/shot.

One of the two Gemini laser beams was used to accelerate 11.5 pC of electrons via LWFA up to 550 MeV of energy. This beam propagates through a 1 mm thick Bismuth converter target and emits Bremsstrahlung, which is further collimated by a 10 cm long hollow cylinder of solid Tantalum with a 2 mm wide bore. A 1 T strong, 40 cm long permanent magnet deviates remaining charged particles away from the interaction region. Finally, the pure multi 100 MeV γ -beam collides with a strong x-ray field, produced by a burn through Germanium foil driven by Gemini's second beam. The high density x-ray flux results in an appreciable pair production probability for γ -rays above the energetic reaction threshold determined by the particles rest mass. While single energetic leptons are typically detectable, the challenge in this experiment is separating the signal from the intense background in a space constrained experiment. To achieve this the analyzer magnetic system separates the pairs from the intense γ -beam and directs them onto small but highly sensitive detectors, encapsulated in lead based radiation shielding. (Fig. 1)

calculations with the measured primary LWFA beam, we infer that (225 ± 61) positrons carrying a total energy of (62 ± 17) GeV hit the detector during PTFE shots. This gives a calibration of $(1.4 \pm 0.8) \cdot 10^7$ counts per GeV for incident multi 100 MeV positrons.

On the experiment, with no positron target and full radiation shielding, we measured a detector signal of $(3.3 \pm 0.8) \cdot 10^7$ counts with an average LWFA beam charge of (9.3 ± 2.5) pC, giving a background level of $(3.5 \pm 0.9) \cdot 10^9$ counts/nC. This is due to scattered secondary radiation from the primary electron and γ -ray beams. By measuring this, we were able to compensate for charge variations on a single shot basis, giving an improved background level stability of $(3.5 \pm 0.3) \cdot 10^9$ counts/nC.

The expected pair-rate depends on the density of the thermal x-ray photons in the γ -ray beam path and the intensity of the γ -ray beam itself. Calculations for our experimental geometry and x-ray source [2] predict a rate of 4.3 pairs/nC. Assuming all positrons hit the detector, the average Breit-Wheeler signal would be $1.7 \cdot 10^7$ counts/nC above the background level of $(3.5 \pm 0.3) \cdot 10^9$ counts/nC.

To bring the statistical significance up to our targeted value of 4σ , the measured Breit-Wheeler signal μ_{BW} needs to have a standard error $\delta\mu_{BW}$ smaller than $\frac{1}{4}$ th of the signal level above background μ_{BG} . If we assume a normal distribution for the signal variation, the standard error of the mean $\delta\mu_{BW}$ can be expressed by the standard deviation σ_{BW} and the number of shots n_{BW} as $\delta\mu_{BW} = \frac{\sigma_{BW}}{\sqrt{n_{BW}}}$, which gives the following expression for the number of signal shots needed:

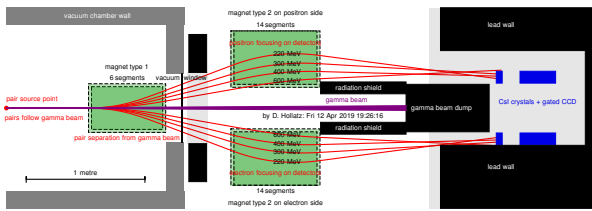


Figure 1: A top view sketch of the analyser magnet system (green) with γ -beam (purple) and pair trajectories (red) around the shielding (black) onto the detectors (blue). [1]

To calibrate the detectors, we inserted a 1 mm thick PTFE target into the beam to provide a defined positron source, which yielded a total $(8.7 \pm 2.7) \cdot 10^8$ counts. From a combination of Geant4 simulations and Radia tracking

$$n_{BW} > \left(\frac{4\sigma_{BW}}{|\mu_{BW} - \mu_{BG}|} \right)^2 \quad (1)$$

Assuming a constant conversion probability with $\sigma_{BW} \approx \sigma_{BG} = 0.3 \cdot 10^9$ counts/nC and a pair rate of $|\mu_{BW} - \mu_{BG}| = 1.7 \cdot 10^7$ counts/nC, 46 nC total electron beam charge is required. During the experiment the energy of the Gemini laser was limited resulting in reduced charge of (9.3 ± 2.5) pC per shot requiring ≈ 5000 shots for 4σ significance. For an electron source delivering the previously demonstrated performance of 300pC per shot [3], 153 shots are predicted to be sufficient.

References

- [1] D. Hollatz, Dissertation, HI Jena & FSU Jena (ongoing)
- [2] G. M. Samarin, Dissertation, Queen's Univ. Belfast, 2019
- [3] K. Poder, Dissertation, Imperial College London, 2016

* D.Hollatz@gsi.de

Single Shot 1D Space-Time Resolved Transmission Diagnostic for Probing Relativistic Laser-Plasma Interaction

Y. Azamoum^{*1,2}, G. A. Becker¹, S. Keppler^{1,2}, I. Tamer^{1,2}, M. Hornung^{1,2}, M. Hellwing¹, F. Schorcht², and M. C. Kaluza^{1,2}

¹Institute of Optics and Quantum Electronics, Jena, Germany; ²Helmholtz Institute Jena, Germany

Recent progress in ultraintense short-pulse laser systems have facilitated the acceleration of highly energetic ions from ultrathin foils. However, fluctuations of the different laser parameters, mainly laser energy, focal spot size and temporal intensity contrast, have a strong influence on the target properties and ultimately on the acceleration process itself. Furthermore, the possible interplay of different acceleration mechanisms is not yet fully understood. Therefore, single-shot diagnostics are necessary to achieve a better control in laser-plasma experiments as well as a deeper understanding of the acceleration scheme. Ion acceleration depends on the absorption of the incident laser pulse in a pre-formed plasma, where the so-called hot electrons are accelerated by the laser field [1]. The temporal intensity contrast affects significantly the generation of the pre-plasma and thus the laser absorption process which relies on the pre-plasma's electron density and scale length. Also, recent studies indicate that an overdense plasma may become transparent during the laser-plasma interaction due to the increase of the electrons' relativistic mass [2]. Ions might be accelerated to higher energies in this regime. In this context, we developed a new transmission diagnostic to be able to monitor the spatio-temporal dynamics of the plasma properties within a single laser shot. The experiment was set up at the POLARIS laser system operated at the Helmholtz Institute Jena. The probe laser is a homemade non-collinear optical parametric amplifier (NOPA) [3] seeded by the same oscillator as the POLARIS system. The 200 nm broadband probe pulses, centered around 800 nm, contain 10 μ J laser energy and can be as short as 11 fs. The experimental setup is depicted in Figure 1a).

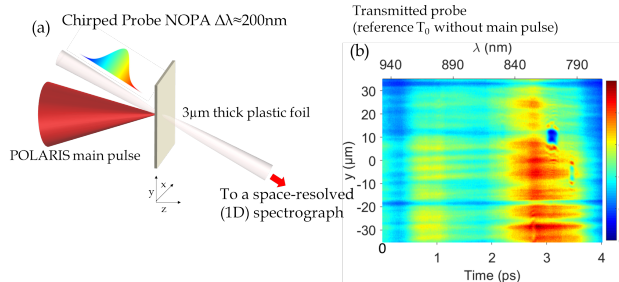


Figure 1: (a) Sketch of the experimental setup. (b) Transmitted probe beam through a transparent target without main pulse imaged onto a 1D space-resolved spectrograph.

Before reaching the interaction zone, the probe pulses were positively chirped and thus stretched to a duration of 6 ps. The probe pulses propagate then through the target at an angle of incidence of 37° . The interaction region is imaged onto a 1D space-resolved spectrograph with a spa-

tial resolution of $\sim 2 \mu$ m. Due to the introduced chirp, the different wavelengths correspond to different times of the laser-plasma interaction. By the wavelength separation within the spectrometer, the plasma generation can be monitored as a function of time and one spatial dimension. The temporal calibration of the wavelength axis was obtained using a controlled pre-pulse with different delays to the main pulse. Figure 2a) shows a preliminary measurement of 1D space-time resolved relative transmission (T/T_0) of the probe pulse through a 3 μ m thick plastic foil. T and T_0 are the probe pulse's transmission with and without the main pulse. In this measurement, the main pulse with an energy of $E = 0.62$ J, was focused at normal incidence on the target, with an effective f-number of 2.5, resulting in an intensity of $I = 7 \times 10^{18}$ W/cm².

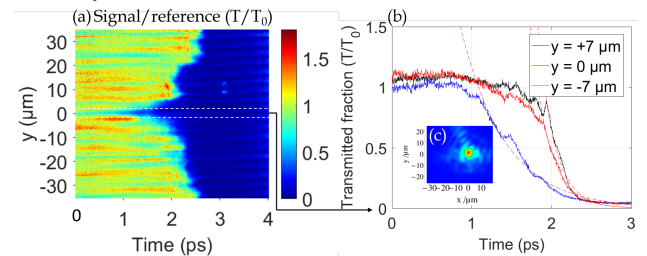


Figure 2: (a) 1D space-time map of the probe pulse relative transmission (T/T_0) during the interaction. (b) Relative transmission as a function of time for different spatial positions (y) in the focal plane. (c) Spatial profile of the main pulse's focal spot.

Figure 2a) reveals a region where the target is fully transparent ($T/T_0 \sim 1$, $n_e \ll n_c$, with n_e , n_c being the electron density and the critical density respectively) and a region where the target is fully opaque ($T/T_0 \sim 0$, $n_e \gg n_c$) depending on the time during the interaction. As the opacity is induced by the electron density increasing during the ionization process, Figure 2b) indicates that within the focal spot at $y = 0 \mu$ m the ionization starts earlier ($t \sim 1$ ps) and lasts longer ($\tau_i \sim 0.6$ ps) compared to the regions of low laser intensity outside the focus (at $y = \pm 7 \mu$ m, $t \sim 2$ ps and $\tau_i \sim 0.2$ ps). This single-shot measurement points out the strong dependence of the plasma generation on both the temporal intensity contrast and the spatial focus quality. In the near future, we will investigate the plasma dynamics for different contrast conditions and target materials. This new diagnostic also paves the way to investigate novel regimes such as relativistic self-induced transparency [2].

References

- [1] A. Macchi *et al.*, Rev. Mod. Phys. **85**, 751 (2013).
- [2] S. Palaniyappan *et al.*, Nat. Phys. **8**, 763 (2012).
- [3] I. Tamer *et al.*, Opt. Express, doi:10.1364/OE.388344 (2020).

* yasmina.azamoum@uni-jena.de

Establishment of a dedicated plasma characterization laboratory

S. Keppler^{*1,2}, *M. Hellwing*², *F. Schorcht*¹, *M. Mäusezahl*², *T. Weickhardt*², *M. Beyer*², *M. Nolte*², *J. Margraf*², and *M. C. Kaluza*^{1,2}

¹Helmholtz Institute Jena, Germany; ²Institute of Optics and Quantum Electronics, FSU Jena, Germany

Recent endeavours in the field of laser-driven ion acceleration from solid targets highlight the importance of the driving laser's temporal intensity contrast. The contrast fundamentally determines the density and geometric shape of the pre-plasma in which the main laser is absorbed and converted into 'hot' electrons. In the so-called 'Target Normal Sheath Acceleration'-regime (TNSA), these electrons travel through the target and generate a sheath field on the rear side in which protons from contamination layers can be efficiently accelerated. In order to achieve a high conversion efficiency of the laser energy into kinetic energy of the accelerated protons, the absorption of the laser pulse, and thus the pre-plasma itself, must be precisely tailored. This requires a complete understanding of the generation and spatial expansion of the pre-plasma. In this context, the plasma excitation with spatio-temporally shaped pre-pulses or the use of specially developed target surfaces are a key technology for optimizing laser-driven proton acceleration.

To make these technologies available for the experiments at Polaris, we have developed an independent pump-probe setup, which allows to precisely characterize the generation and the temporal evolution of the pre-plasma. Here, the spatial expansion of the plasma's electron density can be characterized via interferometry. First investigations of plasma generation on solid aluminium targets have already been successfully carried out. Fig. 1 shows a measurement of the plasma expansion excited by a femtosecond pulse at

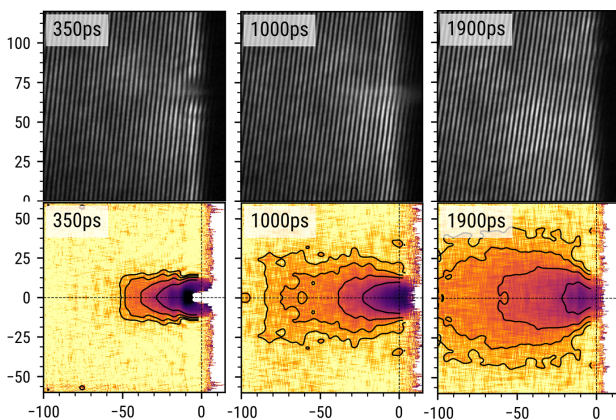


Figure 1: Exemplary interferometric characterization of a plasma excited by a femtosecond pulse at three different time steps.

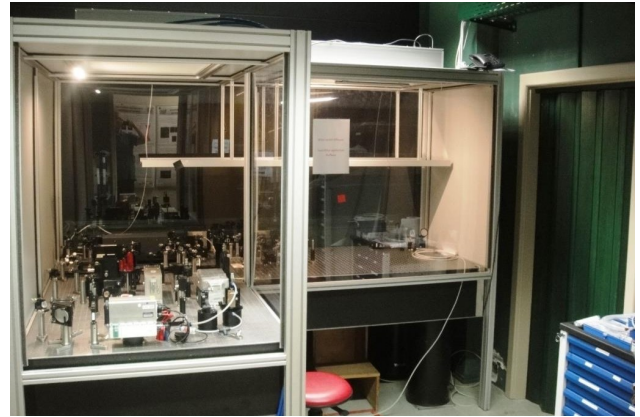


Figure 2: View into the plasma laboratory with the oscillator and the currently developed CPA system.

three different times.

Since –for safety reasons– it is not possible to operate this measurement setup during experimental operation, a dedicated plasma characterization laboratory is currently being established. To ensure a stable and clean laboratory environment, the laboratory rooms were equipped with optical tables, enclosures and flow boxes as can be seen in Fig 2. Furthermore, the laboratory is currently equipped with a Flint oscillator having a pulse duration of 50 fs, a power of 500 mW and a repetition rate of 76 MHz. A subsequent chirped-pulse-amplification (CPA) system, consisting of a pulse stretcher, a regenerative amplifier and a pulse compressor, is currently under development. Finally, the system will deliver pulses with an energy of about 2 – 3 mJ, a pulse duration of 100 fs with a repetition rate of 1 Hz, which can be used to generate and characterize the plasmas. It will also be possible to generate plasmas with pulses of nanosecond duration. While plasmas generated with femtosecond pulses only expand with an initial temperature, plasmas generated with nanosecond pulses are heated continuously. This leads to significantly different electron temperatures and thus to different propagation characteristics. For this purpose a Surelite with approx. 400 mJ at the fundamental wavelength (1064 nm) and a pulse duration of approx. 8 ns is available. Furthermore, the development of novel plasma diagnostics and probing schemes can be carried out in this laboratory, which will enable a better understanding of the laser-plasma interaction with high intensity lasers.

* Sebastian.Keppler@uni-jena.de

Intensity scaling limitations of laser proton acceleration in the TNSA-regime

S. Keppler^{*1,2}, N. Elkina², G. A. Becker², J. Hein^{1,2}, M. Hellwing², M. Hornung^{1,2}, M. Mäusezahl², C. Rödel^{1,2}, F. Schorcht¹, I. Tamer^{1,2}, M. Zepf^{1,2}, and M. C. Kaluza^{1,2}

¹Helmholtz Institute Jena, Germany; ²Institute of Optics and Quantum Electronics, FSU Jena, Germany

The availability of proton pulses accelerated to kinetic energies well above 1 MeV using novel, laser-based acceleration schemes has great potential for fundamental science and applications, e.g. in radiation therapy [1]. While proton energies in the multi-ten-MeV range are already available for applications, here, kinetic energies in excess of 200 MeV are required. This increase in energy is currently being addressed not only by a continuous development of the driving laser technology, but also by investigating and improving well-established acceleration mechanisms, e.g. the Target Normal Sheath Acceleration (TNSA). Here, electrons are accelerated by a high intensity laser pulse to relativistic energies within a pre-plasma formed at the front side of a solid target. The relativistic, ‘hot’ electrons then travel through the foil and form a space charge field at the back side. This field can ionize atoms from a surface contamination and the generated protons and ions can be accelerated along the target normal direction. To identify possibilities which further increase the maximum proton energy \mathcal{E}_p as a function of different experimental parameters, e.g. the laser pulse energy E_L , various scaling laws have been derived, e.g. $\mathcal{E}_p \propto E_L^\xi$ with ξ being the exponent of such a power law. In literature, exponents of $\xi = 0.5$ up to $\xi = 1$ have been reported. However, experiments verifying the different scalings have only been carried out with laser systems having peak powers of 10 . . . 400 terawatt. A confirmation of the scaling laws at the petawatt (PW) or even multi-PW level, where $\mathcal{E}_p > 100$ MeV is predicted, has still not been reported. This reveals a lack of comprehension of the acceleration dynamics, where additional experimental parameters might play an important role.

For this reason, we carried out an extensive experimental study in which we investigated the scaling of \mathcal{E}_p with the laser energy E_L (Fig. 1a-b). The study was carried out by varying different parameters, mainly the laser polarization and the temporal intensity contrast (see Ref. [2] for details). We were able to successfully reproduce the different scaling exponents reported in the literature by changing the contrast setting of the driver laser system [2]. However, \mathcal{E}_p only followed these scaling laws up to a certain threshold in laser energy. Above this threshold, the \mathcal{E}_p -curve flattens significantly (Fig. 1a-b). Thus the highest proton energies predicted by the scaling measurement at low intensity could not be reached leading to the assumption of a principle \mathcal{E}_p -limitation in the TNSA regime.

In Fig. 1d-h), both the evolution of the electric field $\mathcal{E}(x, t)$ generated on the target rear surface as well as the

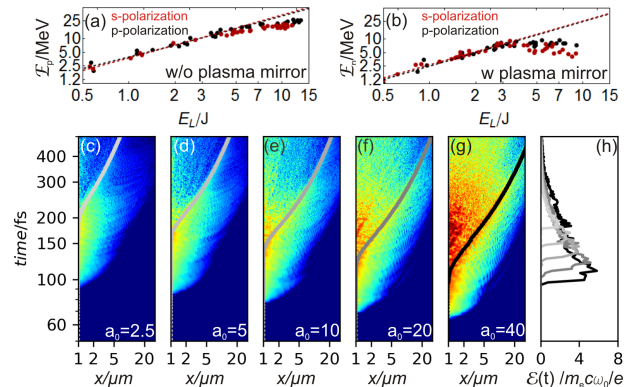


Figure 1: Measured scaling of maximum proton energy \mathcal{E}_p with (b) and without (a) plasma mirror for different polarization states; Evolution of the longitudinal \mathcal{E}_x -field on the target rear side for different values of a_0 (c-g) with trajectories of the fastest protons $x_{p_{\max}}(t)$ (continuous lines); (h) temporal line-outs.

position of the fastest protons $x_{p_{\max}}(t)$ (solid line) – extracted from 2D-PIC simulations – is depicted for different a_0 . Here we see, that with increasing laser energy, the laser pulse is sufficiently intense for longer time periods to produce ‘hot’ electrons. Thus, the rear-surface field is generated earlier and maintains its large amplitude longer. As a consequence, also the protons are accelerated earlier. Starting at the lowest intensities, increasing the laser pulse energy first leads to both an increase of the maximum field strength experienced by the protons and of the duration of the acceleration process. Consequently, this leads to a scaling exponent ξ , which is larger than can be expected when the maximum field strength alone is considered. However, if the intensity is increased further, the proton acceleration process starts earlier and protons are more distant from target when the field strength at the target rear surface is maximum. Consequently, the protons do not experience the increased field due to the increased laser energy and are therefore not accelerated to higher energies. In conclusion, the acceleration dynamic of the rear field significantly affects the intensity scaling ξ of \mathcal{E}_p eventually leading to a principle limitation of \mathcal{E}_p in the TNSA regime.

References

- [1] S. V. Bulanov et al., Phys. Lett. A **299**, 240 (2002).
- [2] S. Keppler et al., HI-Jena annual report (2018).

* Sebastian.Keppler@uni-jena.de

Simulations on ion acceleration in laser-driven foam-like plasma targets

Bin Liu and Matt Zepf

Helmholtz Institute Jena, Germany; GSI, Darmstadt, Germany

With the development of ultra-intense laser technology, laser-driven plasma-based ion acceleration has attracted much attention. High-energy high-quality controllable ion beams with particle energy hundreds of MeV have important applications in many areas including medical treatment of cancer, matter detection, nuclear physics, and high energy physics. Theoretical analysis and simulations have shown that foam-like plasma targets is promising for laser-driven high-energy ion acceleration. In relativistically-transparent regime, via ion wave breaking acceleration (IWBA), high-energy high-quality controllable ion beams can be produced. With the help of three-dimensional (3D) particle-in-cell (PIC) simulations, we have investigated laser-plasma interaction in such regime with practical laser plasma parameters. This work provides helpful information for the future experiments on high-energy ion acceleration.

When propagating an ultra-intense laser pulse in a foam-like plasma target in the relativistically-transparent regime, electrons are piled up at the laser front edge, forming a high density electron layer. A localized charge-separation field created in the region just behind of the electron layer co-moves with the laser front edge. Background ions can be self-trapped in the field via ion wave breaking [1] and then be accelerated to velocities far beyond the velocity of the laser front edge. The trapping happens localized close to the laser axis, resulting in highly directed ion beams. The output ion beam is adjustable by tuning the laser intensity or the plasma density. This allows designing controllable laser-plasma ion accelerators.

In laboratories, it is extremely difficult to prepare a foam-like target standalone with a relatively steep boundary which is crucial for breaking an ion wave at the initial stage. A foam-like carbon nano-tube target is usually produced on a solid-density substrate foil which usually makes the density of the foam have a step-like boundary on the foil side. Actually, IWBA can survive in such a double-layer target which combines a solid-density foil and a foam as long as the foil is thin enough so that the incident laser pulse can penetrate through it. This allows an experimental implementation of IWBA.

We have carried out 3D PIC simulations of IWBA for POLARIS laser parameters. The laser pulse is chosen as a

circularly polarized gaussian pulse with peak intensity

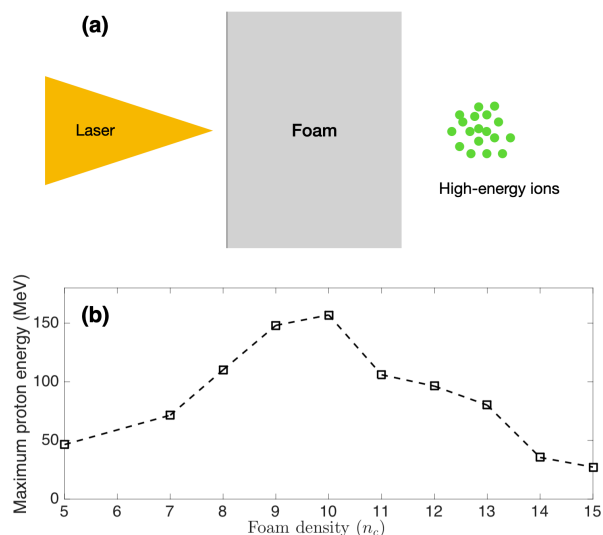


Figure 1: (a) A schematic plot: High-energy ions are produced by irradiating a POLARIS laser pulse on a foil-coated foam target. (b) Maximum proton energy versus foam density obtained from 3D PIC simulations.

$6 \times 10^{20} \text{W/cm}^2$ and total energy 16J. The target is assumed to be combined by a solid-density ultra-thin (areal density $1.4 \times 10^{17} \text{cm}^{-2}$) carbon foil and a uniform foam with a thickness 20 μm . The foam is assumed to be hydrogenated so that it is composed of fully ionised hydrogen and carbon atoms. We have found that the optimal proton acceleration happens when the foam density is about $1.1 \times 10^{22} \text{cm}^{-3}$ ($10n_c$, where n_c is the critical density) and the corresponding maximum proton energy is about 150 MeV, as is shown in Fig. 1.

Work supported by the John von Neumann Institute for Computing (NIC) on the GCS Supercomputer JUWELS at Jülich Supercomputing Centre (JSC).

References

- [1] B. Liu, J. Meyer-ter-Vehn, and H. Ruhl, *Physics of Plasmas* **25**, 103117 (2018).

Single Particle Detection System for the Strong-Field QED Experiment (E-320) at FACET-II

F. Salgado^{*1,2}, Harsh^{1,2}, S. Meuren³, C. Nielsen⁴, D. Reis³, C. Rödel^{1,2}, W. Ziegler^{1,2}, and M. Zepf^{1,2}

¹Helmholtz-Institut Jena, Germany; ²Institute of Optics and Quantum Electronics, Friedrich-Schiller-Universität Jena, Germany; ³SLAC National Accelerator Laboratory, Menlo Park, USA; ⁴Aarhus University, Aarhus, Denmark

The E-320 experiment at the SLAC National Accelerator Laboratory will investigate the nonperturbative regime of strong-field quantum electrodynamics by the interaction of an ultra-relativistic electron beam with a strong laser field. For the envisaged laser and electron parameters at SLAC, 10-100 pairs are produced per laser pulse in the range of 1-6.5 GeV. The main diagnostic for the generated positrons is a Cherenkov calorimeter, which is designed and built by the Helmholtz Institute Jena.

Strong-field quantum electrodynamics (SFQED) models have been widely studied theoretically [1]. Examples of physical processes from the interaction between relativistic electrons and high energy photons are radiation reaction and electron-positron pair creation (trident and Breit-Wheeler process). Experiments demonstrating SFQED effects have been performed, for example, at SLAC [2] and, recently, at the Rutherford Appleton Laboratory [3]. The proposed E-320 experiment at FACET-II will explore a regime of interaction where the perturbative treatment of a strong electromagnetic (laser) field breaks down, i.e., the electrons start to interact coherently with many photons. Therefore, a reliable detection system for GeV-particles produced by SFQED processes is required.

Here, we present a detection system composed of pixelated crystals arrays and a Cherenkov calorimeter designed to fit into the space constraints of the FACET-II facility and capable of tracking and diagnosing single GeV-positrons with reduced background signal from scattered high energy radiation for the upcoming E-320 experiment at FACET-II. Two LYSO crystal arrays are utilized for the tracking of single positrons and exhibit a sufficiently rapid temporal response to allow for the suppression of scattered radiation (e.g. from the beam dump) by temporal gating. Figure 1 shows the proposed single particle detection system.

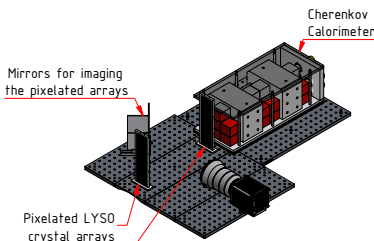


Figure 1: 3D drawing of the proposed detection system.

The Cherenkov detector consists of seven F2 lead-glass

* felipe.salgado@uni-jena.de

channels, where a photomultiplier tubes is attached on its rear, and aluminum frames to hold the parts together.

Monte-Carlo simulations of the detection system were performed using GEANT4. In the simulations were implemented the LYSO screens and the Cherenkov detector, the FACET beamline with radiation shielding, and, the electron spectrum after the electron-laser interaction. Figure 2 presents the number of detected photons (sum of all PMTs hits) for a total of 1000 simulation events. One event consists of a single GeV-positron interacting with the proposed detection system.

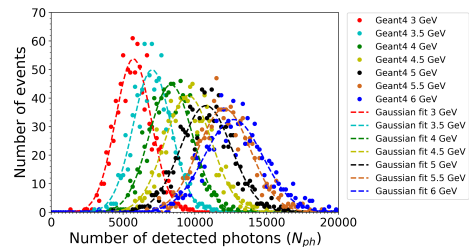


Figure 2: Expected total number of detected photons on the PMTs after a single GeV-positron interacted with the F2 lead-glass of the calorimeter. The total number of events, i.e. the number of Monte Carlo simulations, are equal to 1000.

The result presented in Fig. 2 shows an increase in the number of detected photons by the PMTs for higher energies of single positrons. More photons being detected by the PMTs leads to a higher current signal generated by the PMT devices which can be associated with the energy of the incoming positron.

In conclusion, the proposed single particle detection system is capable of diagnosing single GeV-positron hits as required by the experiment E-320. The calibration of the system will be performed at the high-power laser system JETI200 at the Helmholtz Institute Jena before the SFQED experiment at FACET-II.

References

- [1] V. I. Ritus, J. Sov. Laser Res. **6**, 497 (1985); A. Di Piazza *et al.*, Phys. Rev. A **99**, 022125 (2019).
- [2] D. L. Burke *et al.*, Phys. Rev. Lett. **79**, 1626 (1997); C. Bamber *et al.*, Phys. Rev. D **60**, 092004 (1999); C. Bula *et al.*, Phys. Rev. Lett. **76**, 3116 (1996).
- [3] K. Poder *et al.*, Phys. Rev. X **8**, 031004 (2018); J. M. Cole *et al.*, Phys. Rev. X **8**, 011020 (2018).

Photon and Particle Spectroscopy

X-ray polarimetry with artificial four bounces diamond channel cuts

H. Bernhardt^{1,2}, A. T. Schmitt², B. Grabiger¹, B. Marx-Glowna^{1,2}, R. Loetzsch^{1,2}, H. C. Wille⁴, D. Bessas³, A. I. Chumakov³, R. Ruffer^{3,4}, R. Roehlsberger^{1,2,4}, T. Stoehlker^{1,2}, I. Uschmann^{1,2}, G. G. Paulus^{1,2}, and K. S. Schulze^{*1,2}

¹Helmholtz Institute Jena, Germany; ²Friedrich-Schiller-Universität Jena, Germany; ³ESRF, Grenoble, France; ⁴DESY, Hamburg, Germany

We report on the use of synthetic single-crystal diamonds for high definition x-ray polarimetry. The diamonds are precision mounted to form artificial channel-cut crystals (ACCs). Each ACC supports four consecutive reflections with a scattering angle $2\Theta_B$ of 90° (Figure 1). We achieved a polarization purity of $3.0 \cdot 10^{-10}$ at beamline ID18 of the European Synchrotron Radiation Facility (ESRF). When the x-ray beam's horizontal divergence was reduced through additional collimation from $17\mu\text{rad}$ to $8.4\mu\text{rad}$, the polarization purity improved to $1.4 \cdot 10^{-10}$. Precision x-ray polarimetry thus has reached the limit, where the purity is determined by the divergence of the beam. In particular, this result is important for polarimetry at 4th generation x-ray sources, which provide diffraction-limited x-ray beams. The sensitivity expected as a consequence of the present work will pave the way for exploring new physics like the investigation of vacuum birefringence.

A particularly demanding application of x-ray polarimeters, which actually sets the benchmark for our efforts, is the detection of the birefringence of vacuum polarized by an extremely strong laserfield [1]. Based on ideas of Euler and Heisenberg, the effect was already predicted in the early days of QED. Like in birefringent crystals, the induced optical anisotropy causes a difference between the refractive indices parallel and perpendicular to the electric or magnetic field vector.

Here we improved the polarization purity compared to the best value which was achieved with silicon and six reflection in a channel cut. In both cases the 400 - Bragg reflection were used. The photon energy of the polarized radiation was 9839 keV.

Moreover, the choice of an appropriate crystal material is imperative to reduce multiple-wave diffraction. The influence of multiple-wave diffraction grows with the 4th power of the atomic number Z [2, 3]. Silicon with $Z = 14$ is advantageous because perfect crystals with minimal impurities are readily obtainable and can easily be machined. For the challenge of detecting the birefringence of vacuum, the highest polarization purity at the highest photon energy is desired. Obviously, diamond with $Z = 6$ is an attractive material (see Figure 2).

References

[1] F. Karbstein, H. Gies, M. Reuter, and M. Zepf, Vacuum birefringence in strong inhomogeneous electromagnetic fields,

* kai.sven.schulze@uni-jena.de

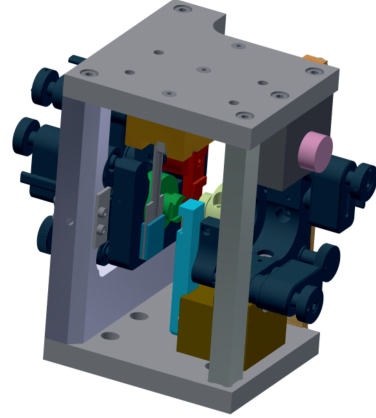


Figure 1: The mounting of the four diamond crystals consist of piezo driven mirror mounts (dark grey) which are fixed within an invar skeleton (grey). An X-ray photodiode (dark blue) can be moved along the artificial channel cut in order to align each diamond crystal.

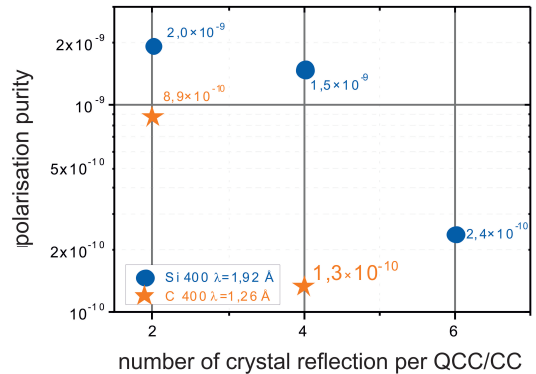


Figure 2: The polarization purity of x-ray polarimeters measured for different number of bounces and by using silicon and diamond crystals. According to [3] the purity is decreasing for lower atomic number Z .

Physical Review D 92, 071301 (2015).

[2] H. Bernhardt, A. T. Schmitt, B. Grabiger, B. Marx-Glowna, R. Loetzsch, K.S. Schulze, et al. Ultra-high precision x-ray polarimetry with artificial diamond channel cuts at the beam divergence limit, Phys. Rev. Research, accepted, 2020.

[3] K. S. Schulze, Fundamental limitations of the polarization purity of x rays, APL Photonics 3, 126106 (2018).

S-EBIT Facility: status report

S. Trotsenko^{1,2,#}, T. Morgenroth^{1,3}, O. Herdrich^{1,3}, F. Kröger^{1,3}, A. Gumberidze², G. Weber^{1,2}, A. Fleischmann⁴, D. Hengstler⁴, S. Allgeier⁴, Ch. Enss⁴, R. Schuch⁵ and Th. Stöhlker^{1,2}

¹Helmholtz Institute Jena, Germany; ²GSI, Darmstadt, Germany; ³FSU, Jena, Germany;
⁴Ruprecht-Karls-Iniversität Heidelberg, Heidelberg, Germany; ⁵University of Stockholm, Stockholm, Sweden

The cryogenic electron beam ion trap facility based on the Stockholm EBIT [1], set two experimental concepts (S-EBIT-I and S-EBIT-II), serving as R&D platforms and the sources of ions/photons for the SPARC/FARI and HI Jena. The S-EBIT-I is already supplying the experiments and instrumentation with the photons from up to the mid-Z ions, while the S-EBIT-II is being commissioned with the goal of reaching the highest charge states of high-Z ions.

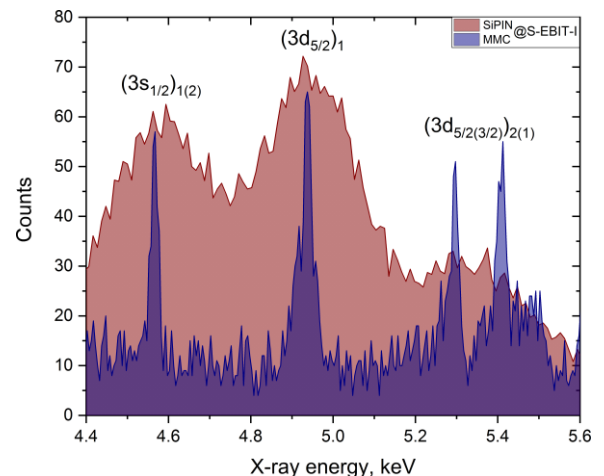
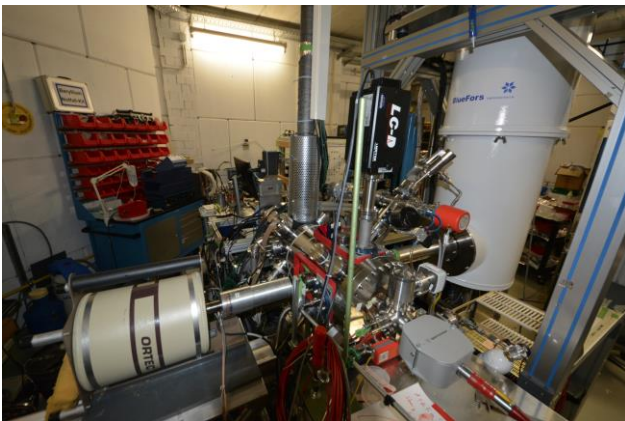
The S-EBIT-I among all serves as a benchmarking setup in the combination with the on-going FAIR related developments driven by the Helmholtz Institute Jena, e.g. x-ray optics [2], magnetic micro-calorimeters [3] etc. Here, recent efforts have been devoted to the activities in support of the very first experiments to be carried out at FAIR facility, namely the Lamb-shift experiment at the CRYRING@ESR [4]. In this campaign, a magnetic micro-calorimeter (MMC) of a high energy-resolution has been set up at the S-EBIT-I in combination with a data acquisition system based on novel data processing algorithms [5]. The experimental setup can be seen in the Figure (left) below. The EBIT was operated with a 10 keV electron beam and a current of 25 mA compressed by 1 Tesla magnetic flux density and provided highly charged iron and barium ions for a high-precision x-ray spectroscopy in a few keV region of interest. As an example, the below figure (right) shows the x-ray spectrum obtained by preliminary analysis. The L x-ray transitions of highly charged barium (measured by the MMC and a SiPIN-diode detector) are indicated. The data

analysis is in progress. These activities lead to a number of improvements of the MMC operation, readout, data acquisition as well as its signal processing algorithms, which are crucial for the upcoming FAIR experiments (more details can be seen in a contribution these reports by M.O. Herdrich et al.). In addition to the MMC, the application of the x-ray optics [2] is of particular interest for optimizing the measurement efficiency in a broad range of x-ray spectroscopic studies. Ultimately, the combination of such optics with the MMC will serve this purpose.

In the meantime, the S-EBIT-II has been undergoing further upgrades, e.g. successful test of the new prototype (IrCe-based) electron gun, achieved a stable operation of the superconducting magnet near its maximum flux density, which was enabled by the optimized vacuum and the cryogenic systems. In the upcoming months, we aim on completing the mechanical and electrical setup for the high-voltage cage with all the safety interlocks and measures for the first commissioning of this EBIT.

References

- [1] R. Schuch et al., JINST5, C12018 (2010).
- [2] S. Trotsenko et al., HI Jena Scientific Report 2018.
- [3] S. Kempf et al., Superc. Sci. Tech. 28, 045008 (2015)
- [4] M. Lestinsky et al., Eur.Ph.J.Sp.T.225,797-882 (2016)
- [5] M. O. Herdrich et al., X-ray spect. 49, 184-187 (2020).



S.Trotsenko@gsi.de

A high-photon-flux narrow bandwidth XUV source for experiments at ion storage rings

V. Hilbert^{1,2}, M. Tschernajew^{1,2}, R. Klas^{1,2}, H. Lin^{1,4}, P. Gierschke^{2,3}, J. Limpert^{1,2,3},
and J. Rothhardt^{1,2,3#}

¹Helmholtz Institute, Jena, Germany; ²Institute of Applied Physics Jena, Germany; ³Fraunhofer Institute for Applied Optics and Precision Engineering, Jena, Germany ⁴GSI, Darmstadt, Germany

A high harmonic source generating more than 10^{13} XUV photons per second per harmonic was developed. To apply this source in experiments at heavy ion storage rings, a 3-stage differential pumping system was developed that allows windowless and thereby lossless coupling of the generated XUV photons to the storage ring. In a first part of a proof of principle experiment at CRYRING@GSI XUV photons were successfully delivered to the storage ring and spatially overlapped with the ions.

Up to date table-top fiber laser systems enable the scientific community to execute a variety of experiments that were formerly confined to large scale instruments such as free-electron lasers and synchrotron light sources. Amongst others the development of high harmonic generation (HHG) sources opened access to a variety of photon hungry XUV applications that require laser like radiation. To apply such an XUV source for spectroscopy of highly-charged ions at an ion storage ring it has to be of table-top size, remotely controllable and in addition exhibit a narrow bandwidth.

We designed and have setup a dedicated XUV source for this purpose as shown in fig. 1. A robust and compact fiber laser system at a fundamental wavelength of 1030nm acts as the driving system. The fundamental IR pulses are then frequency doubled and focused into an Argon jet to generate the harmonics. The photon flux of the 9th harmonic at 21 eV yields 2.0×10^{13} Photons per second and the 11th harmonic at 27 eV yields 6.5×10^{13} Photons

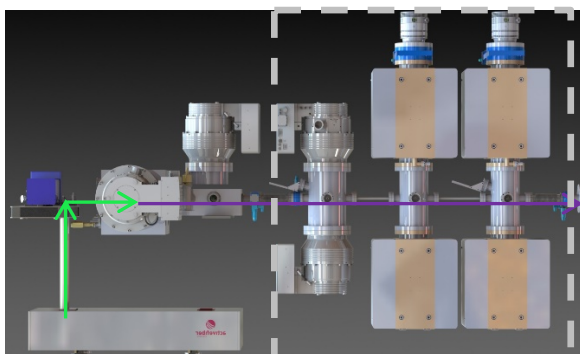


Figure 1: Scheme of the HHG source setup combined with the differential pumping unit. The path of the laser is marked green (driving laser) and purple (XUV photons). The differential pumping section is shown in the grey rectangle. [2]

[#]J.Rothhardt@gsi.de

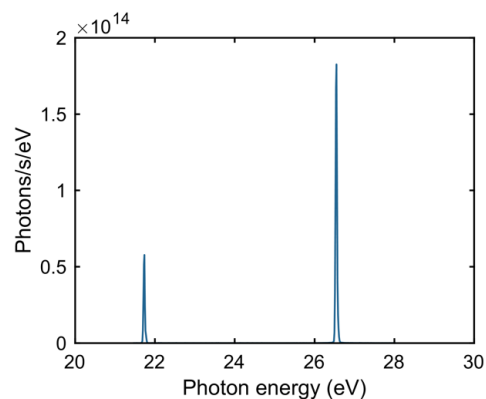


Figure 2: Spectra of the 9th (21.5 eV, i.e. 57.6 nm) and the 11th (26.7 eV, i.e., 46.4nm) harmonic [1].

per second (fig. 2) at a repetition rate of 334kHz. Together with the measured narrow energy bandwidth of $\Delta E/E=7.5 \cdot 10^{-4}$ the developed HHG XUV source is a powerful table-top turn-key tool for a number of applications [3]. Photoionization experiments making use of the Doppler upshift at ion storage rings or pump probe experiments on cooled ions stored in ion traps (EBIT) are feasible.

To apply the generated XUV harmonics at ion storage rings we developed a dedicated vacuum coupling unit. It comprises of an efficient multi stage pumping system to decrease the absolute pressure over three stages from $1.5 \cdot 10^{-5}$ mbar to $1 \cdot 10^{-11}$ mbar. An open aperture of 10mm diameter guarantee lossless XUV- transport to the storage ring target ions. The developed XUV source was already successfully run during the first shifts of a granted beam time at CRYRING@GSI together with the vacuum coupling unit. The generated XUV beam was transported to the storage ring and overlapped with the ion beam.

In future these promising results will open exciting possibilities e.g. spectroscopy, photoionization or lifetime pump probe measurements on highly charged ions [3, 4].

Work supported by BMBF grant 05P19SJFA.

References

- [1] V. Hilbert, et al. AIP Advances **10**, 045227 (2020).
- [2] M. Tschernajew, et al., Vacuum 109443 (2020).
- [3] M. Lestinsky, et al., Eur. Phys. J. Spec. Top. **225**, 797 (2016).
- [4] J. Rothhardt, et al., X-Ray Spectrometry **49**, 165 (2020)

New Setup for X-Ray Spectroscopy at the CRYRING@ESR Electron Cooler

F. M. Kröger^{1,2,3} #, G. Weber^{1,2}, O. Forstner^{1,2,3}, A. Gumberidze², M. O. Herdrich^{1,2,3}, M. Lestinsky², A. Kalinin², Th. Köhler^{1,2,3}, E. Menz^{1,2,3}, P. Pfäfflein^{1,2}, U. Spillmann², and Th. Stöhlker^{1,2,3}

¹Helmholtz Institute Jena, Germany; ²GSI, Darmstadt, Germany; ³IQO, Friedrich-Schiller-Universität, Jena, Germany

X-ray spectroscopy at the electron cooler of CRYRING@ESR offers the unique possibility to study the photon emission in the interaction of decelerated highly-charged ions with an ultracold electron beam [1]. One of the flagship experiments is the precise determination of the 1s Lamb shift in U^{91+} . The preparation of the experiment led to the development of several new experimental installations. In this report we present vacuum chambers for mounting beryllium x-ray windows at the electron cooler as well as a moveable holder for calibration sources.

Different experiments being conducted at the CRYRING electron cooler need the interaction region of the ion beam and the electron beam to be accessible either in the optical or in the x-ray regime. This requires the mounting of windows optimized for the specific wave-length regime, while at the same time the strict UHV requirements make it desirable to minimize the need to break the ring vacuum.

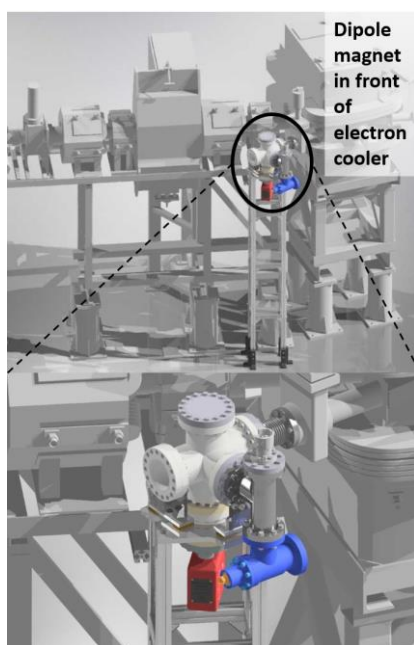


Figure 2: Drawing of the chamber at the 180° port of the CRYRING electron cooler. A valve between the dipole magnet and the chambers allows a separation from the CRYRING vacuum to exchange the windows (e.g. switching between optical and x-ray windows).

To facilitate the exchange of the windows without interfering with the CRYRING vacuum, dedicated vacuum chambers were developed for both viewports of the electron cooler section. The chamber at 180° is depicted in Figure 1. Its main part is a 5-way CF100 cross with the following installations: a vacuum pocket for beryllium x-ray windows, a combined NEG and ion getter pump as well as a valve and an ion gauge are installed. The chambers can be separated from the CRYRING by a UHV valve to enable the exchange of the windows without breaking the vacuum of the storage ring. Moreover, the chambers are equipped with tailor-made heating jackets for vacuum bakeout.



Figure 1: Lead-shielded box with moveable holder for a reference gamma source. The holder is synchronized with the operation of the storage ring to place the source in front of the detector whenever the setup is not in measurement mode.

As the 1s Lamb shift experiment requires a rigorous and continuous energy calibration of the x-ray detectors, it is planned to place suitable reference gamma sources in front of the detectors during periods when there is no ion beam in the storage ring. To this purpose a lead-shielded box with a moveable source holder was developed, which is presented in Figure 2. It enables a continuous calibration that is synchronized with the measurement operation of the CRYRING. This box will be mounted to the vacuum chamber in front of the x-ray window.

We acknowledge financial support by BMBF for APPA R&D, project number 05P19SJFAA.

References

- [1] M. Lestinsky. et al., Eur. Phys. J. Spec. Top. **225**, 797 (2016)

felix.kroeger@uni-jena.de

Resonant photoexcitation of highly charged ions at synchrotron light sources with the compact electron beam ion trap PolarX-EBIT

S. Bernitt^{*1,2,3,4}, S. Kühn⁴, R. Steinbrügge⁵, C. Shah^{6,4}, P. Micke⁷, M. Togawa⁴, J. Stierhof⁸, M. Leutenegger⁶, N. Hell⁹, G. V. Brown⁹, J. R. Crespo López-Urrutia⁴, and Th. Stöhlker^{1,2,3}

¹Helmholtz-Institut Jena, Germany; ²GSI, Darmstadt, Germany; ³IOQ, Friedrich-Schiller-Universität Jena, Germany; ⁴Max-Planck-Institut für Kernphysik, Heidelberg, Germany; ⁵DESY, Hamburg, Germany; ⁶NASA Goddard Space Flight Center, Greenbelt, USA; ⁷PTB, Braunschweig, Germany; ⁸Dr.-Karl-Remeis-Sternwarte and ECAP, Bamberg, Germany; ⁹LLNL, Livermore, USA

The compact electron beam ion trap PolarX-EBIT provides a target of trapped highly charged ions for x-ray photon beams at the PETRA III synchrotron light source. It has been used in multiple experiments for high-precision spectroscopy, as well as for the characterization of photon beams at different beamlines.

An electron beam is used to stepwise ionize neutral atoms into high charge states. The ions are produced at rest and held at the trap center. A compact design and reduced complexity, compared to conventional electron beam ion traps, is achieved by using permanent magnets to supply the magnetic field necessary to compress and guide the electron beam. Additionally, a novel off-axis electron gun is employed, which allows the synchrotron photon beam to pass through the apparatus, while being axially overlapped with the cloud of trapped ions [1].

Undulators combined with high-resolution monochromators, which are available at multiple beamlines, are used to select the energy of photons interacting with the ions. By scanning this energy and simultaneously recording the ion fluorescence caused by resonant excitation of electronic transitions, it is possible to measure transition energies and other atomic structure parameters with high accuracy.

An experiment focused on measuring the intensity ratio of two $2p-3d$ transitions in Ne-like Fe^{16+} was conducted at beamline P04. Values for this ratio predicted by theory have consistently disagreed with laboratory experiments and astronomical observations. A spectral resolution ten times better than previous experiments was achieved, resulting not only in the most accurate measurement of the line ratio yet, confirming the discrepancy, but also in the rejection of all proposed explanations [2]. Data analysis for a follow-up experiment with improved resolution and statistics is still in progress.

Other experiments were performed at beamlines P04 and P01, providing atomic data for high charge states of oxygen and medium charge states of iron, relevant for the analysis of x-ray observatory data, and for benchmarking atomic structure theory. One such measurement revealed surprisingly strong two-electron-one-photon transitions [3].

The PolarX-EBIT has also been used to provide high-precision calibration of other experiments [4] and to characterize the apparatus profile of the P04 beamline. Experiments were conducted to explore the possible use of

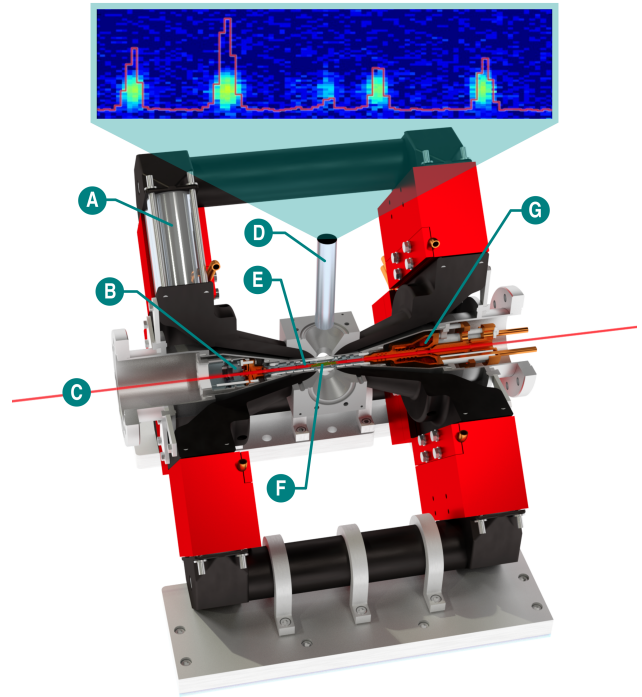


Figure 1: PolarX-EBIT with permanent magnets (A), off-axis electron gun (B), x-ray photon beam (C), fluorescence detector (D), trap electrodes (E), cloud of trapped ions (F), and electron collector (G). A typical spectrum recorded is shown at the top.

electronic transitions in highly charged ions as future x-ray wavelength standards.

The PolarX-EBIT was funded by BMBF through project 05K13SJ2 and was supported by MPG and PTB. Part of this work was performed by LLNL contributors under contract DE-AC52-07NA27344 and was supported by NASA grants to LLNL.

References

- [1] P. Micke *et al.*, Rev. Sci. Instrum. **89**, 063109 (2018).
- [2] S. Kühn *et al.*, <https://arxiv.org/abs/1911.09707> (accepted for publication in Phys. Rev. Lett., 2020).
- [3] M. Togawa *et al.*, <https://arxiv.org/abs/2003.05965> (submitted to Phys. Rev. Lett., 2020).
- [4] M. Leutenegger *et al.*, <https://arxiv.org/abs/2003.13838> (submitted to Phys. Rev. Lett., 2020).

*sven.bernitt@mpi-hd.mpg.de

Characterization of a YAP:Ce scintillator for ion detection

B. Zhu^{1,3} #, P. Pfäfflein^{1,3}, C. Hahn^{1,3}, H. Lin², G. Weber^{1,2}, and Th. Stöhlker^{1,2,3}

¹Helmholtz Institute Jena, Germany; ²Institute for Optics and Quantum Electronics, Friedrich Schiller University Jena, Germany; ³GSI, Darmstadt, Germany

Recently two scintillation detectors based on Ce-doped yttrium aluminium perovskite (YAP:Ce) were developed for ion detection in CRYRING@ESR. In this report we present a systematic study of the degradation of the scintillation material as a result of ion bombardment.

The recently commissioned CRYRING@ESR allows the storage of highly-charged ions at low kinetic energies down to a few 10 keV/u. For detection of these ions windowless detectors are necessary as the stainless steel foils of the multi-wire proportional-counter (MWPC) detectors routinely used at the ESR cannot be penetrated by ions with less than roughly 10 MeV/u. To this purpose recently two scintillation detectors based on YAP:Ce were developed. This scintillator material is well-known to be radiation-hard and UHV-compatible [1,2,3,4]. However, to our knowledge its performance for detection of low-energy ions was not systematically studied so far.

In the following we report on a series of measurements at the 3 MV JULIA accelerator operated at the University of Jena, where the relative light yield and radiation damage was studied for a broad range of low-charged, low-energy ion species, namely from C⁴⁺ to Au⁴⁺. A schematic view of the experimental setup is shown in Fig. 1. The scintillator is coupled to a photodetector which converts impinging scintillation photons into an electric signal. The electronic output signals from the photodetector are typically fed into a preamplifier, shaping amplifier, multichannel analyzer, and computer in pulse-height analysis.

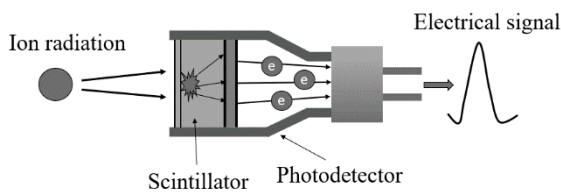


Figure 2: Schematic sketch of a typical scintillation detector.

Using a digital oscilloscope, we recorded a few thousand events for a number of different cumulated ion depositions on 1x1 mm² spots of the scintillator. The aim is to see at what ion deposition level the detector signals starts to degrade and at what level the signals can no longer be discriminated from the noise/background signals. Our results

for 10 MeV total kinetic ion energy are depicted in Fig. 2, where the pulse strength is plotted as a function of the amount of ions already deposited on the scintillator. By comparing the signals resulting from different ion particles, we find that for different ion species with the same kinetic energy, light ion species produce higher light yields and show a higher damage threshold compared to heavy ions. The most probable cause is that light ions transfer more of their kinetic energy into electron excitations that lead to the emission of scintillation light, but do not result in a damage of the crystal structure. In contrast, heavy ions transfer a greater fraction of their energy into modifications on the crystal structure, leading to radiation damage but not so much to electron excitation and subsequently light yield.

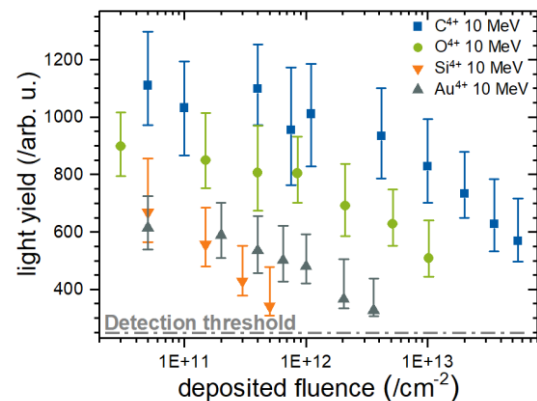


Figure 1: Light output of activated inorganic scintillator YAP:Ce under bombardment by different ion beams with the same kinetic energy. The light output is defined by the area under detector signal.

We acknowledge financial support by the Chinese Scholarship Council.

References

- [1] G. Miersch et al., NIM A 369, 277 (1996)
- [2] W. Klamra et al., NIM A 444, 626 (2000)
- [3] S. Westman et al., NIM A 481, 655 (2002)
- [4] W. Q. Wen et al., NIM B 317, 731 (2013)

binghui.zhu@uni-jena.de

Phase-volume Effect for Few-cycle Light-matter Interactions

Yinyu Zhang^{1,2#}, Danilo Zille^{1,2}, Dominik Hoff^{1,2}, Philipp Wustelt^{1,2}, Daniel Würzler^{1,2},
Max Möller^{1,2}, A. M. Saylor^{1,2}, and Gerhard G. Paulus^{1,2}

¹Helmholtz Institute Jena, Germany; ²Institut für Optik und Quantenelektronik, Jena, Germany

Few-cycle laser beams are known since more than 20 years. Much less known is the complex phase distribution in the few-cycle focus and even less known are the implications in attosecond and strong-field physics. In this project, we investigated the importance of the non-Gouy phase-volume effect for few-cycle light-matter interactions.

The phase behaviour of focused broadband lasers, which was predicted [1] and recently directly probed in a highly specialized measurement [2], is very different and significantly more complex than the well-known Gouy phase for monochromatic beams. Thus, one should expect that there are profound consequences for all broad-band laser-induced dynamics, in particular in cases where the interaction volume is comparable to the focal size, as is inevitable for isolated attosecond pulse generation, high-harmonic generation, terahertz emission, and electron dynamics in atomic, molecular, and solid-state systems.

In this project, we investigated and demonstrated the importance of this non-Gouy phase induced “phase-volume effect”, i.e., the complex spatial distribution of the carrier-envelope phase (CEP) of few-cycle laser pulses, has an on measuring effect on interpreting the CEP-dependent dynamics.

First, we examined measurements and simulations of CEP-dependent strong-field ionization to quantify and illustrate the characteristics of this effect. We applied ~ 12 -fs, 1800-nm pulses to ionize xenon atoms around the barrier-suppression intensity (0.8×10^{14} W/cm²). The CEP-dependent photoelectron spectra were measured by a high-resolution time-of-flight spectrometer. The spatial asymmetry was obtained by analysing the normalized difference between the photoelectron spectra emitted to opposing directions along the laser polarization axis. The measured asymmetry (Fig. 1a) was compared to simulated results (Fig. 1b, 1c and 1d) calculated from a standard one-dimensional time-dependent Schrödinger equation simulation. One can clearly see the blurring of the phase-dependence due to the intensity- and phase-volume effect. The strength of the asymmetry for each energy region becomes smaller when the focal phase is included in the simulation, producing a better agreement with the measurements.

The carrier-envelope phasemeter (CEPM) traces, which are based on the measurement of high-order photoelectron emission, allowing for single-shot CEP and pulse duration measurement, also shows the same quality of the phase effect. A so-called parametric asymmetry plot (PAP) can be obtained by plotting two asymmetries in different energy regions as x - and y -coordinates, shown in Fig. 1e and 1f. Including the focal phase in the theoretical model reduces the radius of the PAP due to the averaging effect on the CEP. Additionally, the agreement between the measurements at both laser wavelengths (750 nm and 1800 nm) and

the numerical calculations including the focal phase validates our theoretical treatment. This allows more accurate modelling and interpretation of the CEP-dependent few-cycle laser-induced processes, as well as more precise determination of the CEP of the laser pulse.

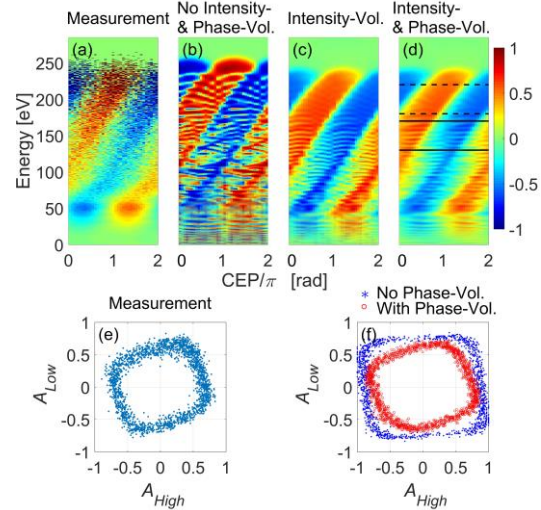


Fig. 1 (a) Measured asymmetry with $\tau = 11.8 \pm 0.5$ fs pulses (b) Simulated asymmetry excluding the intensity- and phase-averaging effect with 12-fs pulses with $I_0 = 0.8 \times 10^{14}$ W/cm² (c) Simulated asymmetry including only the intensity-volume effect. (d) Simulated asymmetry including both effects. (e) Measured PAP by a CEPM with 10.4 ± 0.5 fs pulses at 1800 nm. (f) Simulated PAPs with 10-fs pulses. The blue and red dots represent the case with and without the phase-volume effect, respectively. Two energy regions within black dashed lines and black solid lines in (d) are selected to obtain the PAPs. [3]

Building upon the knowledge of the phase effect in strong-field ionization, we further formulated a more general description of the impact of the focal phase for laser-matter interactions with different nonlinear intensity dependencies to answer the fundamental question: If, when and how much should one be concerned about the phase-volume effect?

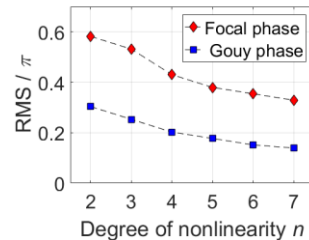


Fig. 2 RMS of the phase distribution for light-matter interactions with different degrees of nonlinearity, n , with the probability of events, $P \sim I^n$, where I is the laser intensity. [3]

[1] M. A. Porras, *Phys. Rev. E* **65**, 026606 (2002)

[2] D. Hoff, *et. al. Nat. Phys.* **13**, 947 (2017).

[3] Y. Zhang, *et. al. Phys. Rev. Lett.* **124**, 133202 (2020)

XUV source diagnostics with a single diffraction pattern

F. Tuitje^{1,2,#}, T. Helk^{1,2}, A. Dehlinger³, H. Stiel³ and C. Spielmann^{1,2}

¹Helmholtz Institute Jena, Germany; ²Institute for Optics and Quantum Electronics Jena, Germany; ³Institute for Optics and Atomic Physics Berlin, Germany

Weak and partially coherent sources based on laser-driven plasmas emitting in the extreme ultraviolet (XUV) are hard to characterize with diffraction-based methods like the double slit. Here we demonstrate a new method which allows to characterize the source's spatial coherence and the axial jitter via a long-exposed diffraction pattern evaluated with a refined numerical method. For water-window XUV source at 2.7nm we estimated the coherent fraction of the beam area to 7.5 % with a total axial jitter amplitude of 160 μ m.

We report on a diagnostics tool for weak and partially coherent high energy XUV sources, where common techniques, such as Young's double slit or SCIMITAR [1] fail due to low count rates and small scattering angles. A long time exposed diffraction pattern of a laser-driven, plasma-based XUV source, located at the Berlin Laboratory for Innovative X-Ray Technologies (BLIX) has been recorded. The image contains information about spatial coherence and jitter of the light emitting plasma spot, which we want to retrieve. The axial jitter of the spot causes warping-like effects (see fig. 1, measurement) due to the imaging system, described in [2]. The high spectral purity $\lambda/\Delta\lambda = \sim 10000$ of the emitted Ly α line (2.48 nm) of highly ionized nitrogen rules out spectral overlay as the accountable effect for warping. Partial coherence however leads to a significant normally distributed background and blurring of the diffraction pattern's features. We developed a numerical model to simulate the far-field diffraction of a known object, taking into account jitter and coherent diameter, to generate a 4D matrix of patterns. For the same coherence, patterns with different axial jitter amplitude were mixed, resulting in the pattern matrix shown in Fig. 1(overlay). Image correlations between the generated patterns and the measured long-exposure time image results in a 2D correlation matrix. Finding the maximum reveals the parameter-set which fits best to the experimental conditions. The parameter recovered via this framework for the nitrogen plasma-source reveal a total jitter amplitude of 160 \pm 10 μ m with a coherent diameter of 11 \pm 1 μ m, resulting in an illuminated area to coherent area ratio of 7.5 %.

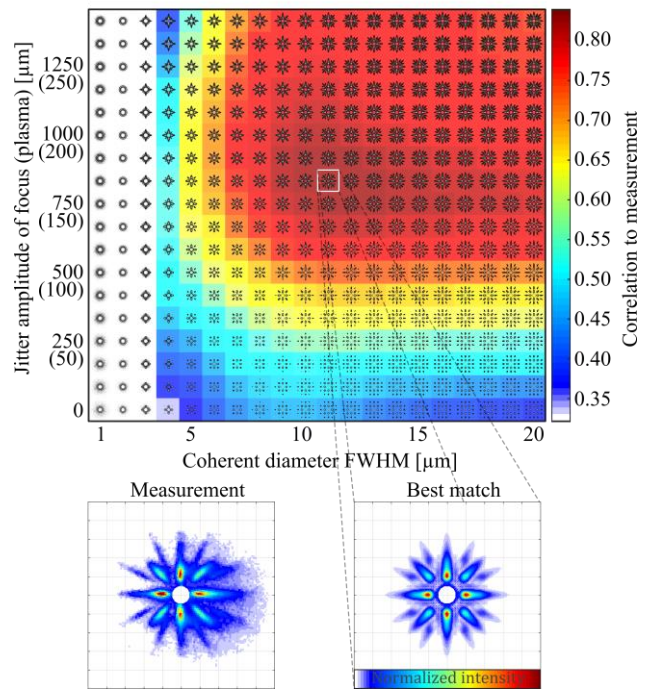


Figure. 1: Calculated diffraction pattern matrix varying in axial jitter and coherent diameter (overlay) with the corresponding correlation factors to the measurement. The jitter values in brackets were calculated via the lens equation. The shown diffraction patterns were freed from the central high-intensity spot for the sake of clarity.

We acknowledge support by the Federal State of Thuringia and the European Social Fund (ESF) Project 2018 FGR 0080.

References

- [1] D. T. Lloyd et al. Opt. Lett. **38**, 7 (2013).
- [2] H. Legall et al. Opt. Express **20**, 16 (2012).

Frederik.tuitje@uni-jena.de

This work will also contribute to the GSI annual Report 2019

Strong-field physics with phase-stable mid-IR pulses

M. Kübel[#], S. Skruszewicz, P. Wustelt, Y. Zhang, D. Hoff, D. Würzler, A. M. Sayler
R. Hollinger, C. Spielmann, and G. G. Paulus

¹Helmholtz Institute Jena, Germany; ²Institute of Optics and Quantum Electronics, Jena, Germany

The field of strong-field and attosecond laser physics has recently seen a significant shift towards longer wavelengths. Ultrashort laser pulses in the mid-infrared (MIR) spectral range hold the promise to push high harmonic generation (HHG) towards the soft x-ray regime, and enable molecular imaging experiments with ultrahigh spatial and temporal resolution. Realizing the full potential of ultrashort MIR pulses, however, will require efficient methods for the measurement of the carrier-envelope phase (CEP). In order to aid development of such methods, we have performed phase-resolved measurements of strong-field effects in atoms, molecules and solids using the CEP-stable MIR laser at the ELI-ALPS laser facility. Our measurements of phase-dependent above-threshold ionization provide new insights into the mechanisms leading to asymmetric electron ejection, relevant for CEP measurements. Moreover, we show that HHG from wide-band semiconductors, such as ZnO, represents a convenient and cost-effective route to CEP measurements of few-cycle MIR laser pulses.

The interaction of intense laser light with gaseous media is characterized by the quiver motion of electrons in the strong oscillating electric field of the laser. The quiver energy, or ponderomotive potential $U_p \propto I\lambda^2$, amounts to typically a few eV for visible to near-IR driving lasers but can be dramatically increased if MIR laser sources are used. While propagating in the laser field, the electron may re-collide with its parent ion [1] leading to high-harmonic generation and electron scattering and diffraction. Both effects can be extended to higher energies by using MIR drivers. Key to generate attosecond pulses from HHG and reach the ultimate time resolution in electron scattering experiments is measurement and control of the CEP.

In the MIR spectral range, established methods for measuring the CEP are faced with significant challenges. Firstly, the overlap of a broadband MIR pulse with its second harmonic may no longer be within the detection range of economic silicon-based detectors, making CEP detection with the f-2f method costly. Secondly, due to the unfavorable scaling of the recollision probability ($\sim \lambda^{-4}$) the stereo-ATI technique cannot be directly transferred to the MIR. In order to identify efficient routes to CEP measurements it is desirable to obtain a survey of strong-field phenomena in phase-controlled MIR laser fields.

[#]matthias.kuebel@uni-jena.de

Here, we report on measurements of above threshold ionization using CEP-controlled few-cycle laser pulses at 3.1 μm . We observe pronounced CEP-dependencies of rescattered electrons for the benchmark system Xe, as well as for C₆₀, which was identified as an anomalous scatterer at near-IR wavelengths [1]. However, as expected, the low rescattering probability precludes usage of these targets in a stereo-ATI phase meter.

The prospects for detecting the CEP via rescattered electrons is more favorable when using Cs as a target, whose low ionization potential allows for experiments using moderate laser intensities. Our experimental results represent reference data for the design of a specialized stereo-ATI phase meter, in which alkali metals are used. Moreover, our measurements provide clear evidence for a new mechanism leading to high-order CEP-dependencies in photoelectron spectra from strong fields.

In addition, we have measured CEP-dependent spectra of HHG in ZnO. Thanks to the large bandwidth of the MIR laser, adjacent odd-order harmonics overlap. The spectral interference fringes that appear in the overlap regions provide access to the CEP, as shown in Figure 1. In a very recent publication [2], we demonstrate that HHG from solids provides an economic route to CEP measurements of MIR few-cycle pulses.

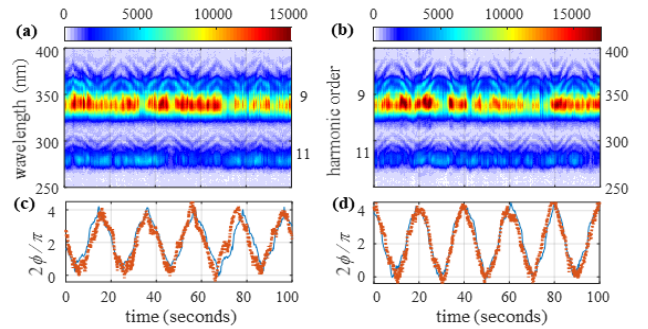


Figure 1 CEP measurement using HHG in ZnO. The series of harmonic spectra (a,b) have the triangular (a,c) and sinusoidal (b,d) waveforms used to vary the CEP, imprinted on them. The retrieved CEP values (blue line) together with reference f-2f measurements (red dots) are shown in panels (c,d).

References

- [1] S. Skruszewicz, *et al.*, in preparation
- [2] R. Hollinger, *et al.*, *Opt. Exp.* **28**, 7314 (2020).

Ultrafast Laser-Induced Fragmentation of Molecular Ion Beam Targets with a High-Repetition-Rate Laser Source

Bo. Ying^{1,2}, P. Wustelt^{1,2}, M. Kübel², A.M. Saylor^{1,2}, T. Stöhlker^{1,2}, and G.G. Paulus^{1,2}

¹Helmholtz Institute Jena, Germany; ²Institute for Optics and Quantum Electronics, Jena, Germany

In this project, we report the first measurement of the strong-field fragmentation of a molecular ion beam target using a 100 kHz-High-Repetition-Rate Fiber Laser Source. The high laser repetition rate allows to overcome the limitations resulting from the low target densities of ionic targets.

Simple molecular and atomic systems play an important role in understanding of principles of light-matter interaction. In contrast to neutral targets, ionic targets provide an easy access to many fundamental systems, which serve as benchmark systems for theory, such as the single electron system He^+ and the simplest molecular ion H_2^+ [1]. Additionally, some molecular species exist only as an ion and must be synthesized in an ion beam apparatus, for example the helium hydride molecule (HeH^+) [2].

Ion sources produce target density at 10^4 - 10^5 ions/cm³, which is several orders of magnitude lower than that of neutral atomic or molecular beams. Thus, the use of ionic targets lowers dramatically the achievable statistics for the investigation of strong field phenomena, which typically have very low cross sections. Therefore, using conventional laser sources with repetition rates of only 1 kHz, very long measurement times of several days are required. These limitations can be overcome by either increasing the target density or using higher repetition-rate lasers. While the target density is limited by the extraction efficiency from the ion source [1], aiming for high-repetition-rate laser sources is a promising path.

Here, we report the first measurements with a newly acquired 100 kHz-fiber laser system. The pulse duration of the laser pulses of the 100 kHz laser system was characterized with a FROG (Frequency Resolved Optical Gating). (see Fig. 1). The compressed laser pulses are then focused into the interaction region of the ion beam coincidence 3D momentum imaging setup, which is regularly operated at the HI Jena. Additionally, a new data acquisition system was installed, which allows for the momentum coincidence detection of laser-induced molecular fragmentation at high event rates. These laser pulses were successfully used for benchmark measurements of laser-induced fragmentation of the H_2^+ molecule. Using a pulse energy of 800 μJ focusing provides focal intensities of approximately 2×10^{14} W/cm², high enough to observe dissociation and ionization of H_2^+ (see Fig. 2). The data was obtained with a measurement time of only approximately 1 hour and demonstrates

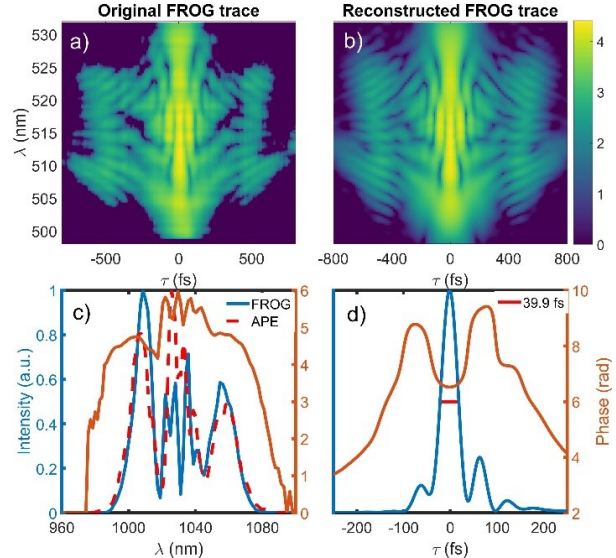


Figure 1: SHG FROG measurement for the 100 kHz laser. (a) Measured FROG trace in log. scale. (b) Reconstructed FROG trace, (c) reconstructed spectrum (solid blue line) with spectral phase (solid orange line) and the measured spectrum (dashed red line). (d) Temporal profile with phase, the FWHM pulse duration is 39.9 fs.

that the high repetition rate laser enables the conduction of ion beam experiments at much higher event rates. The new laser source allows for measurements which are previously too time consuming to be realized. Such candidates include dedicated pump-probe measurements, carrier-envelope-phase dependent measurements or scans with a larger parameter space in general.

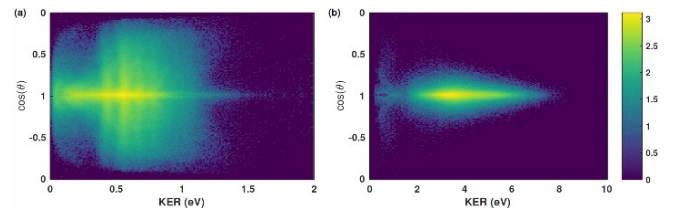


Figure 2: H_2^+ measurement with the 100 kHz laser system: (a) KER and $\cos(\theta)$ dependent distribution after dissociation (a) and ionization (log. scale) ($I \approx 2 \cdot 10^{14}$ W/cm² and 40 fs).

References

- [1] T. Rathje, et al., *Phys. Rev. Lett.* **111**, 093002 (2013).
- [2] P. Wustelt, et al., *Phys. Rev. Lett.* **121**, 073203 (2018)

bo.ying@uni-jena.de

Role of free carriers in the absorption of intense long wavelength light

Richard Hollinger^{1,2,#}, Ellisa Haddad³, Maximilian Zapf⁴, Robert Röder⁴, Ingo Uschmann¹, Michael Zürch¹, Daniil Kartashov¹, François Légaré³, Carsten Ronning⁴, Christian Spielmann^{1,2}

¹Institute of Optics and Quantum Electronics, Abbe Center of Photonics, Friedrich-Schiller-University Jena, Germany;

²Helmholtz Institute Jena, Germany; ³INRS-EMT Varennes, Canada; ⁴Institute for Solid State Physics, Friedrich-Schiller-University Jena, Germany

The nonlinear absorption of light in a broad spectral range ranging from the near- to the far-infrared in the semiconductor ZnO was studied. The onset of stimulated emission (lasing) was applied to probe the density of excited carriers. Comparing the experimentally determined lasing thresholds with theoretical simulations based on a rate equation model provides insight into the nature of the excitation channels. Increasing the wavelength the electron excitation mechanism changes first from multiphoton absorption to tunnelling excitation, and finally electron impact excitation upon intraband free carrier absorption is the dominant mechanism.

In recent years, strong-field laser physics has experienced a shift towards longer wavelengths. On one hand this is motivated by the beneficial scaling law of electron acceleration as a result an increasing ponderomotive energy ($U_p \sim \lambda^2$). On the other hand, the low linear excitation rate of mid-IR light in wide band gap semiconductor and dielectric materials allows for applying high electric fields [1]. However, applying a strong electric laser field onto a semiconductor carries the risk of laser induced damage due to avalanche excitation upon free carrier heating. In this work the contribution of interband impact excitation subsequently intraband free carrier absorption is studied using photoemission spectroscopy from polycrystalline ZnO thin films.

Polycrystalline ZnO thin films are a well-known wide-bandgap (3.3 eV) semiconductor material and one of a few, efficient near ultraviolet (NUV) laser materials [2]. Here we demonstrated NUV lasing far off-resonance pumped in the multiphoton absorption and tunnelling excitation regime by intense femtosecond laser pulses in the spectral range from 1.2 to 10 μm wavelength, whereby the ratio between the band gap and photon energy is up to 27.

The onset of lasing was experimentally confirmed by an abrupt increase of the output yield and a spectral narrowing as a function of the pump laser intensity. This lasing threshold was additionally confirmed by temporally resolved measurement revealing a transition from a slow to a fast dynamics.

Figure 1 depicts the lasing threshold as a function of the

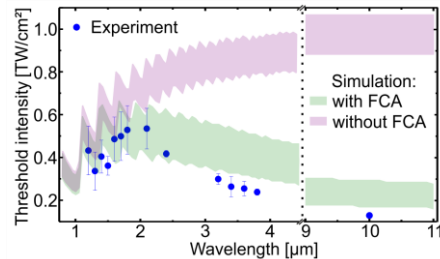


Figure 1: Threshold intensity to observe lasing from ZnO thin films as function of the pump wavelength

pump laser wavelength. The blue dots show the experimentally determined laser threshold values. A rate equation model, based on the the Keldysh and Drude formalism [3] describing the interband and intraband absorption processes, was used to study the nature of the electron excitation channels (green and purple areas). The lasing threshold values for excitation pulses between 1.2 and 2 μm increase as a result of a higher number of photons absorbed in the multiphoton absorption process. The saturation of the threshold values reveals the transition towards the tunneling excitation mechanism [3] which is characterized by a wavelength independent electron generation rate. Comparing calculations with and without free carrier absorption (green and purple areas, respectively) reveals, that the reduction of the pump threshold intensity of pump wavelength in the mid- to the far IR (2-10 μm) can be explained by the increasing electron impact excitation upon efficient free carrier absorption (FCA).

Therefore our results demonstrate the possibility of NUV lasing from polycrystalline ZnO thin films optically pumped in the tunneling regime as well as the striking importance of free carriers in the absorption processes of intense light in the mid- and far-IR.

We acknowledge support by the DFG through IRTG 2101 and the Federal Ministry of Education and Research (BMBF) under “Make our Planet Great Again—German Research Initiative”

- [1] S. Y. Kruchinin, et al., Rev. Mod. Phys. 90(2), 21002 (2018).
- [2] C. Klingshirn et al., Phys. Rev. B 75, 115203 (2007).
- [3] R. Hollinger et al., Nano. Lett. B 19, 3563 (2019).

[#] richard.hollinger@uni-jena.de

Improving the contrast of ghost image based on the speckles' histogram

Zhe Sun^{1,2,3,#}, Frederik Tuitje^{1,2}, and Christian Spielmann^{1,2}

¹Helmholtz Institute Jena, Germany; ²Institute of Optics and Quantum Electronics, Friedrich Schiller University; ³Xi'an Institute of Optics and Precision Mechanics, Chinese Academy of Sciences

In this report, the influence of the histogram of speckle field on the contrast-to-noise ratio (CNR) is examined in microscopic pseudothermal ghost imaging which is a promising method for high-quality XUV/X-ray imaging. The result shows that the histogram of speckle field plays a significant role in CNR improvement. To our knowledge, the scaling of CNR with the different histograms of the speckle field is observed for the first time in the field of microscopic ghost imaging.

In recent years, ghost imaging with pseudothermal light sources has been studied extensively to overcome the limitations of the image quality, which mainly depends on the detection contrast-to-noise ratio (CNR). In microscopic pseudothermal ghost imaging, the diffused light is weak and easy to be disturbed by the stray light in detection. Thus, the influence of the histogram of speckle field must be considered, which represents the distribution of the pixel count of the speckle pattern. In this report, we report on the influence of the speckle's histogram on the CNR in microscopic ghost imaging. We analyze the influence of the center position and full width at half maximum (FWHM) of the speckles' histogram to eliminate the unfavorable influence caused by the pseudothermal light field in experiment. This research has great support for nanoscale microscopic imaging combining our previous results in manipulating the speckle pattern and speckle size, especially for high-quality XUV/X-ray imaging [1-4].

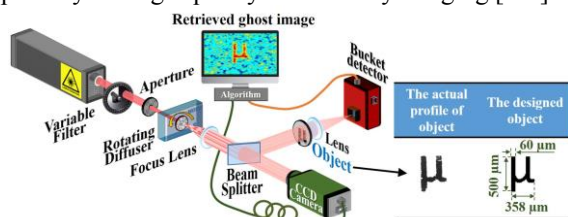


Fig.1 Schematic of the experimental setup and object.

The experimental setup to study the evolution of CNR with pixel distribution in the speckle field is shown in Fig. 1. A He-Ne laser and a rotating diffuser constituted a nonuniform pseudo-thermal light source. Using a continuously variable filter and a few filter papers, we can realize the different Gaussian-like speckle's histograms. We can see from Fig. 2(a), the mean CNR of the object "μ" will increase rapidly with increasing the FWHM of the speckles' histogram. By contrast, after being modulated by corresponding optical elements, the FWHM of the speckles' histogram became narrower. In Fig. 2(b), the CNR of the re-

trieved images with different center positions of the speckles' histogram was evaluated. By moving the center position of the speckles' histogram, the CNR starts to grow from the left position of the speckles' histogram until it reaches a maximum, then the CNR begins to drop.

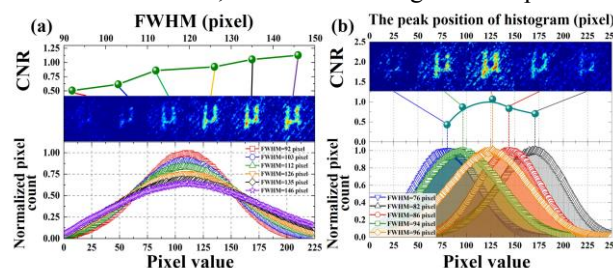


Fig. 2 (a) The CNR as a function of the FWHM of the speckles' histogram, and corresponding the retrieved images; (b) The CNR as a function of different center positions of the speckles' histogram, and corresponding the retrieved images.

Therefore, the best CNR of ghost image can be achieved if the speckles' histogram with the broadest FWHM located in the center position of the histogram. The slight discrepancy may be due to some uncertainties of the FWHM of the speckles' histogram. Our data prove that the widest FWHM at the center position of the speckle's histogram can achieve the best CNR for the given speckle size and object in microscopic ghost imaging.

In conclusion, the speckle's histogram plays a more important role in the CNR enhancement of ghost imaging. To our knowledge, this CNR behavior with the speckles' histogram is observed for the first time in microscopic ghost imaging. Furthermore, it offers a general approach applicable to all fields of imaging where higher CNR is needed and can be applied to all lensless ghost imaging schemes of any wavelength, including XUV/X-ray sources.

Work supported by DFG under Germany's Excellence Strategy – EXC 2051 – Project-ID 390713860; GSI & Postdoc Research Found. China (GSI05HGF-GSI-OCPC-2017).

References

- [1] Z. Sun, F. Tuitje, and C. Spielmann, *Opt. Express* **27**(23), 33652 (2019).
- [2] T. Helk, M. Zürich, and C. Spielmann, *Struct. Dyn.* **6**(1), 010902 (2019).
- [3] Z. Sun, F. Tuitje, and C. Spielmann, *Annual Report of the Helmholtz-Institute Jena*, **57** (2018).
- [4] F. Tuitje, Z. Sun, and C. Spielmann, *Annual Report of the Helmholtz-Institute Jena*, **58** (2018).

zh.sun@gsi.de; zhe.sun@uni-jena.de

Storage of Highly Charged Ions for Non-Linear Laser Experiments at the HILITE Penning Trap

M. Kiffer^{*1}, S. Ringleb^{1,2}, N. Stallkamp^{1,3}, B. Arndt⁵, S. Kumar⁴, G. G. Paulus^{1,2}, W. Quint^{3,6}, B. Reich⁶, Th. Stöhlker^{1,2,3}, and M. Vogel³

¹Friedrich-Schiller-Universität, Jena; ²Helmholtz Institute Jena; ³GSI, Darmstadt; ⁴Inter-University Accelerator Centre, New Delhi; ⁵Goethe-Universität, Frankfurt; ⁶Ruprecht Karls-Universität, Heidelberg

The goal of the HILITE Penning trap setup is to provide a well-defined ion target that can be used to study light-matter-interactions with intense laser beams. We present the current status of the setup and the preparations for a beam time at the FLASH laser facility at DESY in Hamburg.

The development of high-intensity laser systems in the XUV to X-ray regime allows the investigation of non-linear ionisation of highly charged ions. Especially, the K-shell of highly charged ions is available for ionisation, such that simple systems like hydrogen-like ions can be investigated. To compare the measured absolute cross sections of the interaction, the ion target has to be well defined and the ion detection techniques have to be sensitive also to small numbers of ions.

The HILITE experiment [1] produces the target ions with a compact electron-beam ion trap (EBIT), which allows the creation of ions up to Xe^{46+} . The produced ion bunch is guided and decelerated inside a beam line with a length of about 2 m and stored in a Penning trap. Such a trap can confine ions and offers a wide range of ion manipulation techniques as well as destructive and non-destructive detection. The main ion detector of the setup is a multi channel plate detector (MCP). In particular, this detector allows the measurement of single ions.

The motivation for the beam time at the FLASH laser facility is to investigate double photon ionisation. To this end we created C^{2+} bunches and trapped them for an extended period. Figure 1 shows the trap content after a storage time of 14 min.

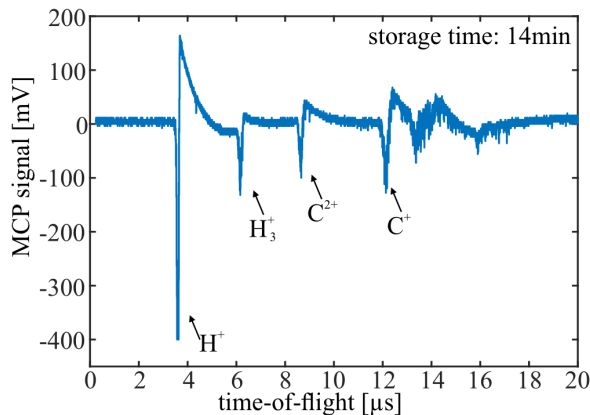


Figure 1: Time-of-flight spectrum of the stored C^{2+} ions after 14 min. Measured with the MCP.

* markus.kiffer@uni-jena.de

This plot shows that a sufficient number of ions can be stored and are available for the experiment while distinct charge states can be determined. Furthermore, the narrow C^{2+} peak indicates a cold ensemble, which is required for sufficient target densities. Here the main cooling mechanism is buffer gas cooling. In the future we plan to reduce the required cooling time with resistive cooling.

In addition to the C^{2+} , one can see other peaks, which result from charge exchange with the residual gas, mainly H_2 . From the decay time of the ion signal we deduce the residual gas pressure in the trap centre to be about 2×10^{-10} mbar, which allows storage of highly charged ions for sufficient times to conduct laser experiments.

The setup is modular and transportable to allow operation of the setup at different laser facilities. For a first laser experiment we have successfully moved the setup to the FLASH laser facility at DESY in Hamburg. Figure 2 shows the assembled setup.



Figure 2: Picture of the full setup at the FLASH laser facility. The laser enters the setup from the pipe to the left. The target chamber is encompassed by our 6 T magnet. To the right of the chamber one can see the ion beam line.

During the beam time we want to investigate double photon ionisation of C^{5+} and O^{5+} and show that the setup is capable of providing a well-defined ion target for laser experiments. In the future we plan to conduct more experiments with XUV laser systems to investigate ion-laser interactions in detail.

References

- [1] S. Ringleb et al. Journal of Physics Conference Series 635 (2015) 092124
- [2] M. Kiffer et al. Review of Scientific Instruments 90.11 (2019): 113301.

X-ray and particle emission from titanium foils irradiated by ultra-relativistic near-infrared ultrashort laser pulses

E. Eftekhari Zadeh^{1,2}, R. Löttsch^{1,2}, L. Manganelli^{3,4}, S. Blümke¹, D. Kartashov¹, I. Uschmann^{1,2}, O. Rosmej³, C. Spielmann^{1,2,#}

¹ Institute for Optics and Quantum Electronics, FSU Jena, Germany; ² Helmholtz Institute Jena, Germany; ³ GSI Darmstadt, Germany; ⁴ Wolfgang Goethe University Frankfurt, Germany

Recent experiments on relativistic interaction of ultrashort laser pulses with nanowire targets demonstrated a possibility to reach unique plasma parameters with high density and temperatures of electrons. It was predicted in simulations that wire geometry enables unprecedented current densities resulting in pinch effect that increases the electron density and temperature by orders of magnitude. To reach pinching regime the temperature of electrons is of critical importance. Typically to ensure sufficiently high temporal contrast of relativistically intense laser pulses frequency doubling technique is used. However, electron temperature scales quadratically with the laser wavelength, thus longer wavelength laser pulses are preferable for entering pinching regime.

In this report we present results in experimental investigation of energy spectra of electrons, ions and X-ray radiation generated from Ti foils by relativistically intense, femtosecond near-IR laser pulses to verify if the temporal contrast of the laser system is sufficient for relativistic interactions with nanowire targets.

Experiments were conducted at the JETI40 multi-terawatt laser system delivering 30 fs laser pulses at the 0.8 μm wavelength with energy up to 520 mJ and estimated peak intensity on the target $\sim 5 \cdot 10^{19}$ W/cm², resulting in normalized vector potential value $a_0 \approx 5$. Particle and X-ray energy spectra were measured for two different focusing conditions: normal to the target and under 45° (p-polarized) incidence angle on the target surface using 90° and 45° off-axis parabolic mirrors correspondingly. The targets were 15 μm and 50 μm thick Ti foils placed in a vacuum chamber pumped down to 10^{-4} mbar.

The energy distribution of run-away electrons with energies above 300 keV was measured by a magnet spectrometer with a magnetic flux density of 250 mT and image plates (IP) as a detector accumulating a signal over 10–30 laser shots. The X-ray crystal spectrometer comprises a toroidally bent GaAs crystal in 111 orientation. Spectral diagnostic was conducted in air after the emission was passing through a 50 μm thick Kapton window.

The measured electron spectra from front and back sides of the target for different focusing conditions are shown in Fig. 1. The bulk electron temperature is similar for both focusing conditions and estimated to about 0.3 MeV. At the same time, the hot electron fraction shows about twice higher temperature for the back side of the target (~ 2.7 MeV) in comparison to the front side under normal focusing (~ 1.3 MeV), whereas for 45° incidence the hot temperatures are very similar (~ 0.9 MeV) and substantially less than for the normal focusing

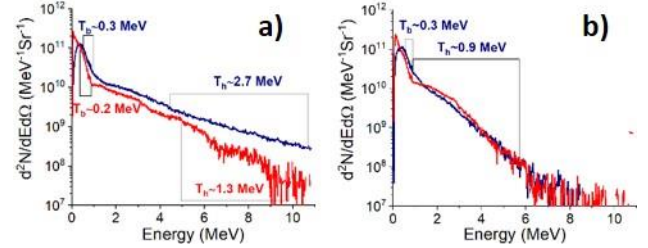


Fig. 1: Energy spectra of electrons measured at the front side (red line) and the back side (blue line) of the foil for a) normal incidence and b) 45° incidence focusing. At the back side the spectra are measured in the direction of the laser beam propagation, whereas at the front side the spectra are measured under 10° for a) and 30° for b).

geometry. Importantly, our measurements show that the temperature of electrons at the back side of the foil is high enough to penetrate through a few hundred micron thick Si substrate that supports nanowire targets. Therefore, it might be possible to detect pinch effect in wires from measurements of energy spectra and density angular divergence of electrons.

Measured X-ray spectra (see Fig. 2) show that line emission from high charge states like He-like Ti ions are much more intense for the case of normal incidence than for 45° geometry but still much weaker than in our previous experiments with relativistically intense second harmonic beam. These high charge states can be reached only under conditions of relatively hot and dense plasmas. Therefore, our results suggest that, although the temporal contrast of laser pulses at the fundamental wavelength is considerably worse than after frequency doubling, it should be possible to use those pulses under condition of normal incidence for relativistic interaction with sparsely arranged nanowire targets.

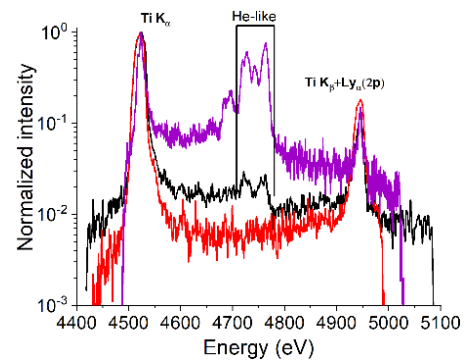


Fig. 2: Calibrated spectra of X-ray emission measured under 45° focusing (red solid line), normal focusing (black line) and 45° focusing but using the second harmonic pulses with $a_0=1.4$.

Extreme ultraviolet interferometry for artefact-free coherence tomography driven by a high-harmonic source *

J. Nathanael^{†1,2}, S. Fuchs^{1,2}, M. Wünsche^{1,2}, J. J. Abel², J. Reinhard^{1,2}, F. Wiesner^{1,2}, C. Rödel¹, and G. G Paulus^{1,2}

¹Helmholtz Institute Jena, Germany; ²Institute of Optics and Quantum Electronics, Friedrich-Schiller University Jena, Germany

Extreme ultraviolet coherence tomography (XCT) is emerging as a laboratory-scale sub-surface metrology method, which can achieve a depth resolution of 16 nm using the spectral range of 36 – 98 eV [1]. Broadband extreme ultraviolet radiation (XUV) that is generated by a high-harmonic source is focused onto the sample under investigation. The reflected spectral intensity is detected with a high-resolution XUV spectrometer [2]. With the ability to mitigate autocorrelation artefacts using a phase-retrieval algorithm, the reconstruction of samples with an arbitrary depth structure is possible. However, this algorithmic solution usually requires an adequate signal-to-noise ratio. Here, we report on a solely hardware-based approach of artefact mitigation using a broadband extreme ultraviolet interferometer, which enables direct unambiguous three-dimensional imaging. Our approach utilizes a few nanometer thin Si_3N_4 membrane that is suspended in close proximity of the sample surface such that a common-path interferometer is realized. The distance of the membrane to the surface is critical. Its maximum distance from the surface depends on the depth structure of the sample and the resolving power of the spectrometer. Accordingly, a high-resolution spectrometer is necessary since large depths correspond to high frequency modulations in the spectral intensity. The thickness of the membrane is about 20 nm. Its mechanical positioning with respect to the sample surface is accomplished by a sophisticated mount that allows nanometer precision manipulation in tip, tilt, and distance while keeping vibrations at low amplitudes (≈ 10 nm). The distance is kept constant at typically 1000 nm with a closed-loop piezo-actuator system. The three-dimensional representation in Fig.1 is accomplished by scanning the sample under the incident XUV beam and retrieving the individual depth structures. A volumetric image is created from these datasets. The silicon sample contains three layers. At a depth of 170 nm, there is a few nanometer thin SiO_2 layer, at 220 nm a 10 nm gold layer which is laterally structured, and at 330 nm a final layer of 10 nm thick scattered points of gold. The image shows an edge of the buried gold layer at the depth of 220 nm.

This hardware-based approach of artefact-free XCT by realizing a the common-path interferometer enables sub-

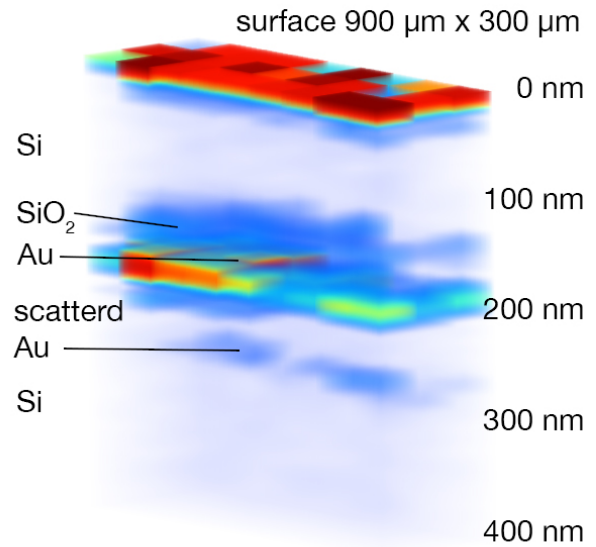


Figure 1: Three-dimensional representation of the scan over a laterally structured sample with buried layers. The scan area is $300\mu\text{m}$ by $900\mu\text{m}$ in 27 individual points. An edge of the structured layer is prominently visible at about 220 nm depth.

surface non-invasive 3D cross-sectional imaging of layered samples on the laboratory scale. Our XUV interferometer can furthermore be utilized to determine the broadband resolution of the XUV spectrometer[2]. Since the membrane is independent of the sample, it is possible to utilize the reflection of the membrane as a spectral reference of the XUV source.

References

- [1] J. Nathanael, M. Wünsche, S. Fuchs, T. Weber, J.J. Abel, J. Reinhard, F. Wiesner, U. Hübner, S.J. Skruszewicz, G.G. Paulus and C. Rödel. “Laboratory setup for extreme ultraviolet coherence tomography driven by a high-harmonic source”, *Review of Scientific Instruments*, **90** (11), p.113702, 2019.
- [2] M. Wünsche, S. Fuchs, T. Weber, J. Nathanael, J.J. Abel, J. Reinhard, F. Wiesner, U. Hübner, S.J. Skruszewicz, G.G. Paulus and C. Rödel. “A high resolution extreme ultraviolet spectrometer system optimized for harmonic spectroscopy and XUV beam analysis”, *Review of Scientific Instruments*, **90** (2), p.023108, 2019.

* Work supported by HI Jena/University Jena; Bundesministerium für Bildung und Forschung (BMBF) (VIP “X-CoherenT”); Thüringer Aufbaubank Forschergruppe Grant No. 2015FGR0094 and 2018FGR0080; We thank Uwe Hübner from the Leibniz Institute of Photonic Technology (IPHT) Jena for the production of the sample.

[†] jan.nathanael@uni-jena.de

High Density Ion Beam Targets for Ultrafast Laser-Induced Processes using High Brightness Ion Sources

F. Machalett^{1,2#}, P. Wustelt^{1,2}, V. Huth², T. Weber², T. Stöhlker^{1,2}, and G.G. Paulus^{1,2}

¹Helmholtz Institute Jena, Germany; ²Institute for Optics and Quantum Electronics, Friedrich-Schiller-University Jena, Germany

In this work we report on first simulations and experiments with high brightness liquid metal ion sources (LMIS) to generate high density ionic laser targets. As a first source, the emission characteristics of a Ga-LMIS has been measured and optimized. The LMIS will be prepared for adaption to the existing beam line for ultrafast laser-induced processes at the HI Jena. These experiments should open the opportunity to use atomic or molecular ions of many elements as high density ionic targets for laser interactions.

The aim of this work is to generate advanced ion beam targets for the study of ultrafast laser-induced fragmentation and ionization dynamics of atoms and molecules in strong laser fields. Ionic targets allow the investigation of many interesting fundamental systems of light-matter interaction, as He^+ and H_2^+ [1], and molecules that only arise in the ion source, e.g. HeH^+ [2]. An additional advantage is the well-defined setting and controllable properties of an ion beam target in the interaction volume with the laser beam. Drawbacks of ion beam targets generated by conventional ion sources like duoplasmatron, EBIT and RF, are the very low densities of $10^4 - 10^5 \text{ cm}^{-3}$ in the laser focus, resulting from the typical parameters of the ion beam with a cross section $A = 0.25 \text{ mm}^2$ and a current of $I = 2 \text{ nA}$. The very low number of molecules in the laser focus requires very long measurement times. To overcome these problems, an alternative ion source with a higher brightness is desirable. The aim is to generate particle densities closer to those of neutral targets, which are typically around 10^{11} cm^{-3} for cold supersonic gas jets.

A promising respective candidate is a high brightness liquid metal ion source (LMIS) based on the field evaporation from a liquid metal cone of 10 to 30 nm. At least two orders of magnitude higher densities should be possible.

The LMIS has the following advantages [3,4]:

- Small source size results in high brightness of $10^6 \text{ A / cm}^{-2} \text{ sr}^{-1}$ (see Fig.1)
- Simple and compact setup (see Fig.2)
- Ions from a variety of chemical elements possible (almost half the periodic table) by the use of liquid alloys
- Numerous combinations of different stoichiometries in the molecular ions of an element (Si_2^+ , Ge_2^+)
- Examination of noble metal molecular ions Au_n^{m+} (e.g. Au_2^+ , Au_3^+ , Au_3^{2+}) and noble metal compounds (e.g. AuSi^+ , AuGe^+)

- Possibilities of further increasing emission currents by application of new emitter configurations and source geometries based on high current LMISs developed for ion thrusters.

First experiments with a Ga-LMIS were carried out and have shown promising results. Emission currents of $60 \mu\text{A}$ have been measured and will be improved in the next steps. Experiments using other elements and alloys, e.g. Au-Si and Au-Ge, are in preparation.

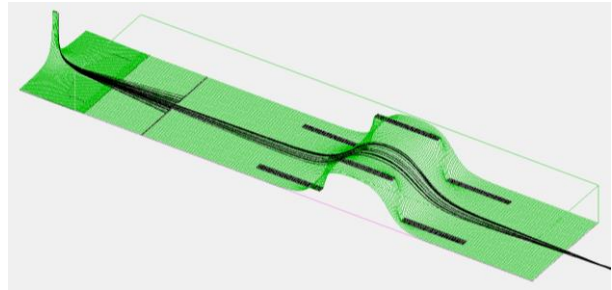


Fig. 1 Potentials at the emitter tip and the resulting trajectories of the ions emitted from the Taylor cone and focused by the einzel lens (simulated in SIMION)

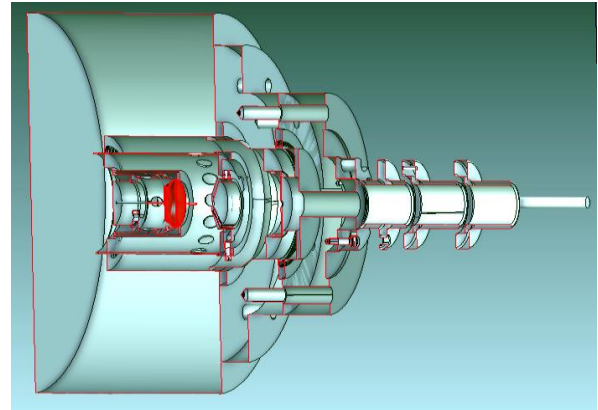


Fig. 2 Scheme of the ion source housing with LMIS ion emitter (red) and an einzel lens.

References

- [1] T. Rathje, et al., *Phys. Rev. Lett.* **111**, 093002 (2013)
- [2] P. Wustelt, et al., *Phys. Rev. Lett.* **121**, 073203 (2018)
- [3] F. Machalett, P. Seidel, *Focused Ion Beams and Some Selected Applications*, EAP, Wiley 2019
- [4] L. Bischoff, et al., (2016). *Appl. Phys. Rev.* **3**: 021101 (30 pp).

frank.machalett@uni-jena.de

Setup for a study on the polarization transfer in elastic scattering of hard x-rays

W. Middents^{1,2,#}, G. Weber^{1,3}, M. Vockert^{1,2}, U. Spillmann³, A. Volotka¹, and Th. Stöhlker^{1,2,3}

¹Helmholtz Institute Jena, Germany; ²Institute for Optics and Quantum Electronics, Friedrich Schiller University Jena; ³GSI, Darmstadt, Germany

We report on the development of a setup for a study of the polarization transfer in elastic scattering of hard x-rays, which was recently granted beamtime at the PETRAIII synchrotron of DESY. The planned experiment on the polarization properties of elastically scattered synchrotron radiation will allow us to get a complete characterization of the polarization-dependent elastic scattering.

Elastic scattering of hard x-rays on atoms is a fundamental process in QED which can be used to test the theoretical models. Fully relativistic calculations predict a strong dependence of the polarization of the scattered beam on the degree of polarization of the incident beam [1]. In a previous measurement, where the linear polarization of the scattered radiation was analyzed within the polarization plane of the incident synchrotron beam, we could verify this prediction [2].

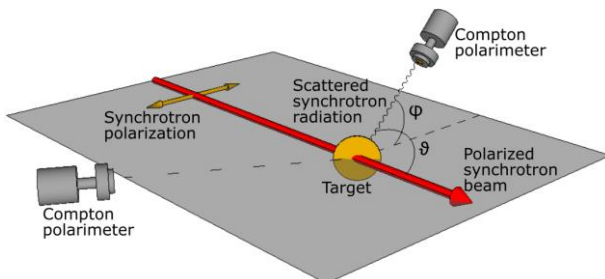


Figure 1: Sketch of the experimental setup with two Compton polarimeters for linear polarization analysis of the elastically scattered radiation.

In addition to the incident photon beam's degree of polarization and the scattering angle ϑ , the scattered beam's polarization degree and orientation also strongly depend on the azimuthal scattering angle φ , which denotes the angle between the incident polarization plane and the scattering plane, see Fig. 1. In an upcoming experiment an out-of-plane detector will enable us to probe this dependence for the first time, providing a more complete picture of the scattering process. We plan to use synchrotron radiation with a beam energy of 175 keV as a highly linear polarized x-ray source at the beamline P07 of the PETRAIII facility and a thin gold foil ($Z=79$) as the scattering target.

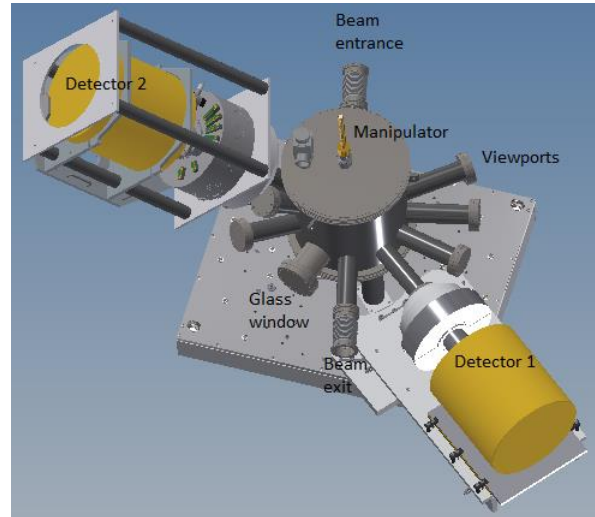


Figure 2: Technical design of the experimental setup with two Compton polarimeters for linear polarization analysis of the elastically scattered radiation.

The design of the experimental chamber is shown in Fig. 2. We will use two 2D-sensitive hard x-ray detectors as Compton polarimeters [3] to measure the degree and direction of linear polarization of the scattered radiation. The first detector will be placed inside the polarization plane of the incident photon beam ($\varphi=0^\circ$), which will allow us to precisely measure the degree of linear polarization of the incident beam, as shown in [2]. The second detector will be placed at different azimuthal angles outside the polarization plane ($\varphi>0^\circ$) to probe the dependence on the azimuthal scattering angle. Both detectors will be placed at multiple scattering angles ϑ during the experiment for a complete picture of the scattering process. To avoid scattering in the air, we will place the target inside a vacuum chamber. The chamber and positioning system for the detector are being designed and constructed at the moment.

References

- [1] A. Surzhykov *et al.*, J. Phys. B: At. Mol. Opt. Phys. **48**, 144015 (2015)
- [2] K.-H. Blumenhagen *et al.*, New J. Phys. **18**, 103034 (2016)
- [3] G. Weber *et al.*, J. Phys.: Conf. Ser. **583**, 012041 (2015)

wilko.middents@uni-jena.de

Detector support frames for the 1s Lamb shift study at CRYRING@ESR

P. Pfäfflein^{*1,3}, M. O. Herdrich^{1,3}, T. Köhler³, G. Weber¹, and Th. Stöhlker^{1,2,3}

¹Helmholtz Institute Jena, Germany; ²GSI, Darmstadt, Germany; ³Friedrich Schiller University Jena, Germany

The upcoming investigation of the 1s Lamb shift in hydrogen-like uranium performed at CRYRING@ESR will use two high resolution cryogenic micro-calorimeters for X-ray spectroscopy. They outperform conventional intrinsic germanium (Ge(i)) detectors by an order of magnitude in terms of resolution. Ge(i) detectors on the other hand offer online spectra throughout the measurement at the electron cooler where both detectors need to be mounted level with the stored ion beam, 2 metres off the ground [1]. This report focuses on the design of two support frames for the detector setup.



Figure 1: Left: Detector assembly used at the 180° port with Blufors cryostat. Right: Detector assembly for use at the 0° port using a compact MiniMix cryostat. Bright orange: accompanying Ge(i) detectors.

Spectroscopy of the light emitted by electronic transitions is a well established method for gaining insight into the atomic energy levels. In the case of highly charged ions these photons can have energies in the order of 100 keV and therefore X-ray detectors are necessary. In that energy regime micro-calorimeters can outperform the resolution of conventional Ge(i) detectors by more than one order of magnitude [2]. Therefore the upcoming investigation of the 1s Lamb shift in hydrogen-like uranium (G-PAC E138) will make use of them. One major drawback of micro-calorimeters is their need for temperatures lower than 50 mK, which means that they require helium dilu-



Figure 2: Stepper-motor-driven XYZ positioning unit for use with Blufors cryostat.

tion cryostats which are usually a lot bigger than the liquid nitrogen dewars required for the operation of Ge(i) detectors. This experiment will be the first investigation of the X-ray emission for H-like uranium at CRYRING, exploring the unique geometrical conditions at the electron cooler (simultaneous x-ray detection at 0° and 180°). For monitoring purposes it will be necessary to quickly switch between Ge(i) detectors and their capability to provide online spectra and the micro-calorimeters which offer superior resolution but require extensive data post processing.

The shape of the designed frames, displayed in figure (1) is determined by geometric constraints of the vacuum setup of CRYRING as well as site-specific restrictions (e.g. emergency exits). The common idea was having an upper mount carrying both detectors and a lower frame adapting them to the beam height and granting the necessary support by being bolted to the cave floor. The feet of said lower frame can be used to fine-adjust the reference height and level the supports. In the case of the simpler support in the right part of the image the alignment of both detectors with respect to each other is realised by the table carrying the Ge(i) detector. For the support of the larger cryostat as seen on the left of figure (1) the Ge(i) detector is aligned with the bottom frame and the micro-calorimeter can be positioned by an automated XYZ stage shown in figure (2). Both supports are currently being built and will be installed at GSI within 2020.

We acknowledge financial support by the European Union and the federal state of Thuringia via Thüringer Aufbaubank within the ESF project (2015 FGR 0094) as well as by BMBF for APPA R&D, project number 05P19SJFAA.

References

- [1] M. Lestinsky, Y. Litvinov and Th. Stöhlker, Physics book: CRYRING@ESR (2016).
- [2] A. Fleischmann et al., maXs Cryogenic Micro-Calorimeter Arrays TDR (2014).

*p.pfaefflein@gsi.de

Energy resolution of maXs, a metallic magnetic micro-calorimeter

P. Pfäfflein^{*1,3}, M. O. Herdrich^{1,3}, J. Geist⁴, D. Hengstler⁴, A. Fleischmann⁴, G. Weber¹, C. Enss⁴,
and Th. Stöhlker^{1,2,3}

¹Helmholtz Institute Jena, Germany; ²GSI, Darmstadt, Germany; ³Friedrich Schiller University Jena, Germany;

⁴Ruprecht Karls University Heidelberg, Germany

For high precision spectroscopy like in the upcoming 1s Lamb shift study of hydrogen-like uranium it is crucial to thoroughly characterise the used detector. For the evaluation of said properties, data taken with a maXs-30 detector in combination with a radioactive ²⁴¹Am source has been analysed. The resolution was determined to be about $\Delta E/E = 2000$ at 26.345 keV.

Micro-calorimeters are pixelated spectroscopic detectors which translate the energy of an incident photon into a temperature rise of a small absorber which is then measured [1]. The detectors work at temperatures below 50 mK, where the relevant material properties like magnetisation, heat capacity and thermal conductivity are very sensitive to changes in absolute temperature. In the case of the maXs, a metallic magnetic micro-calorimeter, each pair of pixels is read out by an individual superconducting quantum interference device (SQUID) which has its own working point and therefore gain. In addition the working point cannot be fixed between operations. Consequently, to determine the detector gain monitoring of the chip's temperature as well as continuous measurement of a known calibration source is necessary. Then it is possible to account for the temperature dependent gain in post processing, where each recorded pulse shape is analysed, resulting in high resolution spectra. Resolutions as good as 1.6 eV at a 6 keV line have been demonstrated [2].

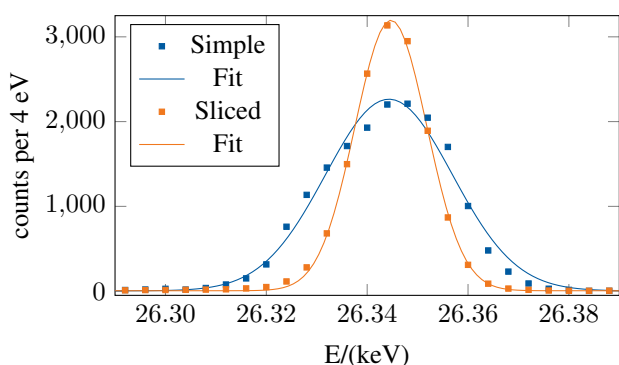


Figure 1: Blue: Result of the first analysis with a Gaussian fit, yielding FWHM to be 29.6 eV. Orange: Result where the data set was divided into two subsets, according to the difference in signal gain as a function of detector base temperature resulting in a 16.8 eV FWHM.

A maXs-30 micro-calorimeter has been used to measure a radioactive ²⁴¹Am source over a period of 10 days. The result of a first analysis can be found as blue plot in figure 1.

*p.pfaefflein@gsi.de

The achieved resolution was considerably inferior than expected and a more in-depth analysis of the data was performed, focusing on the time evolution of the temperature dependence of the gain. This can be seen nicely in figure 2, where the measured energy is plotted against the so-called offset, a signal proportional to the temperature of the detector. Clearly the temperature dependent gain can be seen which needs to be taken into account when compiling a spectrum. This analysis revealed that the operation point of the detector must have shifted throughout the measurement, as data taken in the first 6 d 18 h, plotted as blue dots, nicely scatter around one line and data taken in the remaining 3 d 6 h of the experiment lie around another line. Calibrating each part separately and adding the spectra up lead to an improvement in resolution from 29.6 eV FWHM to 16.8 eV FWHM when fitted with a Gaussian as seen as orange data in figure 1. Although the resolution achieved by the first analysis outperforms an intrinsic germanium (Ge(i)) detector's resolution of 180 eV drastically, this study shows that for achieving the full resolution a micro-calorimeter is capable of, constant measurement of a known calibration source is crucial.

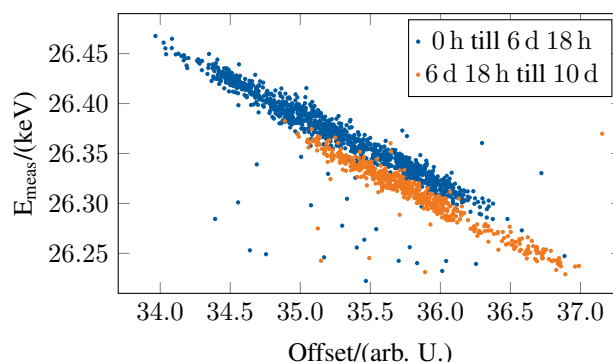


Figure 2: Measured Energy plotted over so-called offset, a detector quantity proportional to the chip temperature. Colour-coded is the time slice of the measured pulse. It is clearly visible that the two time slices need individual calibration.

We acknowledge financial support by the European Union and the federal state of Thuringia via Thüringer Aufbaubank within the ESF project (2015 FGR 0094) as well as by BMBF for APPA R&D, project number 05P19SJFAA.

References

- [1] D. Hengstler et al., Phys. Scr., 014054 (2015).
- [2] C. Pies et al., J. Low Temp. Phys., 167:269-279 (2012).

Commissioning of a SiPM-based ion detector for CRYRING@ESR

G. Weber^{1,*}, A. Borovik Jr.², V. Hilbert^{1,3}, H. Lin⁴, P. Pfäfflein^{1,5}, B. Zhu^{1,3}, C. Hahn^{1,3}, M. Lestinsky⁴, S. Schippers², J. Rothhardt^{1,3}, and Th. Stöhlker^{1,3,4}

¹HI Jena, Germany; ²Justus Liebig University Gießen, Germany; ³Friedrich Schiller University Jena, Germany; ⁴GSI, Darmstadt, Germany;

Combining novel laser-driven high-flux XUV sources with storage rings will open new possibilities for precision spectroscopy as well as pump-probe measurements of highly-charged ions [1]. A proof-of-principle experiment at the CRYRING@ESR was conducted in November 2019, using stored C^+ ions with ion beam energies ranging from 50 keV/u to 600 keV/u. In the experimental section YR09 the ion beam was merged with pulses from a laser-driven high-harmonics XUV source, which was designed to meet the very high vacuum requirements of storage rings.

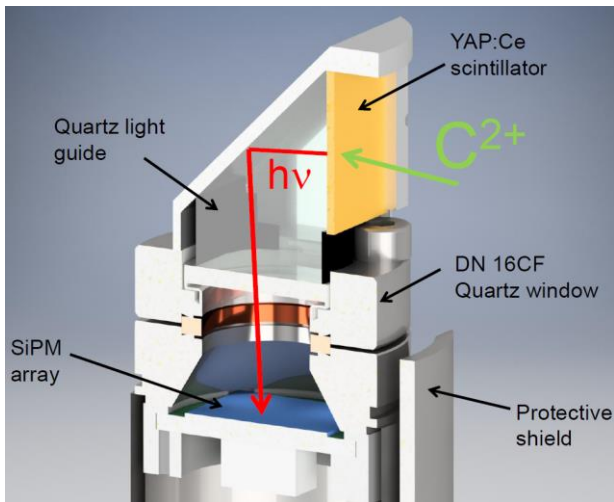


Figure 1: Drawing of the head of the new SiPM-based ion detector.

Ions that underwent charge-changing events were separated from the primary ions by a dipole magnet located downstream to the straight section YR09. The trajectory of the typical product ion, namely C^{2+} , restricts the detection to positions inside the dipole-magnet chamber. This requires the detector to be positioned and operated in a strong magnetic field, which can adversely affect conventional photomultipliers and secondary electron detectors.

Thus, a novel detector system has been developed and installed that is based on a YAP:Ce (yttrium aluminium perovskite, $YAlO_3:Ce$) scintillator connected to an array of silicon photomultipliers (SiPM), which is not sensitive to magnetic fields. Note that the scintillator material is known to be both radiation hard and compatible with strict UHV requirements [2]. A drawing of the detector head, consisting of the scintillator, a light guide and the photodetector is shown in Fig. 1. In the following we report on first results regarding the performance of the detector.

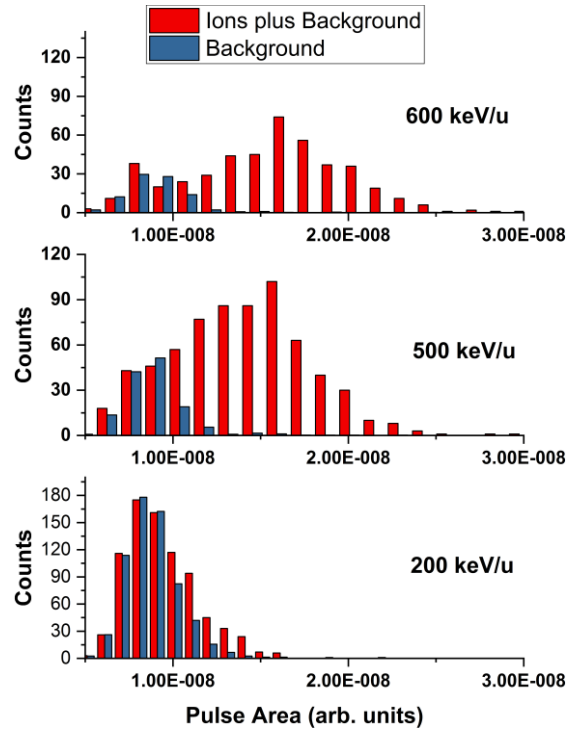


Figure 2: Pulse strength distribution of detector events for three different ion beam energies.

The distribution of pulse strengths, defined by the area under the detector signal, is depicted in Fig. 2 for three different ion beam energies together with the background signals, when no ions were in the ring. It is found that only for 500 keV/u and higher beam energies the signal induced by ion impact on the scintillator is strong enough to be distinguished from the background. This limits the efficiency of the detector for low beam energies and light ions. However, we see considerable potential for improvement by optimizing the guiding of photons from the scintillator to the photodetector and by using a photodetector with a higher quantum efficiency at the specific wavelength of YAP:Ce. Moreover, the shielding of the detector against stray light will be improved in the future.

We acknowledge financial support by BMBF for APPA R&D, project number 05P19SJFAA.

References

- [1] J. Rothhardt et al., *X-Ray Spectrometry* **49**, 165 (2019)
- [2] G. Miersch et al., *NIM A* **369**, 277 (1996)

* g.weber@gsi.de

First measurements of a new type of Coreless Cryogenic Current Comparators (4C) for non-destructive intensity diagnostics of charged particles*

V. Tympel^{1,‡}, Th. Stoehlker^{1,4,8}, J. Tan², H. De Gersem³, N. Marsic³, W. Müller³, D. Haider⁴, M. Schwickert⁴, T. Sieber⁴, J. Golm⁵, M. Stapelfeld⁵, F. Schmidl⁵, P. Seidel⁵, M. Schmelz⁶, R. Stolz⁶, T. Schönau⁶, S. Anders⁶, J. Kunert⁶, V. Zakosarenk⁷

¹Helmholtz Institute Jena, 07743 Jena, Germany; ²CERN, 1211, Geneva 23, Switzerland; ³Department of Electrical Engineering and Information Technology, TU Darmstadt, 64283 Darmstadt, Germany; ⁴GSI Helmholtzzentrum für Schwerionenforschung, 64291 Darmstadt, Germany; ⁵Institute of Solid State Physics, 07743 Jena, Germany; ⁶Leibniz Institute of Photonic Technology, 07745 Jena, Germany; ⁷Supracon AG, 07751 Jena, Germany; ⁸Institute for Optics and Quantum Electronics, 07743 Jena, Germany;

The non-destructive and highly sensitive measurement of a charged particle beam is of utmost importance for modern particle accelerator facilities. A Cryogenic Current Comparator (CCC) can be used to measure beam currents in the nA-range. Therein, charged particles passing through a superconducting toroid induce screening currents at the surface of the toroid, which are measured via Superconducting Quantum Interference Devices (SQUIDs). Classical CCC beam monitors make use of a high magnetic permeability core as a flux-concentrator for the pickup coil. The core increases the pickup inductance and thus coupling to the beam, but unfortunately also raises low-frequency noise and thermal drift. In the new concept from the Leibniz Institute of Photonic Technology the Coreless Cryogenic Current Comparator (4C) completely omits this core and instead uses highly sensitive SQUIDs featuring sub-micron cross-type Josephson tunnel junctions. Combined with a new shielding geometry a compact and comparably lightweight design has been developed, which exhibits a current sensitivity of about 6 pA/sqrt(Hz) in the white noise region and a measured shielding factor of about 134 dB. The measurements were done in the Cryo-Detector Lab at the University of Jena.

Traditionally, the pickup coil is a full-wrap single turn coil around a high-permeability ring core. This core acts as a flux concentrator to make the system highly sensitive [1]. On the other hand, the core dominates the noise and drift behaviour of the CCC. It may therefore be useful to give up the ring core and to compensate for the loss of sensitivity on the SQUID side. Such a coreless CCC (4C) was designed and prepared at the Leibniz IPHT (see Fig. 1).

As it was to be expected from the first pulse measurements, the 4C noise is currently still somewhat above that of the CCCs with flux concentrator core (see Fig. 2). Further SQUID optimization should improve white noise (1 kHz to 100 kHz). The sensitivity to mechanical vibrations in the range between 5 Hz and 1 kHz should be counteracted constructively in the next 4C. The reason for the

higher low-frequency 1/f-noise in the range 50 mHz to 1 kHz is unclear at the moment and object of further research.

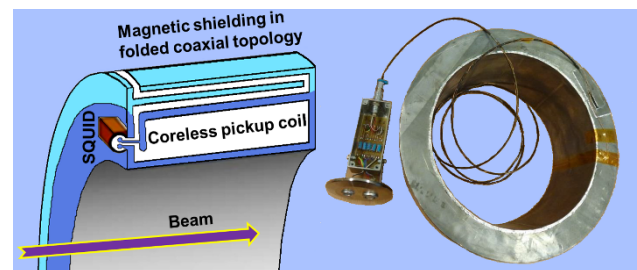


Figure 1: Pb-4C principle (left) in a folded coaxial topology and the realization (right) with a 270 mm inner-diameter including cable to the room-temperature filter box.

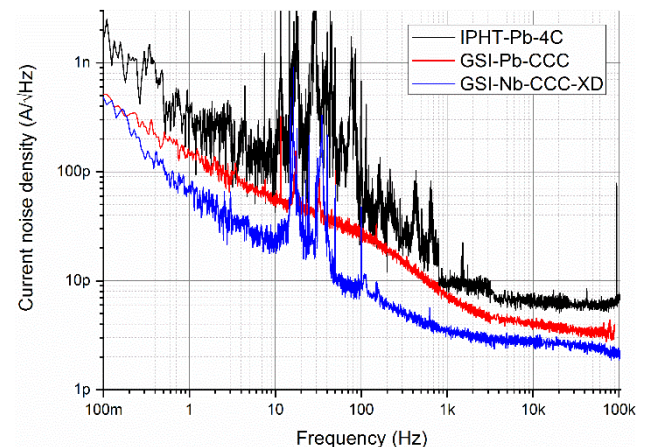


Figure 2: Comparison of the noise spectra of three CCCs. With core: Red in the middle, GSI-Pb-CCC in 2015 (4 pA/sqrt(Hz) white noise); blue at the bottom, GSI-Nb-CCC-XD in 2017 (3 pA/sqrt(Hz) white noise). Without core: Black at the top, IPHT-Pb-4C in 2019 (6 pA/sqrt(Hz) white noise).

References

- [1] K. Grohmann et al., “A cryodevice for induction monitoring of dc electron or ion beams with nano-ampere resolution”, in Superconducting quantum interference devices and their applications, Walter de Gruyter & Co, Berlin, New York, 1977, pp. 311-322.

* Work supported by BMBF, project numbers 05P15SJRBA and 05P18SJRBA1 and is a shortened version of the paper MOPP008 represented at the IBIC'19, Malmö, Sweden, Sep. 2019

[‡]v.tympel@gsi.de

Analysis of Fe X-Ray Spectra from the S-EBIT-I taken with a maXs-30 Detector

M. O. Herdrich^{#1,2,3}, A. Fleischmann⁴, D. Hengstler⁴, C. Enss⁴, S. Trotsenko²,
T. Morgenroth², R. Schuch⁵, G. Weber^{1,3}, and Th. Stöhlker^{1,2,3}

¹HI-Jena, Germany; ²GSI, Darmstadt, Germany; ³IOQ, University Jena, Germany; ⁴KIP, University Heidelberg, Germany; ⁵MSI, University Stockholm, Sweden

This report covers the first analysis of data taken by a maXs-30 series microcalorimeter based x-ray spectrometer at the S-EBIT-I at GSI in 2019. A new algorithm is presented for calibrating spectra with deformed peak shapes and overall low counts per bin.

In recent years, cryogenic microcalorimeters like the maXs-series metallic-magnetic detector array developed by the group of C. Enss [1] have proven to be a promising tool in the field of x-ray spectrometers for atomic physics application. Due to their working principles they combine a high energy resolution $E/\Delta E > 3000$ with a broad energy acceptance range of up to three orders of magnitude [2]. In order to benchmark the performance of such a detector in a realistic experiment environment, a measurement was carried out in 2019 at the S-EBIT-I on the site of GSI using a maXs-30 spectrometer. The detector consists of 64 metallic-magnetic microcalorimeter channels and has a resolution of up to 5 eV FWHM in a range between 100 eV and 100 keV by design.

During the experiment the microcalorimeter detector continuously recorded x-ray photons emitted from the interaction region of electrons with ions in the S-EBIT-I operating at 10 keV electron energy. A ferrocene gas source was used to supply Fe ions into the EBIT. Additionally, a ²⁴¹Am source was present for calibration of the EBIT spectra. The analysis of the raw data from the calorimeter is performed utilizing the finite response filter-based algorithm developed at the HI-Jena during the last years. A low overall count rate together with distortions of the spectrum due to a high susceptibility of the detector to vibrations leading to temperature fluctuations made a consistent energy calibration of the individual detector channels relative to each other challenging. Therefore a new calibration algorithm was implemented and tested in order to find the best match M_{opt} between two spectra f and g :

$$M_{opt} = \max_{a,b,c} \sum_i f_i(E) \cdot g_i(a + bE + cE^2)$$

The overlap of two spectra is measured using the sum over their pointwise product. One of the spectra is panned and stretched relative to the other. Utilizing the Nelder-Mead method (downhill simplex) the optimal parameter set for

the highest overlap is determined. This algorithm is a variation on the classical auto-focus method used by many digital cameras. It is applied to all detector channel spectra subsequently in order to match them all to each other.

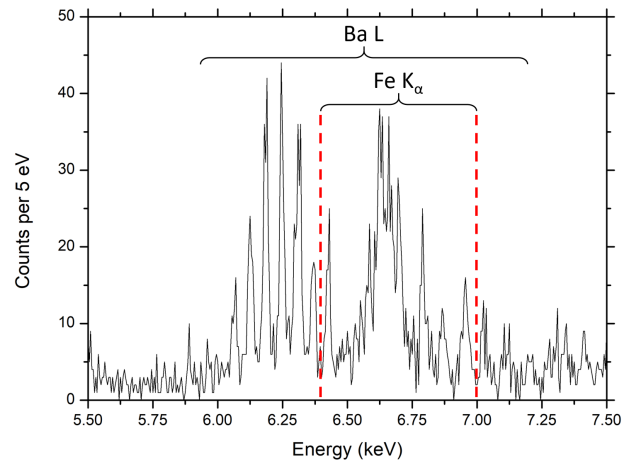


Figure 1: An x-ray spectrum recorded by the maXs-30 from the S-EBIT-I at 10 keV electron energy with a ferrocene source. The K-shell transitions of iron and L-shell transitions of barium in various charge states are present.

Shown in figure 1 is a preliminary spectrum containing K_{α} transitions of several charge states of iron ions as well as L-shell transitions from barium (from the EBIT cathode). A numerical optimization of the finite response filter window size improved the single channel energy resolution to 21 eV FWHM at 59.5 keV photon energy. The auto-focus algorithm yielded an improvement from 40 to 24 eV FWHM by resolving mismatching energy calibrations between the detector channels.

We acknowledge financial support by the European Union and the federal state of Thuringia via Thüringer Aufbaubank within the ESF project (2015 FGR 0094).

References

- [1] D Hengstler et al., Phys. Scr. **T166** (2015)
- [2] S Kempf et al., Supercond. Sci. Technol. **28** (2015)

[#]m.o.herdrich@gsi.de

Theory

Elastic Photon Scattering on Hydrogenic Atoms Near Resonances

Dmitrii Samoilenko^{*1,2,3}, Andrey V. Volotka^{1,3}, and Stephan Fritzsche^{1,2,3}

¹Helmholtz Institute Jena, Germany; ²Theoretisch-Physikalisches Institut, Friedrich-Schiller-Universität, Jena, Germany; ³GSI, Darmstadt, Germany

We investigated Rayleigh scattering on heavy hydrogen-like ions theoretically [1]. Focusing on Gamma Factory initiative at CERN, we chose the example of Pb^{81+} ion with photon energy close to $1s \rightarrow 2p$ transitions. Calculations are performed in rigorous QED-based treatment, as well as within two approximations: relativistic and non-relativistic. In contrast to the non-relativistic one, formulas in relativistic approximation, derived in this work explicitly, provide $\sim 10\text{-}20\%$ accuracy for observables within reasonable range of photon energies near resonances.

Scattering of light on atoms is a widely used technique for characterization and tailoring of properties of both photons and atoms. Here, we focus on the case of photon energy being close to certain electronic transition, which we call resonant case. We also focus on elastic component of photon scattering, so-called Rayleigh scattering. We employ well-developed theoretical tools of quantum electrodynamics (QED) for rigorous calculations of the scattering process, namely angle-differential cross section and polarization of the scattered light. Our goal is to derive analytical expressions describing the observables and verify their accuracy. Such expressions can be used for designing an experiment, that involves resonant Rayleigh scattering. Our focus lies on Gamma Factory initiative [2], where Rayleigh scattering on highly charged heavy ions is proposed as a high intensity and high photon energy γ -ray source.

The expressions are derived in two *resonant electric-dipole* approximations. This means that, in contrast to QED treatment, we neglect two things: (i) effects of all states, except for the resonant one; (ii) all types of transitions, except for the electric-dipole one. The first approximation is *non-relativistic*, currently used by Gamma Factory study group. The second one is *relativistic*, derived in this work in details. Results obtained in both approximations are compared to *exact* QED calculations to determine their accuracy. The relativistic approximation is also tested for stability with respect to photon energy detuning from the resonance.

Calculations are performed for example of H-like lead ion Pb^{81+} . For exact calculations and relativistic approximation we considered $1s_{1/2} \rightarrow 2p_{1/2}$ and $1s_{1/2} \rightarrow 2p_{3/2}$ as resonant transitions. For the non-relativistic approximation the two transitions are degenerated into one $1s \rightarrow 2p$ transition. Based on the results presented in Figure 1, we conclude that the non-relativistic approximation fails to de-

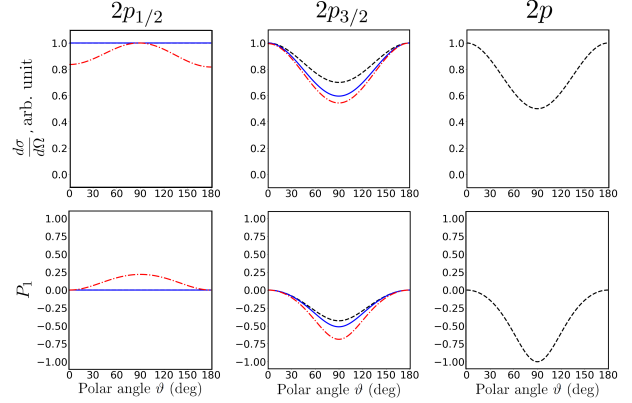


Figure 1: Cross section and polarization angular distribution for different resonant states: $2p_{1/2}$ - left column, $2p_{3/2}$ - middle column, and nonrelativistic $2p$ state - right column. Dashed black line - relativistic resonant electric dipole approximation, dash-dotted red line - exact calculations for the “off-resonance” scenario (see text), solid blue line - exact calculations at the corresponding resonance. Incident light is assumed to be circularly polarized.

scribe angular distribution of the scattered light, as well as its polarization state. At the same time, the relativistic approximation provides $\approx 10\%$ accuracy, while the photon energy is within 5 natural linewidths range near the resonance. We have also found out, that the accuracy of this approximation drops down to $\approx 20\%$, when the photon energy is 30 linewidths “off” the resonance.

Therefore, we find that relativistic resonant electric-dipole approximation provides satisfactory accuracy in reasonable range of photon energies near resonances. We suggest using this approximation for evaluation of scattered light properties for design of experiments, such as proposed by Gamma Factory initiative.

References

- [1] D.Samoilenko, A.V. Volotka, S. Fritzsche, “Elastic Photon Scattering on Hydrogenic Atoms Near Resonances”, *Atoms* 8(2), 12 (2020) .
- [2] M.W. Krasny, The Gamma Factory proposal for CERN, arXiv:1511.07794.

* dmitrii.samoilenko@uni-jena.de

Characterization of opening angle correlations of a biphoton state decomposed in Bessel modes

Baghdasar Baghdasaryan^{*1,2}, Fabian Steinlechner³, and Stephan Fritzsche^{1,2}

¹Helmholtz Institute Jena, Germany; ²Fraunhofer Institute for Applied Optics and Precision Engineering IOF, Germany;

³Theoretisch-Physikalisches Institut, Friedrich-Schiller-Universität Jena, Germany.

This work is a theoretical investigation of the process of spontaneous parametric down-conversion (SPDC). In SPDC a nonlinear crystal is pumped with a laser to create entangled pairs of photons. The entangled state of photon pairs, also known as biphoton state, is decomposed in Bessel modes, which also enables to investigate the non-degenerate SPDC process. Furthermore, we discussed optimization conditions for an efficient generation of entangled pairs. In particular, the proper choice of such parameters as the beam waist of the pump beam, the length of the crystal, and selected orbital angular momentum of photon pairs enable to control the rate and the strength of entanglement.

Spontaneous parametric down-conversion is a way to generate entangled photon pairs, where a strong pump field interacts with a nonlinear crystal to create pairs of photons. A crystal is called *nonlinear*, depending on the symmetry properties of its lattice. The rate at which SPDC can create entangled photons is up to hundreds of thousands per second in a narrow frequency band. Therefore, SPDC is one of the most popular processes for the generation of entangled photons.

Theoretical and experimental studies have shown that the photon pair produced by SPDC are naturally entangled in OAM modes. OAM is a very convenient quantum observable, because, firstly, eigenstates of OAM can be efficiently prepared, unitary manipulated, and measured, which are essential steps in quantum communication protocols. We considered Bessel beams, which also carry OAM if the paraxial approximation is valid [1] and use them to describe the spatial structure of the biphoton state. In addition to OAM, we also considered the radial degree of freedom of biphoton state, which can be presented by a continuous observable called opening angle of Bessel beam.

The Bessel modes have been used to represent the spatial correlations of photon pairs. In particular, the description of the radial degree of freedom by the transverse momentum of Bessel modes. We introduced a new approach, namely, the utilization of the opening angle of the Bessel beam to represent the radial degree of freedom. The opening angle and the radial momentum can be equivalently used for the description of Bessel modes. However, the main difference between the opening angle and the radial momentum is that the correlations regarding the opening angle depends on the ratio of energies of the down-converted photons in contrast to correlation regarding the radial momentum. This fact can be useful for the direct in-

vestigation of nondegenerate SPDC process. We therefore express the spatial structure of the biphoton state in terms of Bessel modes.

We found optimization conditions, which enable us to control both the rate and the strength of the correlation. For instance, the pump beam waist affects the strength of the correlation. It leads to delta-correlation between transverse momenta of the down-converted photons when the beam waist attends to infinity. Such kind of conditions was also found for OAM and energies of photon pairs, energy of the pump photon, and the length of the crystal. On the other hand, the description of the radial degree of freedom of a biphoton state by the opening angle of the Bessel beam is found out to be a convenient approach. Firstly, the correlation measurements regarding the opening angle are easy to realize. Secondly, this kind of measurement enables the investigation of the non-degenerate biphoton states, which were neglected in the previous works. Our investigations offer new tools for the control of high dimensional entanglement experiments. For the demonstration, we present an example of such kind of correlation between the opening angle of down-converted photons, where we analyzed the crystal-length dependence.

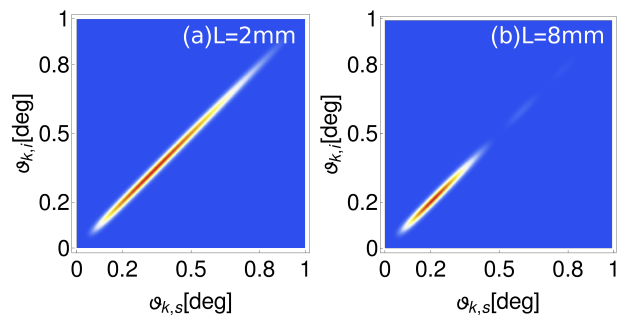


Figure 1: Correlation between $\vartheta_{k,s}$ and $\vartheta_{k,i}$ for different crystal lengths $L = 2$ mm, 8 mm. By increasing the crystal length, the correlation between opening angles of signal and idler beams vanishes along diagonal for large opening angles.

References

- [1] B. Baghdasaryan, B. Böning, W. Paufler, and S. Fritzsche Phys. Rev. A, **99**, 023403 (2019).

* baghdasar.baghdasaryan@uni-jena.de

Polarization-dependent high-intensity Kapitza-Dirac effect in strong laser fields

B. Böning^{*1,2}, W. Paufler^{1,2}, and S. Fritzsche^{1,2}

¹Helmholtz Institute Jena, Germany; ²Friedrich-Schiller-University Jena, Germany

The Kapitza-Dirac effect (KDE) describes the deflection of electrons by an intense standing light wave [1]. If, instead of a free-electron beam, the electrons are generated by above-threshold ionization (ATI) driven by the standing wave itself, the deflection is strongly enhanced (high-intensity KDE). We use a complete quantum description of this process to compute the momentum transfer to low- and high-energy photoelectrons in elliptically polarized standing waves. Our model predicts experimental conditions under which low-energy photoelectrons can be generated with high and controllable longitudinal momenta.

In ATI, an atomic target is ionized and the emitted photoelectrons absorb more photons than needed to overcome the ionization threshold. If the ionizing laser beam is a standing wave formed by two counter-propagating modes of identical wavelength λ and intensity I , an electron may absorb N photons from one mode and emit the same number into the other, which changes its momentum by $2N\hbar k$ while leaving its energy constant. This virtual Compton scattering leads to the high-intensity KDE. To theoretically describe this process, we apply a nondipole formulation of the strong-field approximation (SFA) that we adapted to laser fields with arbitrary spatial dependence [3].

Fig. 1 shows the resulting angular distributions of photoelectrons in the plane spanned by the beam axis (horizontal) and the polarization direction (vertical) for a linearly polarized standing wave. The red dashed curve belongs to photoelectrons with kinetic energy $E_p = 9.0$ eV at the detector, which is large compared to the ponderomotive energy $U_p \approx 4$ eV of the standing wave. The maxima correspond to a momentum transfer of $\Delta p_z \approx 850\hbar k$ to the photoelectron, which agrees with the experiment [2]. However, low-energy photoelectrons with $E_p < U_p$ were not accessible in past experiments. The black curve ($E_p = 2.8$ eV) in Fig. 1 shows a second set of maxima, corresponding to a much larger momentum transfer $\Delta p_z \approx 1240\hbar k$. These different results for low- and high-energy photoelectrons can be understood in analogy to the free-electron KDE: If the electron's kinetic energy is sufficient to move over the crests of the ponderomotive potential ($E_p > U_p$), it can be described classically, leading to a distinct value of its momentum at the detector. On the other hand, if the electron's motion is bounded by the potential crests ($E_p < U_p$), different paths interfere quantum mechanically, giving rise to another maximum in the polar-angle distributions. Our calculations show that due to the conservation of angular

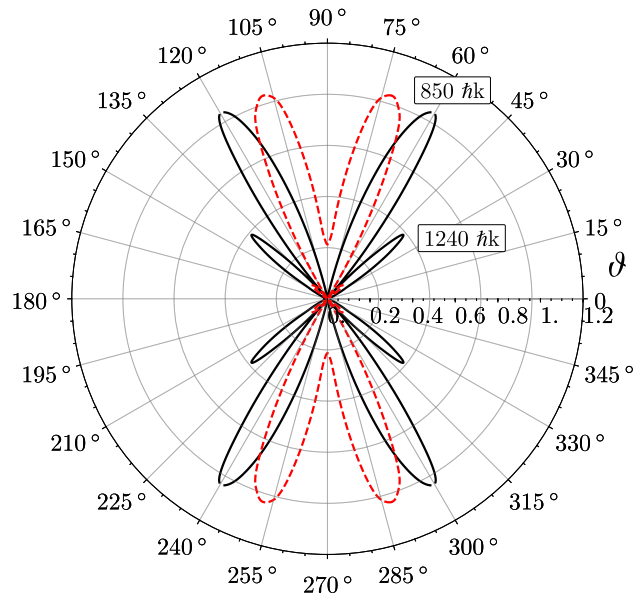


Figure 1: Normalized polar-angle distributions of photoelectrons in the ATI with linearly polarized standing light waves. Shown are high-energy ($E_p = 9.0$ eV $> U_p$; red dashed curve) and low-energy ($E_p = 2.8$ eV $< U_p$; black solid curve) photoelectrons. The labels denote the momentum transfer corresponding to the maxima. Parameters: $I = 1.5 \times 10^{14}$ W/cm², $\lambda = 1200$ nm, Kr target. [3]

momentum in the laser-electron interaction, the momentum transfer can be controlled via the ellipticity of the standing light wave. In particular, the emission of low-energy photoelectrons with large momentum transfer can be enhanced.

Since the SFA underestimates the yield of low-energy photoelectrons due to the neglect of the atomic potential in the electron continuum, we expect that the effect reported here is even more pronounced in experiments. Furthermore, semi-classical simulations promise to give more insight into the different dynamics of low- and high-energy photoelectrons in the standing light wave, especially for elliptical polarization.

References

- [1] P. L. Kapitza and P. A. M. Dirac, *Math. Proc. Cambridge Philos. Soc.* **29**, 297 (1933).
- [2] P. H. Bucksbaum et al., *Phys. Rev. Lett.* **61**, 1182 (1988).
- [3] B. Böning et al., *Phys. Rev. A* **99**, 053404 (2019).
- [4] B. Böning et al., *Phys. Rev. A* **101**, 031401(R) (2020).

* birger.boening@uni-jena.de

All-Loop Result for the Strong Magnetic Field Limit of the Heisenberg-Euler Effective Lagrangian

Felix Karbstein^{*1,2}

¹Helmholtz Institute Jena, Germany; ²Theoretisch-Physikalisches Institut, FSU Jena, Germany

We provide an explicit expression for the strong magnetic field limit of the Heisenberg-Euler effective Lagrangian for quantum electrodynamics. To this end, we show that the strong magnetic field behavior is fully determined by one-particle reducible contributions discovered only recently. The latter can efficiently be constructed in an essentially algebraic procedure from lower-order one-particle reducible diagrams. Remarkably, the leading strong magnetic field behavior of the all-loop Heisenberg-Euler effective Lagrangian only requires input from the one-loop Lagrangian. Our result revises previous findings based exclusively on one-particle irreducible contributions.

The Heisenberg-Euler effective Lagrangian [1] is a central quantity in the development of quantum field theory. It studies the effect of quantum fluctuations on the effective theory of prescribed constant electromagnetic fields in the vacuum, and allows for the systematic derivation of quantum corrections to Maxwell's classical theory of electrodynamics. The latter manifest themselves in effective, non-linear self-couplings between electromagnetic fields, giving rise to light-by-light scattering phenomena. In electric fields the Heisenberg-Euler effective Lagrangian \mathcal{L}_{HE} develops an imaginary part which can be associated with an instability of the quantum vacuum towards the formation of a state featuring real electrons and positrons.

As in the derivation of \mathcal{L}_{HE} the dynamical fermion and photon fields are integrated out, \mathcal{L}_{HE} can be represented in terms of Feynman diagrams featuring internal fermion and photon lines only. In turn, the only physical dimensionful scale inherited by \mathcal{L}_{HE} from the microscopic theory of QED is the electron mass m . Each coupling of a photon to a fermion line is mediated by the elementary charge $e = \sqrt{4\pi\alpha}$, implying that each internal photon line comes with a factor of α . On the other hand, the external field dependence of any loop diagram is entirely in terms of the combined parameter $eF^{\mu\nu}$. The latter combination actually forms a renormalization group invariant, and hence is independent of the renormalization scale. Correspondingly, it is convenient to formally treat the parameter α and the combination $eF^{\mu\nu}$ as independent. The power of the former counts the number of internal photon lines in a given diagram, and the power of the latter the number of couplings to the external fields.

The Heisenberg-Euler effective Lagrangian admits a diagrammatic expansion in the number of loops ℓ of the con-

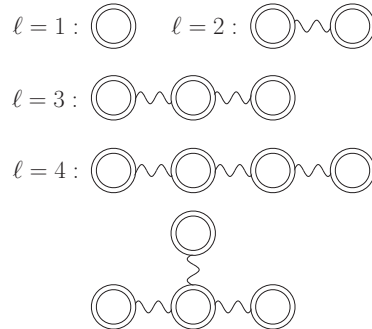


Figure 1: Topologically distinct diagrams constituting $\mathcal{L}_{\text{1PR}}^{\ell\text{-loop}}$ up to four loops. The double solid line denotes the charged-particle propagator dressed to all orders by the background field.

stituting Feynman diagrams,

$$\mathcal{L}_{\text{HE}} = \sum_{\ell=0}^{\infty} \mathcal{L}^{\ell\text{-loop}}, \quad (1)$$

where $\mathcal{L}^{0\text{-loop}} = -\frac{1}{4}F_{\mu\nu}F^{\mu\nu}$ is the classical Maxwell Lagrangian. The ℓ -loop contribution scales as $\mathcal{L}^{\ell\text{-loop}} \sim (\frac{\alpha}{\pi})^{\ell-1}$, where $\alpha \equiv \alpha(m^2) = \frac{e^2}{4\pi} \simeq \frac{1}{137}$ is the fine-structure constant. Contributions beyond one loop generically decompose into one-particle irreducible (1PI) and one-particle reducible (1PR) diagrams [2], such that for $\ell \geq 2$ we have $\mathcal{L}^{\ell\text{-loop}} = \mathcal{L}_{\text{1PI}}^{\ell\text{-loop}} + \mathcal{L}_{\text{1PR}}^{\ell\text{-loop}}$.

In Ref. [3] have explicitly determined the strong magnetic field limit of the Heisenberg-Euler effective Lagrangian. After demonstrating that beyond one loop this limit is fully determined by 1PR contributions, we extracted the leading contribution at each loop order ℓ . See Fig. 1 for an illustration of 1PR diagrams. In a next step, we resummed these leading contributions to obtain the leading strong magnetic field behavior of the all-loop Heisenberg-Euler effective Lagrangian. This result could then be straightforwardly translated to the case of a purely electric field, by means of the replacement $B \rightarrow -iE$.

This work has been funded by the DFG under Grant No. 416607684 within the Research Unit FOR2783/1.

References

- [1] W. Heisenberg and H. Euler, Z. Phys. **98**, 714 (1936).
- [2] H. Gies and F. Karbstein, JHEP **1703**, 108 (2017).
- [3] F. Karbstein, Phys. Rev. Lett. **122**, 211602 (2019).

*f.karbstein@gsi.de

Boosting Quantum Vacuum Signatures by Coherent Harmonic Focusing

Felix Karbstein^{*1,2}, Alexander Blinne¹, Holger Gies^{1,2}, and Matt Zepf^{1,3}

¹Helmholtz Institute Jena, Germany; ²Theoretisch-Physikalisches Institut, FSU Jena, Germany; ³Institut für Optik und Quantenelektronik, FSU Jena, Germany

We show that coherent harmonic focusing provides an efficient mechanism to boost all-optical signatures of quantum vacuum nonlinearity in the collision of high-intensity laser fields, thereby offering a promising route to their first experimental detection. Assuming two laser pulses of given parameters at our disposal, we demonstrate a substantial increase of the number of signal photons measurable in experiments where one of the pulses undergoes coherent harmonic focusing before it collides with the fundamental-frequency pulse. Imposing a quantitative criterion to discern the signal from the background of the driving laser photons and accounting for the finite purity of polarization filtering, we find that signal photons arising from inelastic scattering processes constitute a promising signature.

The quantum vacuum has remarkable properties. It is not trivial and inert, but amounts to a complex state whose properties are fully determined by quantum fluctuations. As these fluctuations comprise all existing particles, the quantum vacuum even constitutes a portal to new physics beyond the Standard Model of particle physics. To obtain a measurable response, the quantum vacuum has to be probed by some external stimulus. A powerful means is provided by strong macroscopic electromagnetic fields which couple directly to the charged particle sector. Within the Standard Model, the leading effect arises from the effective coupling of the prescribed electric \vec{E} and magnetic \vec{B} fields via a virtual electron-positron pair. This process is governed by quantum electrodynamics (QED) and supplements Maxwell's classical theory in vacuum with effective nonlinear couplings of the electromagnetic fields. Up to now, the corresponding deviations have never been directly observed for macroscopically controlled fields. This is because the effective interactions are parametrically suppressed by powers of $|\vec{E}|/E_{\text{cr}}$ and $|\vec{B}|/B_{\text{cr}}$, with $E_{\text{cr}} \simeq 1.3 \times 10^{18} \frac{\text{V}}{\text{m}}$ and $B_{\text{cr}} \simeq 4 \times 10^9 \text{ T}$, respectively.

In Ref. [1], we showed that the number of attainable and, in particular, discernible signal photons can be increased significantly for a given laser pulse energy put into the interaction volume. To this end, we relied on the mechanism of coherent harmonic focusing (CHF), pioneered by Ref. [2]. Our quantitative analysis is based on the novel numerical approach [3] allowing for first-principles simulations of photonic signatures of vacuum nonlinearities. As a concrete example, we employed CHF to boost photonic signatures of QED vacuum nonlinearity in the head-on collision of two linearly polarized high-intensity laser fields of

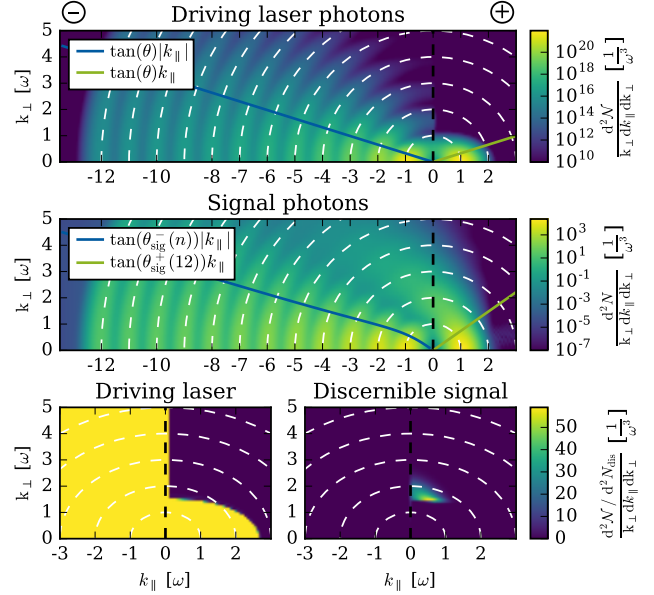


Figure 1: Spectra of the driving laser photons and signal photons attainable in a polarization insensitive measurement. In the highlighted example, the fundamental-mode laser pulse propagates in “+” direction and collides head-on with a CHF pulse made up of 12 harmonics. White dashed circles indicate lines of constant photon energy. The bottom panels focus on the spectral domain where the differential number of signal photons surpasses the differential number of driving laser photons.

given parameters. See Fig. 1 for an illustration.

We are confident that our findings will stimulate many further theoretical proposals as well as dedicated experimental campaigns aiming at the first verification of quantum vacuum nonlinearity using CHF and replications based on conventional higher-harmonic generation techniques.

This work has been funded by the DFG under Grant Nos. 416611371; 416607684; 416702141; 416708866 within the Research Unit FOR2783/1.

References

- [1] F. Karbstein, A. Blinne, H. Gies and M. Zepf, Phys. Rev. Lett. **123**, 091802 (2019).
- [2] S. Gordienko, A. Pukhov, O. Shorokhov and T. Baeva, Phys. Rev. Lett. **94**, 103903 (2005).
- [3] A. Blinne, H. Gies, F. Karbstein, C. Kohlfürst and M. Zepf, Phys. Rev. D **99**, 016006 (2019).

*f.karbstein@gsi.de

X-ray photon scattering at a focused high-intensity laser beam

Felix Karbstein^{*1,2} and Elena A. Mosman³

¹Helmholtz Institute Jena, Germany; ²Theoretisch-Physikalisches Institut, FSU Jena, Germany; ³National Research Tomsk Polytechnic University, Russia

We study x-ray photon scattering in the head-on collision of an XFEL pulse and a focused high-intensity laser pulse, described as paraxial Laguerre-Gaussian beam of arbitrary mode composition. For adequately chosen relative orientations of the polarization vectors of the colliding laser fields, this gives rise to a vacuum birefringence effect manifesting itself in polarization flipped signal photons. As previously demonstrated for the special case of a fundamental paraxial Gaussian beam, this scenario is generically accompanied by a scattering phenomenon of x-ray energy signal photons outside the forward cone of the XFEL beam, potentially assisting the detection of the effect in experiment. Here, we study the fate of the x-ray scattering signal under exemplary deformations of the transverse focus profile of the high-intensity pump.

Quantum electrodynamics (QED) predicts effective nonlinear interactions of electromagnetic fields mediated by quantum fluctuations of electrons and positrons. In the low energy limit, these effective interactions are governed by the Heisenberg-Euler effective Lagrangian. For field strengths much smaller than the critical electric and magnetic fields, the leading effective interaction amounts to a four-field interaction.

The collision of x-ray photons and a high-intensity laser field constitutes one of the most prospective scenarios towards the first experimental verification of QED vacuum nonlinearities in macroscopic electromagnetic fields in the laboratory. The dominant signal arises from the quasi-elastic interaction of the incident x-ray photons with the intensity profile of the high-intensity laser. Recently, it has been demonstrated that the scattering of signal photons outside the forward cone of the x-ray beam can be used to significantly increase the signal-to-background ratio.

So far, all available studies of the effect have modeled the high-intensity laser pump as fundamental paraxial Gaussian beam. However, the details of the scattering process may depend sensitively on the precise spatio-temporal structure of the pump field, and in particular on its transverse intensity profile in the interaction region.

Reference [1] is devoted to a first exploratory study of the fate of the scattering signal under deformations of the transverse focus profile of the pump. To this end, we focus on the head-on collision of a weakly focused XFEL probe pulse with a tightly focused high-intensity laser pump pulse. More specifically, we assume the waist w_{probe} of the x-ray probe to be wider than the waist w_0 of

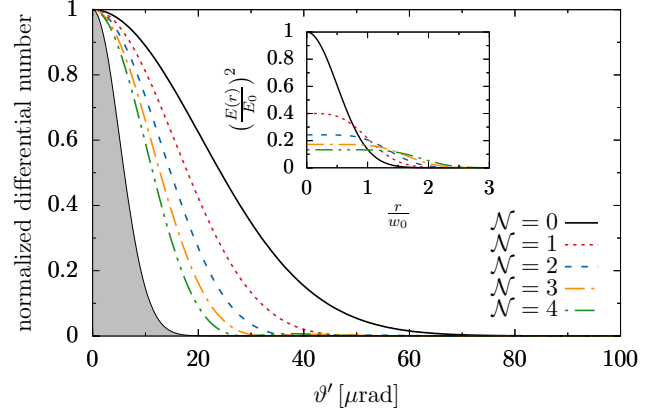


Figure 1: Far-field angular decay of the signal and probe (gray) for different transverse pump profiles. For the pump we consider flattened Gaussian beams of different order \mathcal{N} ; see the inset for the associated focus profiles. The plot is for a probe photon energy of $\omega = 12914$ eV, pump wavelength $\lambda = 800$ nm, pulse durations $\tau = T = 30$ fs and waist parameters $w_0 = 1000$ nm as well as $w_{\text{probe}} = 3w_0$.

the pump, thereby ensuring that the x-ray probe photons illuminate the full transverse pump profile. While the former is modeled as linearly polarized plane wave supplemented with a finite pulse duration, the latter is described as pulsed paraxial Laguerre-Gaussian beam of arbitrary mode composition [2]. In our explicit examples, we especially focus on pump pulses with flattened Gaussian focus profiles [3],

$$E_{\mathcal{N}}(r) = E_{0,\mathcal{N}} e^{-\left(\frac{r}{w_0}\right)^2} \sum_{k=0}^{\mathcal{N}} \frac{1}{k!} \left(\frac{r}{w_0}\right)^{2k}, \quad (1)$$

where $E_{0,\mathcal{N}}$ denotes the peak field amplitude. See Fig. 1 for an illustration of the effect for flattened Gaussian focus profiles of different orders $\mathcal{N} \in \mathbb{N}_0$. The general trend is as follows: the wider the pump, i.e., the larger \mathcal{N} , the narrower the scattering signal.

This work has been funded by the DFG under Grant No. 416607684 within the Research Unit FOR2783/1.

References

- [1] F. Karbstein and E. A. Mosman, Phys. Rev. D **100**, 033002 (2019).
- [2] F. Karbstein and E. A. Mosman, Phys. Rev. D **96**, 116004 (2017).
- [3] F. Gori, Optics Communications **107**, 335-341 (1994).

*f.karbstein@gsi.de

Breakdown of the electric dipole approximation in direct two-photon ionization

J. Hofbrucker^{*1,2,3}, *A. V. Volotka*^{1,2}, and *S. Fritzsche*^{1,2,3}

¹Helmholtz Institute Jena, Germany; ²GSI, Darmstadt, Germany; ³Friedrich-Schiller University Jena, Germany

According to predictions based on electric dipole approximation, an atom can be brought to a fully oriented state by two-photon ionization of one of its K -shell electrons, if the incident light is circularly polarized and its energy is tuned to a nonlinear Cooper minimum. We show that by inclusion of electric quadrupole interaction, dramatic drop of the orientation purity is obtained. The low degree of ion orientation provides a direct access to contributions of electron-photon interaction beyond electric-dipole approximation. The predicted ion orientation can be experimentally detected either directly using a Stern-Gerlach analyzer, or by means of subsequent $K\alpha$ fluorescence emission.

The interest in the inner-shell dynamics of atoms and molecules has been rising ever since excitation and ionization of the strongly bound electrons became accessible by the first XUV and x-ray light sources. Nowadays, it is also possible to probe these systems in nonlinear regime with free-electron lasers. That is why, in the last decade, much of experimental efforts have been paid to studying the fundamental properties of nonlinear light-matter interaction, and finding use in applied fields such as nonlinear spectroscopy [1, 2].

We consider the case of two-photon K -shell ionization of atoms by right-circularly polarized light. Due to the light polarization, the two electrons from the $1s$ subshell proceed via different electric dipole ionization pathways. While the spin down electron can be ionized through a single ionization pathway $s_{1/2} \rightarrow p_{1/2} \rightarrow \varepsilon_{d_{3/2}}$ only, both electrons can be ionized via an intermediate $p_{3/2}$ state. Consequently, passing through a nonlinear Cooper minimum, where the ionization pathways through the intermediate $p_{3/2}$ state vanish, one might expect a pure depletion of the spin down electron. However, this conclusion holds only in the electric dipole approximation.

In our work, we showed that in the case of two-photon ionization of K shell at nonlinear Cooper minima, accounting for beyond-dipole contributions becomes inevitable [3]. In other words, the fragile spin nature of the nonlinear Cooper minimum of a fine-structure channel gives us the opportunity to access multipole contributions in nonlinear light-matter interaction processes. To demonstrate the breakdown of the electron-dipole approximation on examples, we proposed similar conditions as considered in the recent experiments [1], where either ion, or fluorescence yields were detected as a signature of two-photon K shell ionisation. However, instead of solely detecting the yields,

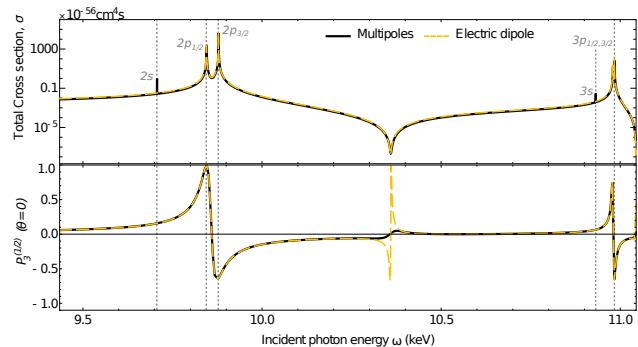


Figure 1: Direct two-photon ionization of germanium atom by two right-circularly polarized photons within electric dipole approximation (dot-dashed yellow), and including higher multipole orders (full, black). Top: Total photoionization cross section as function of incident photon energy. The nonlinear Cooper minimum is reflected into the cross section in a form of a local minimum around $\omega = 10.35$ keV. Bottom: Degree of circular polarization of subsequent $K\alpha$ fluorescence. Clear breakdown of the dipole approximation is visible at nonlinear Cooper minimum. [3].

we suggest to additionally carry out measurements of degree of polarisation of photoions or fluorescence photons. Figure presents the theoretical predictions of the total cross section as well as degree of polarization of $K\alpha$ fluorescence in the case of nonsequential two-photon ionisation of neutral germanium atoms. The nonlinear Cooper minimum can be clearly seen both in the values of the cross section (top), where it appears as a local minimum around $\omega = 10.35$ keV, as well as in the degree of polarization of $K\alpha$ fluorescence (bottom), where the strong variation between electric-dipole (dashed yellow) and multipole (full black) occurs [3].

Work supported by Bundesministerium für Bildung und Forschung (Grand No. 05K16FJA).

References

- [1] K. Tamasaku, *et al.* Nat. Photonics **8**, 313, (2014).
- [2] J. Szlachetko, *et al.* Sci. Rep. **6**, 33292, (2016).
- [3] J. Hofbrucker, A. V. Volotka, and S. Fritzsche, Sci. Rep. **10**, 3617 (2020).

*j.hofbrucker@gsi.de

Optimized Chirped Laser Pulses for Narrowband Inverse Compton Sources in the High-Intensity Regime

Daniel Seipt^{*1,2,3}, Vasily Yu. Kharin^{1,2}, and Sergey G. Rykovanov^{1,2,4}

¹Helmholtz Institute Jena, Germany; ²GSI, Darmstadt, Germany; ³University of Michigan, CUOS, Ann Arbor, USA;

⁴Skolkovo Institute of Science and Technology, Russia

The Inverse Compton Scattering (ICS) of laser light off high-energy electron beams is a well-established source of X- and gamma-rays for applications in medical, biological, nuclear, and material sciences. High-brightness ICS γ sources require high-intensity scattering lasers in general. Here we describe a method to generate optimized chirped laser pulses that compensate nonlinear spectrum broadening that inevitably occurs when the scattering laser is relativistically intense. The optimized pulses can be thought of as a superposition of two oppositely linearly chirped pulses, and delayed with respect to each other. By using those pulses in ICS, the peak spectral brightness of γ -rays can be increased by orders of magnitude.

We propose to synthesize an optimized laser spectrum using spectral interferometry. By working in frequency space, both the temporal pulse shape and the local laser frequency are adjusted simultaneously to fulfill as good as possible the compensation condition, $\omega_L(\varphi) = \omega_0[1 + a(\varphi)^2]$, where the frequency rises with the squared normalized laser vector potential $a(\varphi)$.

Our proposed scheme can be summarized as follows: An initially unchirped broadband laser pulse with the spectral amplitude $\tilde{a}_{in}(\omega)$ is split into two identical pulses. Each of these pulses is sent to the arms of an interferometer where a spectral phase $\tilde{\Phi}(\omega)$ is applied to one of the pulses and the conjugate spectral phase $-\tilde{\Phi}(\omega)$ is imposed onto the other one, using, e.g. a DAZZLER. The two pulses are coherently recombined causing a spectral modulation. In the time-domain this translates to the coherent superposition of two oppositely linearly chirped laser pulses which are delayed with respect to each other, see Fig. 1 (a).

By modeling the laser spectrum as Gaussian, and including spectral phase terms up to the second order, $\tilde{\Phi}(\omega) = \sum_{k=0}^2 B_k (\omega - \omega_0)^k / (k! \Delta\omega_L^k)$, we found analytic expressions for the synthesized laser pulses in the time-domain as function of the chirp parameters $\mathbf{B} = (B_0, B_1, B_2)$. These laser pulses were then used to simulate the ICS γ -ray spectrum using the Lienard-Wiechert potentials in the far field [1].

We need to find, for given a_0 and laser bandwidth, the optimized values of \mathbf{B} that minimize the spectral bandwidth (BW) of the scattered γ -rays and provides the largest peak spectral brightness (psb) of the ICS source. In Ref. [1] this has been achieved by both numerical optimization, and by developing an analytic model, see Fig. 1 (c).

Fig. 1 (d) shows the relative rms bandwidth of the ICS

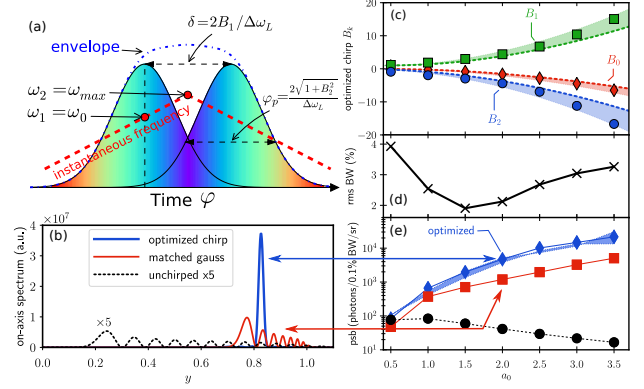


Figure 1: (a) Schematic sketch of the two-pulse model for generating optimized laser pulses for narrowband nonlinear ICS. (b) On-axis scattered photon spectra as function of $y = \omega/4\gamma^2\omega_0^2$ for $a_0 = 2$, $\Delta\omega_L/\omega_0 = 0.1$ (blue) in comparison to matched Gaussian (red) and unchirped pulses (black). Right panels: Optimal chirp parameters (c) that lead to the narrowest on-axis scattered photon spectrum (d) for given a_0 and $\Delta\omega_L/\omega_0 = 0.1$. Shaded areas are analytical model predictions [1] and symbols are from numerical optimization. (e) Peak spectral brightness (psb) of the on-axis scattered photons as a function of a_0 for the optimally chirped pulse (blue) and compared to matched Gaussian (red) and unoptimized cases (black).

photons, which is well below 4% throughout. It is evident that there is an optimal range of a_0 for the given laser bandwidth around $a_0 = 1.5$ where the bandwidth of the ICS photons is smallest. This optimal region shifts to higher a_0 for larger laser bandwidth. For large values of $a_0 > 3.5$, the quality of the photon spectrum decreases.

Fig. 1(e) shows the on-axis peak spectral brightness of the γ photons as a function of a_0 for the numerically optimized chirped pulses. It is several orders of magnitude larger than for unchirped pulses, and exceeds the matched Gaussian pulse by a factor of 4...5.

To verify the robustness of the presented two-pulse scheme with regard to 3D effects we performed numeric simulations of realistic LWFA electron bunches with focused optimized chirped laser pulses [1].

References

- [1] D. Seipt, V. Yu. Kharin, and S. G. Rykovanov, Phys. Rev. Lett. **122**, 204802 (2019).

*d.seipt@gsi.de

Propagation effects in multipass HHG from plasma surfaces

S. Tietze^{*1,2}, M. Zepf^{1,2}, and M. Yeung³

¹Helmholtz Institute Jena, Germany; ²Friedrich-Schiller-Universität Jena, Physikalisch-Astronomische Fakultät, Germany; ³School of Mathematics and Physics, Queen's University Belfast, United Kingdom

To enhance the efficiency of high order harmonics generated from plasma surfaces, a multipass scheme has been proposed. We show on the example of two targets, that it is not optimal to place the targets as close as possible, but at a certain distance to optimize the waveform of the pulse and thus maximize the efficiency. This is due to the Gouy phase shift changing the relative phase between multiple colours in a Gaussian beam.

Surface High Harmonic Generation (SHHG) has been considered as a promising route towards intense ultrashort XUV pulses generated in laser-plasma interactions. Several different techniques have been proposed since then to enhance the efficiency of the harmonic generation process. One technique is the mixing of several frequencies in the driving laser pulse by using multiple passes [1, 2, 3]. An important factor, which has not been considered so far, is the distance between two targets in a multipass setup. It is especially important for possible experiments to find the optimal distance, while still being practical from a technical point of view. As already outlined in previous work [2], the waveform of the driving laser pulse is important for the efficiency of the harmonic generation process. But due to the Gouy phase [4, 5], the waveform of a Gaussian pulse with multiple colours will change, even when propagating in free space. Furthermore, the Gouy phase shift is different, depending on the number of spatial dimensions. While this does not seem to be important for experiments in the three-dimensional real world, often two-dimensional Particle-in-Cell (PIC) simulation are used to support experimental data. Performing full scale 3D PIC simulations, especially of surface high harmonic generation in double reflection, would require a huge number of CPU-hours of computing time even for a single simulation. This was not feasible for this study, but it was possible to reproduce the effect using 1D PIC simulations. To model the free space propagation in higher dimensions between the two targets in a 1D PIC simulation, both the intensity and the phase had to be adjusted accordingly. The reflected pulse was obtained after the first target and, after a Fourier transform, the Gouy phase was artificially imposed on the pulse. Likewise the intensity was reduced according to the paraxial approximation. Afterwards the pulse was injected into another simulation for the interaction with the second target. The model was verified by comparing the results to full-scale 2D PIC simulations.

The Gouy phase shift changes the relative phase between multiple colours in a Gaussian beam while propagating.

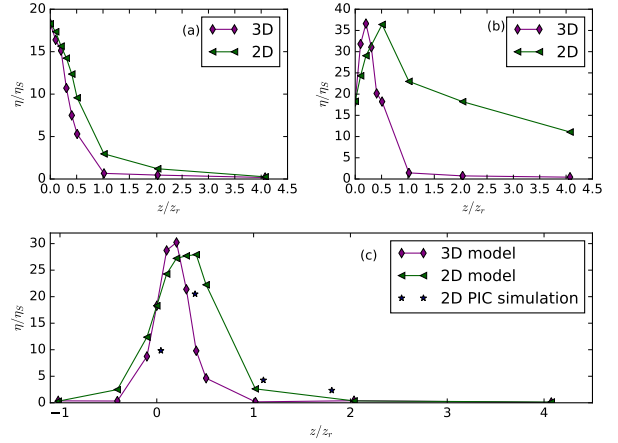


Figure 1: Dependence of the harmonic generation efficiency $\eta = I_{AP}/I_L$ (normalized to the single pass efficiency η_S) on the distance between the two targets. The attosecond pulse is obtained by applying a highpass filter which cuts out everything below the 20th harmonic. The pulse between the two targets has been modelled to reflect the intensity falloff only (a), the Gouy phase shift only (b) and the combined effect of both (c). The combined effect is also compared to full 2D simulations.

This also changes the resulting waveform, which has implication for multipass high order harmonics generation. As the waveform changes with the propagated distance, there exists an optimal distance between the two targets, where the harmonic generation efficiency on the second target is maximized. It is not optimal to just minimize the distance between the two targets, as one would assume purely from the intensity falloff alone. It is found that the harmonic generation efficiency peaks at $0.2z_r$ or $0.5z_r$ for 3D and 2D propagation geometry, respectively.

References

- [1] P. Zhang and A. G. R. Thomas, Appl. Phys. Lett. **106**, 131102 (2015)
- [2] M. R. Edwards and J. M. Mikhailova, Phys. Rev. Lett., **12**, 117 (2016)
- [3] Z. Lécz and A. Andreev, J. Opt. Soc. Am. B **35** (2018)
- [4] C. R. Gouy, Ann. Chim. Phys. Ser. 6, **24**, 145 (1891)
- [5] S. Feng and H. G. Winful, Opt. Lett., **8**, 26 (2001)

* s.tietze@gsi.de

Propagator from Nonperturbative Worldline Dynamics

Sebastián Franchino-Viñas^{2,3} and Holger Gies^{1,2}

¹Helmholtz Institute Jena, Germany; ²TPI, FSU Jena, Germany; ³Univ. Nacional de La Plata, Argentina

We use the worldline representation for correlation functions together with numerical path integral methods to extract nonperturbative information about the propagator to all orders in the coupling in the quenched limit (small- N_f expansion). We consider a simple scalar toy model (S²QED) for QED-like theories. Using a worldline regularization technique, we are able to analyze the divergence structure of all-order diagrams and to perform the renormalization of the model nonperturbatively. We compute the pole mass of the S²QED electron and observe sizable nonperturbative effects in the strong-coupling regime arising from the full photon dressing. We also find indications for the existence of a critical coupling where the photon dressing compensates the bare mass such that the electron mass vanishes.

In addition to Feynman diagram calculus for perturbative expansions of quantum field theory, the worldline method [1] has proved useful in both perturbative as well as nonperturbative applications in QED and beyond.

We have extended nonperturbative worldline methods to a computation of a full propagator in S²QED, a scalar QED toy model, combining a compact worldline representation for a large subclass of Feynman diagrams with information carried by the probability distribution function of a relevant worldline observable. This has enabled us to perform the renormalization of the model nonperturbatively and to compute the propagator of the scalar electron for large values of the coupling beyond the perturbative validity region.

The fully resummed subclass of diagrams is the dominant set in the formal small flavor $N_f \rightarrow 0$ limit. For the scalar electron propagator, it diagrammatically corresponds to the electron line dressed by all possible photon radiative corrections but without any additional electron loop. The computation becomes accessible in the worldline formalism as it corresponds to an expectation value of a worldline observable which we have been able to compute using the method of probability distribution functions.

This gives rise to a number of concrete results for the model: we observe that the propagator is always positive for the range of accessible coupling values, so that we observe no violation of reflection positivity. More precisely, we have analyzed the dependence of the propagator on the distance as a function of the coupling. The large distance behavior is governed by the physical (pole) mass corresponding to the inverse correlation length characterizing the propagator.

For small couplings, our nonperturbative results coincide with the loop approximation. Even though asymptotically

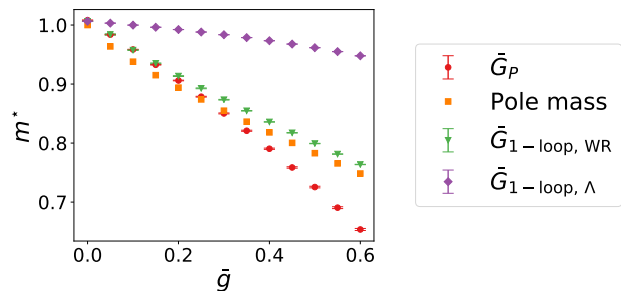


Figure 1: Nonperturbatively computed electron pole mass m^* (red circles) as a function of coupling strength \bar{g} compared with various perturbative estimates.

large distances are numerically difficult to deal with, the accessible distances already exhibit the expected asymptotic behavior and allow for a determination of the pole mass for comparatively large couplings $\bar{g} \sim 0.5$ (playing the role of the finestructure constant in S²QED).

From about $\bar{g} \sim 0.2$ on, we observe a clear deviation from the perturbative estimate, cf. Fig. 1. The inclusion of more diagrams corresponding to a full radiative dressing of the electron with a photon cloud reduces the physical pole mass compared to the leading-order perturbative estimate. Our results are compatible with the existence of a critical coupling value for which the physical mass approaches zero as a consequence of the radiative dressing.

Finally, we observe that the small-distances behaviour of the propagator is not affected by photonic corrections, neither perturbatively nor in the nonperturbative worldline computation. This provides evidence for the superrenormalizable structure of the theory as suggested by powercounting. As a result, the anomalous dimension of the scalar electron field in S²QED remains zero both in perturbation theory and beyond.

Work supported by (DFG) under Grant Nos. 416611371; 392856280 within FOR2783/1.

References

- [1] R. Feynman, Phys. Rev. **80**, 440-457 (1950)
- [2] S. Franchino-Viñas and H. Gies, Phys. Rev. D **100**, no.10, 105020 (2019).

Ponderomotive Scattering of Electrons for High-Intensity Laser Pulse Characterization

Thomas Teter^{*1,2}, Daniel Seipt^{1,3}, and Matt Zepf^{1,2,3}

¹Helmholtz Institute Jena, Germany; ²Friedrich-Schiller-Universität; ³GSI, Darmstadt, Germany

A precise determination of laser intensity in focus is of critical importance for experiments probing strong-field QED, such as the ones planned within the LUXE and FOR collaborations [1, 2]. We examine the possibility of such measurements by means of ponderomotive scattering of electrons from diffuse gas targets. Here the advantages of various target gases for measuring laser pulses at different intensities are compared.

This work investigates the electron energy and angular spectra emerging from the interaction of short, intense laser pulses with a gas target as a means of probing the laser strength, a_0 , in focus. Simulations were conducted using the particle-in-cell code EPOCH to investigate the features of the scattered electron spectra, and from which spectral features the laser strength can be accurately determined.

At high laser intensity, the outer-shell electrons, and in fact all electrons from low-Z gases, are ionized well before the peak of the laser pulse arrives. Those electrons never interact with the peak of the pulse and are thus not useful for determining the peak intensity. We compared various target gases including nitrogen, argon, and krypton to find the optimal target for strong field ionization of electrons at the peak for various intensity levels.

For weakly focused Gaussian pulses, the field distribution near focus and peak of field strength is nearly planar. The dynamics of the electron in such a field are well known theoretically. The minimum scattering angle of the electrons given by the peak laser amplitude is then:

$$\theta \approx \arctan(2/a_0) \quad (1)$$

where a_0 is the laser strength parameter. The highest energy electrons are ponderomotively scattered by fields near the peak of the laser pulse and have the largest drift velocity as compared to their transverse velocity [3]. Therefore, we examine the minimum scattering angles of the highest energy electrons to determine the peak value of laser strength.

We performed 2D-EPOCH simulations where a JETI-like laser pulse collides with a low density gas target. The laser's wavelength is $\lambda = 800$ nm, duration is $\tau = 40$ fs, and beam waist is $w_0 = 10 \mu\text{m}$. Intensity was permuted over 2.94×10^{18} , 10^{19} , 10^{20} , 10^{21} , and 10^{22} W/cm². Our targets were nitrogen, argon, and krypton at number density 1×10^{14} /cm³. As previously shown, we found all of the electrons of nitrogen are ionized and scattered well before the peak of the pulse arrives. We saw little difference between the scattered electron spectra of krypton and argon for the entire intensity range [4]. The peak of

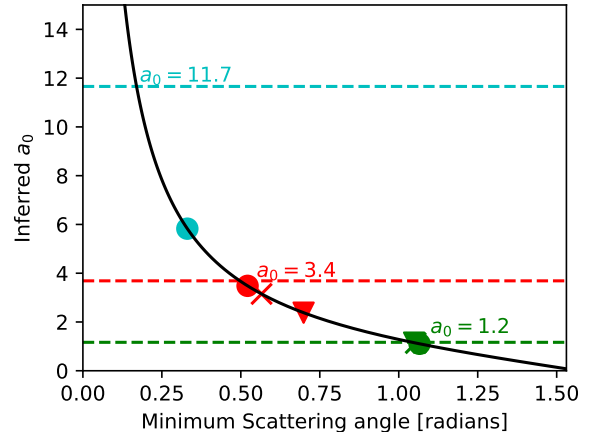


Figure 1: Peak laser strength as given by the minimum scattering angle according to Eqn. 1 (the black line). Different colors correspond to different input values of a_0 (dashed lines): green to $a_0 = 1.167$, red to $a_0 = 3.369$, and cyan to $a_0 = 11.66$. Circles are for simulations using krypton, crosses for argon, and triangles for nitrogen.

the scattered electron spectra also tends to underestimate laser strength as compared to the spectrum's high energy tail. Figure 1 shows the value of a_0 calculated from Eqn. 1 using the scattering angle of the highest energy simulation electrons. This technique predicts laser strength fairly well for weakly focused beams with intensities below 10^{21} W/cm², but consistently underestimates a_0 . For simulation inputs $a_0 = 1.2$ and 3.4 , krypton offers predictions accurate within 5.6% which show an advantage over Thomson scattering techniques [5].

This work is on-going and aims to establish a parameter space for which lasers the technique can be most accurate and precise. Our forthcoming simulations will provide a prediction for the accuracy of these measurements, the energy resolution required for detection, and the sensitivity of the technique to pulse duration and spotsize.

References

- [1] B. Heinemann, et al., arXiv:1909.00860 (2019).
- [2] F. Karbstein, *Particles* **3**, 39 (2020).
- [3] A. L. Galkin, et al., *Phys. Plasmas* **17**, 053105 (2010).
- [4] M. Kalashnikov, et al., *Laser Part. Beams* **33**, 361 (2015).
- [5] D. Umstadter, et al., *Nature Photon.* **11**, 514 (2017).

* thomas.christopher.teter@uni-jena.de

Two-photon sequential ionization of atoms by twisted- and plane-wave light

V. P. Kosheleva^{*1,2,3}, V. A. Zaytsev⁴, R. A. Müller^{1,5,6}, A. Surzhykov^{5,6}, and S. Fritzsche^{1,2,3}

¹Helmholtz Institute Jena, 07743 Jena, Germany; ²GSI Helmholtzzentrum für Schwerionenforschung GmbH, 64291 Darmstadt, Germany; ³Theoretisch-Physicalisches Institut, Friedrich-Schiller-Universität, 07743 Jena, Germany;

⁴Department of Physics, St. Petersburg State University, Universitetskaya naberezhnaya 7/9, 199034 St. Petersburg, Russia; ⁵Physikalisch-Technische Bundesanstalt, D-38116 Braunschweig, Germany; ⁶Technische Universität Braunschweig, D-38106 Braunschweig, Germany

Investigation of the interaction of the twisted (or vortex) light beams with the matter has become an important research topic with extensive applications. It is explained by the fact that these beams can carry a nonzero projection of the orbital angular momentum (OAM) onto the propagation direction. This projection being an additional degree of freedom provides a unique possibility to get a deeper insight into the role of the OAM in light-matter interactions.

In the present work, we perform the fully-relativistic investigation of the resonant sequential two-photon ionization of the neutral atoms by the combination of plane-wave and twisted Bessel light [1]. This process can be regarded as a two-step one. On the first step, the plane-wave photon excites the neutral sodium atoms ($Z = 11$) from their ground $3^2S_{1/2}$ state, while, on the second step, the photoionization of the $3^2P_{3/2}$ excited state by the vortex photon occurs. We evaluate the “twistedness”-induced effects, namely the influence of the kinematic parameters of twisted light such as opening angle, on both the angular distribution of the photoelectron and the circular dichroism. Here we propose to enhance these effects through the appropriate choice of the geometry of the considered process, namely, via adjusting the angle between the first, plane-wave and the second, twisted photon.

The Bessel-wave twisted photons possess the well-defined energy ω , helicity λ as well as the linear k_z and total angular m momenta projections onto the propagation direction. We fix the z axis along this direction. The Bessel-wave twisted photon is described by the vector potential [2, 3, 4]:

$$\mathbf{A}_{\varkappa m k_z \lambda}^{(tw)}(\mathbf{r}) = i^{\lambda-m} \int \frac{e^{im\varphi_k}}{2\pi k_{\perp}} \delta(k_{\perp} - \varkappa) \delta(k_{\parallel} - k_z) \times \mathbf{A}_{\mathbf{k}\lambda}^{(pl)}(\mathbf{r}) d\mathbf{k}. \quad (1)$$

where $\mathbf{A}_{\mathbf{k}\lambda}^{(pl)}$ standing for the vector potential of the plane-wave photon, k_{\parallel} and k_{\perp} are the longitudinal and transversal components of the momentum \mathbf{k} , respectively, and $\varkappa = \sqrt{\omega^2 - k_z^2}$ is the well defined transversal momentum. From Eq. (1), it is seen that in the momentum space, these Bessel states represent a cone with the opening angle $\theta_k = \arctan(\varkappa/k_z)$.

Now let us discuss the geometry of the process under investigation (see Fig. 1). As was mentioned before, the z axis is directed along the propagation direction of the sec-

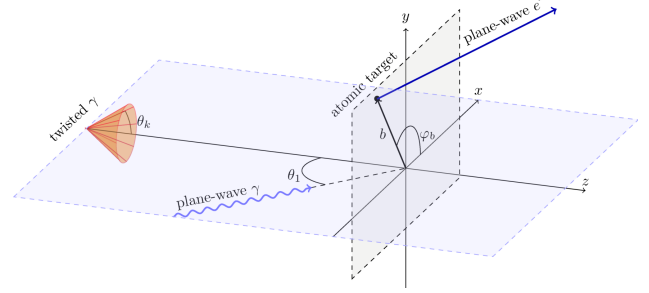


Figure 1: The geometry of the resonant sequential ionization of a single atom by the combination of plane-wave and twisted light.

ond, Bessel photon. The reaction x - z plane is formed by z axis and the direction of the wave vector of the first, plane-wave photon \mathbf{k}_1 . The position of the target atom is given by the impact parameter $\mathbf{b} = (b, \varphi_b, 0)$ in cylindrical coordinate.

In the present work, we consider the scenario of macroscopic target since most photoionization experiments deal with extended targets. We describe such a target as an incoherent superposition of atoms being randomly and homogeneously distributed.

We investigate the angular distribution of the photoelectron as well as the circular dichroism for different opening angles of the twisted photon θ_k and different angles between the first, plane-wave photon and the second, Bessel one θ_1 . It was found that the “twistedness” effects do significantly increase with θ_1 approaching 90° . That makes the case of $\theta_1 = 90^\circ$ the most promising scenario for the observation of these effects in the process under investigation.

References

- [1] V. P. Kosheleva, V. A. Zaytsev, R. A. Müller, A. Surzhykov, and S. Fritzsche, to be published.
- [2] O. Matula, A. G. Hayrapetyan, V. G. Serbo, A. Surzhykov and S. Fritzsche, *J. Phys. B* **46**, 205002 (2013).
- [3] U. D. Jentschura and V. G. Serbo, *Phys. Rev. Lett.* **106**, 013001 (2011); *Eur. Phys. J. C* **71**, 1571 (2011).
- [4] I. P. Ivanov and V. G. Serbo, *Phys. Rev. A* **84**, 033804 (2011).

* v.kosheleva@gsi.de

Publications

I. ARAPOGLOU, A. EGL, M. HÖCKER, T. SAILER, B. TU, A. WEIGEL, R. WOLF, H. ÇAKIR, V. A. YEROKHIN, N. S. ORESHKINA, V. A. AGABABAEV, A. V. VOLOTKA, D. V. ZINENKO, D. A. GLAZOV, Z. HARMAN, C. H. KEITEL, S. STURM, AND K. BLAUM

g Factor of Boronlike Argon $^{40}\text{Ar}^{13+}$

Physical Review Letters **122**, 253001 (2019).

S. ASNAFI, H. GIES, AND L. ZAMBELLI

BRST-invariant RG flows

Physical Review D **99**, 085009 (2019).

F. AUMAYR, K. UEDA, E. SOKELL, S. SCHIPPERS, H. SADEGHPOUR, F. MERKT, T. F. GALLAGHER, F. B. DUNNING, P. SCHEIER, O. ECHT, T. KIRCHNER, S. FRITZSCHE, A. SURZHYKOV, X. MA, R. RIVAROLA, O. FOJON, L. TRIBEDI, E. LAMOUR, J. R. C. LOPEZ-URRUTIA, Y. A. LITVINOV, V. SHABAEV, H. CEDERQUIST, H. ZETTERGREN, M. SCHLEBERGER, R. A. WILHELM, T. AZUMA, P. BODUCH, H. T. SCHMIDT, AND T. STÖHLKER

Roadmap on photonic, electronic and atomic collision physics: III. Heavy particles: with zero to relativistic speeds

Journal of Physics B: Atomic, Molecular and Optical Physics **52**, 171003 (2019).

B. BAGHDASARYAN, B. BÖNING, W. PAUFLER, AND S. FRITZSCHE

Dichroism in two-color above-threshold ionization with twisted XUV beams and intense infrared laser fields

Physical Review A **99**, 023403 (2019).

V. BAGNOUD, J. HORNING, M. AFSHARI, U. EISENBARTH, C. BRABETZ, Z. MAJOR, AND B. ZIELBAUER

Implementation of a phase plate for the generation of homogeneous focal-spot intensity distributions at the high-energy short-pulse laser facility PHELIX

High Power Laser Science and Engineering **7**, E62 (2019).

A. E. BARZAKH, J. G. CUBISS, A. N. ANDREYEV, M. D. SELIVERSTOV, B. ANDEL, S. ANTALIC, P. ASCHER, D. ATANASOV, D. BECK, J. BIEROŃ, K. BLAUM, CH. BORGMANN, M. BREITENFELDT, L. CAPPONI, T. E. COCOLIOS, T. DAY GOODACRE, X. DERKX, H. DE WITTE, J. ELSEVIERS, D. V. FEDOROV, V. N. FEDOSSEEV, S. FRITZSCHE, L. P. GAFFNEY, S. GEORGE, L. GHYS, F. P. HESSBERGER, M. HUYSE, N. IMAI, Z. KALANINOVÁ, D. KISLER, U. KÖSTER, M. KOWALSKA, S. KREIM, J. F. W. LANE, V. LIBERATI, D. LUNNEY, K. M. LYNCH, V. MANEA, B. A. MARSH, S. MITSUOKA, P. L. MOLKANOV, Y. NAGAME, D. NEIDHERR, K. NISHIO, S. OTA, D. PAUWELS, L. POPESCU, D. RADULOV, E. RAPI SARDA, J. P. REVILL, M. ROSENBUSCH, R. E. ROSSEL, S. ROTHE, K. SANDHU, L. SCHWEIKHARD, S. SELS, V. L. TRUESDALE, C. VAN BEVEREN, P. VAN DEN BERGH, P. VAN DUPPEN, Y. WAKABAYASHI, K. D. A. WENDT, F. WIENHOLTZ, B. W. WHITMORE, G. L. WILSON, R. N. WOLF, AND K. ZUBER

Inverse odd-even staggering in nuclear charge radii and possible octupole collectivity in $^{217,218,219}\text{At}$ revealed by in-source laser spectroscopy

Physical Review C **99**, 054317 (2019).

G. BECKER, M. SCHWAB, R. LÖTZSCH, S. TIETZE, D. KLÖPFEL, M. REHWALD, H.-P. SCHLENVOIGT, A. SÄVERT, U. SCHRAMM, M. ZEPF, AND M. KALUZA

Characterization of laser-driven proton acceleration from water microdroplets

Scientific Reports **9**, 17169 (2019).

R. BEERWERTH, T. BUHR, A. PERRY-SASSMANNSHAUSEN, S. O. STOCK, S. BARI, K. HOLSTE, A. L. D. KILCOYNE, S. REINWARDT, S. RICZ, D. W. SAVIN, K. SCHUBERT, M. MARTINS, A. MÜLLER, S. FRITZSCHE, AND S. SCHIPPERS

Near L-edge Single and Multiple Photoionization of Triply Charged Iron Ions

The Astrophysical Journal **887**, 189 (2019).

M. BILAL, A. V. VOLOTKA, R. BEERWERTH, J. ROTHHARDT, V. HILBERT, AND S. FRITZSCHE

High-precision calculations of the $1s^2 2s 2p \ ^1P_1 \rightarrow 1s^2 2s^2 \ ^1S_0$ spin-allowed E1 transition in C III

Physical Review A **99**, 062511 (2019).

A. BLINNE, H. GIES, F. KARBSTEIN, C. KOHLFÜRST, AND M. ZEPF

Photon-Photon Scattering at the High-Intensity Frontier: Paraxial Beams

Journal of Physics: Conference Series **1206**, 012016 (2019).

A. BLINNE, H. GIES, F. KARBSTEIN, C. KOHLFÜRST, AND M. ZEPF

The Vacuum Emission Picture Beyond Paraxial Approximation

Journal of Physics: Conference Series **1206**, 012017 (2019).

A. BLINNE, H. GIES, F. KARBSTEIN, C. KOHLFÜRST, AND M. ZEPF

All-optical signatures of quantum vacuum nonlinearities in generic laser fields

Physical Review D **99**, 016006 (2019).

A. BLINNE, S. KUSCHEL, S. TIETZE, AND M. ZEPF

Efficient retrieval of phase information from real-valued electromagnetic field data

Journal of Computational Physics: X **1**, 100019 (2019).

B. BÖNING, W. PAUFLER, AND S. FRITZSCHE

Nondipole strong-field approximation for spatially structured laser fields

Physical Review A **99**, 053404 (2019).

A. BONDAREV, Y. KOZHEDUB, I. TUPITSYN, V. SHABAEV, G. PLUNIEN, AND TH. STÖHLKER

Differential cross sections for ionization of atomic hydrogen by antiprotons

Hyperfine Interactions **240**, 60 (2019).

J. BULDT, M. MUELLER, C. JAUREGUI-MISAS, L. H. STARK, AND J. LIMPERT

Fiber-laser driven THz source based on air-plasma

Proceedings of SPIE **10897**, 52 (2019).

T. P. BUTLER, D. GERZ, C. HOFER, J. XU, C. GAIDA, T. HEUERMAN, M. GEBHARDT, L. VAMOS, W. SCHWEINBERGER, J. A. GESSNER, T. SIEFKE, M. HEUSINGER, U. ZEITNER, A. APOLONSKI, N. KARPOWICZ, J. LIMPERT, F. KRAUSZ, AND I. PUPEZA

Watt-scale 50-MHz source of single-cycle waveform-stable pulses in the molecular fingerprint region

Optics Letters **44**, 1730 (2019).

S. CREUTZBURG, E. SCHMIDT, P. KUTZA, R. LOETZSCH, I. USCHMANN, A. UNDISZ, M. RETTENMAYR, F. GALA, G. ZOLLO, A. BOULLE, A. DEBELLE, AND E. WENDLER

Defects and mechanical properties in weakly damaged Si ion implanted GaAs

Physical Review B **99**, 245205 (2019).

L. DABELOW, H. GIES, AND B. KNORR

Momentum dependence of quantum critical Dirac systems

Physical Review D **99**, 125019 (2019).

C. DANSON, C. HAEFNER, J. BROMAGE, T. BUTCHER, J.-C. CHANTELOUP, E. CHOWDHURY, A. GALVANASKAS, L. GIZZI, J. HEIN, AND D. HILLIER

Petawatt and exawatt class lasers worldwide

High Power Laser Science and Engineering **7**, E54 (2019).

J. DEPRINCE, M. A. BAUTISTA, S. FRITZSCHE, J. A. GARCÍA, T. R. KALLMAN, C. MENDOZA, P. PALMERI, AND P. QUINET

Plasma environment effects on K lines of astrophysical interest - I. Atomic structure, radiative rates, and Auger widths of oxygen ions

A&A **624**, A74 (2019).

M. DURANTE, P. INDELICATO, B. JONSON, V. KOCH, K. LANGANKE, U.-G. MEISSNER, E. NAPPI, T. NILSSON, T. STÖHLKER, E. WIDMANN, AND M. WIESCHER

All the fun of the FAIR: fundamental physics at the facility for antiproton and ion research

Physica Scripta **94**, 033001 (2019).

I. ENGIN, Z. M. CHITGAR, O. DEPERT, L. DI LUCCHIO, R. ENGELS, P. FEDORETS, S. FRYDRYCH, P. GIBBON, A. KLEINSCHMIDT, A. LEHRACH, R. MAIER, D. PRASUHN, M. ROTH, F. SCHLÜTER, C. M. SCHNEIDER, TH. STÖHLKER, K. STRATHMANN, AND M. BÜSCHER

Laser-induced acceleration of Helium ions from unpolarized gas jets

Plasma Physics and Controlled Fusion **61**, 115012 (2019).

J. FELLINGER, A. S. MAYER, G. WINKLER, W. GROSINGER, G.-W. TRUONG, S. DROSTE, C. LI, C. M. HEYL, I. HARTL, AND O. H. HECKL

Tunable dual-comb from an all-polarization-maintaining single-cavity dual-color Yb: fiber laser

Optics Express **27**, 28062 (2019).

S. FRANCHINO-VIÑAS, AND H. GIES

Propagator from nonperturbative worldline dynamics

Physical Review D **100**, 105020 (2019).

S. FRITZSCHE

A fresh computational approach to atomic structures, processes and cascades

Computer Physics Communications **240**, 1 (2019).

P. GIERSCHKE, C. JAUREGUI, T. GOTTSCHALL, AND J. LIMPERT

Relative amplitude noise transfer function of an Yb³⁺-doped fiber amplifier chain

Optics Express **27**, 17041 (2019).

H. GIES, R. SONDENHEIMER, A. UGOLOTTI, AND L. ZAMBELLI

Scheme dependence of asymptotically free solutions

The European Physical Journal C **79**, 463 (2019).

H. GIES, R. SONDENHEIMER, A. UGOLOTTI, AND L. ZAMBELLI

Asymptotic freedom in \mathbb{Z}_2 -Yukawa-QCD models

The European Physical Journal C **79**, 101 (2019).

D. A. GLAZOV, F. KÖHLER-LANGES, A. V. VOLOTKA, K. BLAUM, F. HEISSE, G. PLUNIEN, W. QUINT, S. RAU, V. M. SHABAEV, S. STURM, AND G. WERTH

g Factor of Lithiumlike Silicon: New Challenge to Bound-State QED

Physical Review Letters **123**, 173001 (2019).

D. A. GLAZOV, A. V. VOLOTKA, O. V. ANDREEV, V. P. KOSHELEVA, S. FRITZSCHE, V. M. SHABAEV, G. PLUNIEN, AND TH. STÖHLKER

Ground-state hyperfine splitting of B-like ions in the high-Z region

Physical Review A **99**, 062503 (2019).

J. GLORIUS, C. LANGER, Z. SLAVKOVSKÁ, L. BOTT, C. BRANDAU, B. BRÜCKNER, K. BLAUM, X. CHEN, S. DABABNEH, T. DAVINSON, P. ERBACHER, S. FIEBIGER, T. GASSNER, K. GÖBEL, M. GROOTHUIS, A. GUMBERIDZE, G. GYÜRKY, M. HEIL, R. HESS, R. HENSCH, P. HILLMANN, P.-M. HILLENBRAND, O. HINRICHS, B. JURADO, T. KAUSCH, A. KHODAPARAST, T. KISSELBACH, N. KLAPPER, C. KOZHUHAROV, D. KURTULGIL, G. LANE, C. LEDERER-WOODS, M. LESTINSKY, S. LITVINOV, YU. A. LITVINOV, B. LÖHER, F. NOLDEN, N. PETRIDIS, U. POPP, T. RAUSCHER, M. REED, R. REIFARTH, M. S. SANJARI, D. SAVRAN, H. SIMON, U. SPILLMANN, M. STECK, T. STÖHLKER, J. STUMM, A. SURZHYKOV, T. SZÜCS, T. T. NGUYEN, A. TAREMI ZADEH, B. THOMAS, S. YU. TORILOV, H. TÖRNQVIST, M. TRÄGER, C. TRAGESER, S. TROTSENKO, L. VARGA, M. VOLKNANDT, H. WEICK, M. WEIGAND, C. WOLF, P. J. WOODS, AND Y. M. XING

Approaching the Gamow Window with Stored Ions: Direct Measurement of $^{124}\text{Xe}(p,\gamma)$ in the ESR Storage Ring

Physical Review Letters **122**, 092701 (2019).

A. GOPAL, A. WOLDEGEORGIS, S. HERZER, AND M. ALMASSARANI

Spatiotemporal visualization of the terahertz emission during high-power laser-matter interaction

Physical Review E **100**, 053203 (2019).

A. GUMBERIDZE, D. B. THORN, A. SURZHYKOV, C. J. FONTES, B. NAJJARI, A. VOITKIV, S. FRITZSCHE, D. BANAŚ, H. F. BEYER, W. CHEN, R. E. GRISENTI, S. HAGMANN, R. HESS, P.-M. HILLENBRAND, P. INDELICATO, C. KOZHUHAROV, M. LESTINSKY, R. MÁRTIN, N. PETRIDIS, R. V. POPOV, R. SCHUCH, U. SPILLMANN, S. TASHENOV, S. TROTSENKO, A. WARCZAK, G. WEBER, W. WEN, D. F. A. WINTERS, N. WINTERS, Z. YIN, AND TH. STÖHLKER

Electron- and proton-impact excitation of heliumlike uranium in relativistic collisions

Physical Review A **99**, 032706 (2019).

S. HAGMANN, P. M. HILLENBRAND, Y. A. LITVINOV, U. SPILLMANN, AND TH. STÖHLKER

The magnetic toroidal sector as a broad-band electron-positron pair spectrometer I. lepton trajectories

Nuclear Instruments and Methods in Physics Research Section A: Accelerators, Spectrometers, Detectors and Associated Equipment **946**, 162641 (2019).

V. HANNEN, J. VOLLBRECHT, Z. ANDELKOVIC, C. BRANDAU, A. DAX, W. GEITHNER, C. GEPPERT, C. GORGES, M. HAMMEN, S. KAUFMANN, K. KÖNIG, Y. A. LITVINOV, M. LOCHMANN, B. MAASS, J. MEISNER, T. MURBÖCK, R. SÁNCHEZ, M. SCHMIDT, S. SCHMIDT, M. STECK, TH. STÖHLKER, R. C. THOMPSON, C. TRAGESER, J. ULLMANN, C. WEINHEIMER, AND W. NÖRTERSCHÄUSER

Lifetimes and g -factors of the HFS states in H-like and Li-like bismuth

Journal of Physics B: Atomic, Molecular and Optical Physics **52**, 085003 (2019).

T. HELK, M. ZÜRCH, AND C. SPIELMANN

Perspective: Towards single shot time-resolved microscopy using short wavelength table-top light sources

Structural Dynamics **6**, 010902 (2019).

S. H. HENDI, S. PANAHYAN, B. E. PANAH, AND M. JAMIL

Alternative approach to thermodynamic phase transitions

Chinese Physics C **43**, 113106 (2019).

T. HEUERMANN, M. GEBHARDT, C. GAIDA, I. PUPEZA, AND J. LIMPERT

High-power ultrafast Tm-doped fiber lasers for the generation of mid-infrared radiation in the molecular fingerprint region

Proceedings of SPIE **10897**, 16 (2019).

J. HOFBRUCKER, A. V. VOLOTKA, AND S. FRITZSCHE

Fluorescence polarization as a precise tool for understanding nonsequential many-photon ionization

Physical Review A **100**, 011401 (2019).

R. HOLLINGER, D. GUPTA, M. ZAPF, M. KARST, R. RÖDER, I. USCHMANN, U. REISLÖHNER, D. KARTASHOV, C. RONNING, AND C. SPIELMANN

Polarization dependent multiphoton absorption in ZnO thin films

Journal of Physics D: Applied Physics **53**, 055102 (2019).

R. HOLLINGER, D. GUPTA, M. ZAPF, R. RÖDER, D. KARTASHOV, C. RONNING, AND C. SPIELMANN

Single nanowire defined emission properties of ZnO nanowire arrays

Journal of Physics D: Applied Physics **52**, 295101 (2019).

R. HOLLINGER, P. MALEVICH, V. SHUMAKOVA, S. ALIŠAUSKAS, M. ZAPF, R. RÖDER, A. PUGŽLYS, A. BALTUŠKA, C. RONNING, C. SPIELMANN, AND D. KARTASHOV

Strong Light-Field Driven Nanolasers

Nano Letters **19**, 3563 (2019).

D. JAHN, D. SCHUMACHER, C. BRABETZ, F. KROLL, F. E. BRACK, J. DING, R. LEONHARDT, I. SEMMLER, A. BLAŽEVIĆ, U. SCHRAMM, AND M. ROTH

Focusing of multi-MeV, subnanosecond proton bunches from a laser-driven source

Physical Review Accelerators and Beams **22**, 011301 (2019).

O. JAHN, V. E. LESHCHENKO, P. TZALLAS, A. KESSEL, M. KRÜGER, A. MÜNZER, S. A. TRUSHIN, G. D. TSAKIRIS, S. KAHALY, D. KORMIN, L. VEISZ, V. PERVAK, F. KRAUSZ, Z. MAJOR, S. KARSCH

Towards intense isolated attosecond pulses from relativistic surface high harmonics

Optica **6**, 280 (2019).

- C. JAUREGUI-MISAS, C. STIHLER, A. TÜNNERMANN, AND J. LIMPERT
Origin and evolution of phase-shifts in high-power fiber laser systems: detailed insights into TMI
Proceedings of SPIE **10897**, 3 (2019).
- H. KANG, S. CHEN, Y. WANG, W. CHU, J. YAO, J. CHEN, X. LIU, Y. CHENG, AND Z. XU
Wavelength-dependent nonsequential double ionization of magnesium by intense femtosecond laser pulses
Physical Review A **100**, 033403 (2019).
- F. KARBSTEIN, A. BLINNE, H. GIES, AND M. ZEPF
Boosting Quantum Vacuum Signatures by Coherent Harmonic Focusing
Physical Review Letters **123**, 091802 (2019).
- F. KARBSTEIN, AND E. A. MOSMAN
X-ray photon scattering at a focused high-intensity laser pulse
Physical Review D **100**, 033002 (2019).
- F. KARBSTEIN
All-Loop Result for the Strong Magnetic Field Limit of the Heisenberg-Euler Effective Lagrangian
Physical Review Letters **122**, 211602 (2019).
- M. KIFFER, S. RINGLEB, N. STALLKAMP, B. ARNDT, I. BLINOV, S. KUMAR, S. STAHL, T. STÖHLKER, AND M. VOGEL
Single-pass non-destructive electronic detection of charged particles
Review of Scientific Instruments **90**, 113301 (2019).
- I. KISHON, A. KLEINSCHMIDT, V. SCHANZ, A. TEBARTZ, O. NOAM, J. FERNANDEZ, D. GAUTIER, R. JOHNSON, T. SHIMADA, G. WURDEN, M. ROTH, AND I. POMERANTZ
Laser based neutron spectroscopy
Nuclear Instruments and Methods in Physics Research Section A: Accelerators, Spectrometers, Detectors and Associated Equipment **932**, 27 (2019).
- A. KLENKE, M. MÜLLER, H. STARK, F. STUTZKI, C. HUPEL, T. SCHREIBER, A. TÜNNERMANN, AND J. LIMPERT
Coherent beam combination of pulses emitted by a 16-core ytterbium-doped fiber
Proceedings of SPIE **10897**, 44 (2019).
- C. KOHLFÜRST
Spin states in multiphoton pair production for circularly polarized light
Physical Review D **99**, 096017 (2019).
- J. KÖRNER, S. ZULIC, A. LUCIANETTI, D. ROSTOHAR, T. MOCEK, J. HEIN, AND M. C. KALUZA
Highly efficient, cryogenically cooled Yb:YAG q-switch laser based on a gain modulated unstable resonator design
Proceedings of SPIE **11033**, 5 (2019).
- S. KUMAR, W. QUINT, S. RINGLEB, C. P. SAFVAN, N. STALLKAMP, T. STÖHLKER, AND M. VOGEL
Properties of a cylindrical Penning trap with conical endcap openings
Physica Scripta **94**, 075401 (2019).

- B. LEI, T. TETER, J. W. WANG, V. YU. KHARIN, C. B. SCHROEDER, M. ZEPF, AND S. G. RYKOVANOV
Flexible x-ray source with tunable polarization and orbital angular momentum from Hermite-Gaussian laser modes driven plasma channel wakefield
Physical Review Accelerators and Beams **22**, 071302 (2019).
- V. E. LESHCHENKO, A. KESSEL, O. JAHN, M. KRÜGER, A. MÜNZER, S. A. TRUSHIN, L. VEISZ, Z. MAJOR, AND S. KARSCH
On-target temporal characterization of optical pulses at relativistic intensity
Light: Science & Applications **8**, 96 (2019).
- W. J. MA, I. J. KIM, J. Q. YU, I. W. CHOI, P. K. SINGH, H. W. LEE, J. H. SUNG, S. K. LEE, C. LIN, Q. LIAO, J. G. ZHU, H. Y. LU, B. LIU, H. Y. WANG, R. F. XU, X. T. HE, J. E. CHEN, M. ZEPF, J. SCHREIBER, X. Q. YAN, AND C. H. NAM
Laser Acceleration of Highly Energetic Carbon Ions Using a Double-Layer Target Composed of Slightly Underdense Plasma and Ultrathin Foil
Physical Review Letters **122**, 014803 (2019).
- F. MAES, C. STIHLER, L.-P. PLEAU, V. FORTIN, J. LIMPERT, M. BERNIER, AND R. VALLÉE
3.42 μm lasing in heavily-erbium-doped fluoride fibers
Optics Express **27**, 2170 (2019).
- I. A. MALTSEV, V. M. SHABAEV, R. V. POPOV, Y. S. KOZHEDUB, G. PLUNIEN, X. MA, T. STÖHLKER, AND D. A. TUMAKOV
How to Observe the Vacuum Decay in Low-Energy Heavy-Ion Collisions
Physical Review Letters **123**, 113401 (2019).
- M. MÜLLER, A. KLENKE, A. STEINKOPFF, E. SHESTAEV, A. TÜNNERMANN, AND J. LIMPERT
3.5 kW coherently combined ultrafast fiber laser
Proceedings of SPIE **10897**, 43 (2019).
- R. MÜLLER, A. VOLOTKA, AND A. SURZHYKOV
Excitation of the ^{229}Th nucleus via a two-photon electronic transition
Physical Review A **99**, 042517 (2019).
- T. NAGY, S. HÄDRICH, P. SIMON, A. BLUMENSTEIN, N. WALTHER, R. KLAS, J. BULDT, H. STARK, S. BREITKOPF, P. JÓJÁRT, I. SERES, Z. VÁRALLYAY, T. EIDAM, AND J. LIMPERT
Generation of three-cycle multi-millijoule laser pulses at 318 W average power
Optica **6**, 1423 (2019).
- J. NATHANAEL, M. WÜNSCHE, S. FUCHS, T. WEBER, J. J. ABEL, J. REINHARD, F. WIESNER, U. HÜBNER, S. J. SKRUSZEWICZ, G. G. PAULUS, AND C. RÖDEL
Laboratory setup for extreme ultraviolet coherence tomography driven by a high-harmonic source
Review of Scientific Instruments **90**, 113702 (2019).

W. NÖRTERSCHÄUSER, J. ULLMANN, L. V. SKRIPNIKOV, Z. ANDELKOVIC, C. BRANDAU, A. DAX, W. GEITHNER, C. GEPPERT, C. GORGES, M. HAMMEN, V. HANNEN, S. KAUFMANN, K. KÖNIG, F. KRAUS, B. KRESSE, Y. A. LITVINOV, M. LOCHMANN, B. MAASS, J. MEISNER, T. MURBÖCK, A. F. PRIVALOV, R. SÁNCHEZ, B. SCHEIBE, M. SCHMIDT, S. SCHMIDT, V. M. SHABAEV, M. STECK, T. STÖHLKER, R. C. THOMPSON, C. TRAGESER, M. VOGEL, J. VOLLBRECHT, A. V. VOLOTKA, AND C. WEINHEIMER

The hyperfine puzzle of strong-field bound-state QED

Hyperfine Interactions **240**, 51 (2019).

J. B. OHLAND, U. EISENBARTH, M. ROTH, AND V. BAGNOUD

A study on the effects and visibility of low-order aberrations on laser beams with orbital angular momentum

Applied Physics B **32**, 56 (2019).

F. OZTURK, B. AKKUS, D. ATANASOV, H. BEYER, F. BOSCH, D. BOUTIN, C. BRANDAU, P. BÜHLER, R. CAKIRLI, R. CHEN, W. CHEN, X. CHEN, I. DILLMANN, C. DIMOPOULOU, W. ENDERS, H. ESSEL, T. FAESTERMANN, O. FORSTNER, B. GAO, H. GEISSEL, R. GERNHÄUSER, R. GRISENTI, A. GUMBERIDZE, S. HAGMANN, T. HEFTRICH, M. HEIL, M. HERDRICH, P.-M. HILLENBRAND, T. IZUMIKAWA, P. KIENLE, C. KLAUSHOFER, C. KLEFFNER, C. KOZHUHAROV, R. KNÖBEL, O. KOVALENKO, S. KREIM, T. KÜHL, C. LEDERER-WOODS, M. LESTINSKY, S. LITVINOV, Y. LITVINOV, Z. LIU, X. MA, L. MAIER, B. MEI, H. MIURA, I. MUKHA, A. NAJAFI, D. NAGAE, T. NISHIMURA, C. NOCIFORO, F. NOLDEN, T. OHTSUBO, Y. OKTEM, S. OMIKA, A. OZAWA, N. PETRIDIS, J. PIOTROWSKI, R. REIFARTH, J. ROSSBACH, R. SÁNCHEZ, M. SANJARI, C. SCHEIDENBERGER, R. SIDHU, H. SIMON, U. SPILLMANN, M. STECK, TH. STÖHLKER, B. SUN, L. SUSAM, F. SUZAKI, T. SUZUKI, S. TORILOV, C. TRAGESER, M. TRASSINELLI, S. TROTSENKO, X. TU, P. WALKER, M. WANG, G. WEBER, H. WEICK, N. WINCKLER, D. WINTERS, P. WOODS, T. YAMAGUCHI, X. XU, X. YAN, J. YANG, Y. YUAN, Y. ZHANG, AND X. ZHOU

New test of modulated electron capture decay of hydrogen-like ^{142}Pm ions: Precision measurement of purely exponential decay

Physics Letters B **797**, 134800 (2019).

B. E. PANAH, S. PANAHYAN, AND S. H. HENDI

Entropy spectrum of charged BTZ black holes in massive gravity's rainbow

Progress of Theoretical and Experimental Physics **2019**, 013E02 (2019).

S. PANAHYAN, AND S. FRITZSCHE

Simulation of the multiphase configuration and phase transitions with quantum walks utilizing a step-dependent coin

Physical Review A **100**, 062115 (2019).

S. PANAHYAN, S. H. HENDI, AND N. RIAZI

AdS_4 dyonic black holes in gravity's rainbow

Nuclear Physics B **938**, 388 (2019).

W. PAUFLER, B. BÖNING, AND S. FRITZSCHE

Coherence control in high-order harmonic generation with Laguerre-Gaussian beams

Physical Review A **100**, 013422 (2019).

W. PAUFLER, B. BÖNING, AND S. FRITZSCHE

High harmonic generation with Laguerre-Gaussian beams

Journal of Optics **21**, 094001 (2019).

A. A. PESHKOV, S. FRITZSCHE, AND A. SURZHYKOV

Scattering of twisted light from a crystal

Physica Scripta **94**, 105402 (2019).

W. PLACZEK, A. ABRAMOV, S. ALDEN, R. ALEMANY FERNANDEZ, P. ANTSIFEROV, A. APYAN, H. BARTOSIK, E. BESSONOV, N. BIANCACCI, J. BIERON, A. BOGACZ, A. BOSCO, R. BRUCE, D. BUDKER, K. CASSOU, F. CASTELLI, I. CHAIKOVSKA, C. CURATOLO, P. CZODROWSKI, A. DEREVIANKO, K. DUPRAZ, Y. DUTHEIL, K. DZIERZCEGA, V. FEDOSSEEV, N. FUSTER MARTINEZ, S. GIBSON, B. GODDARD, A. GORZAWSKI, S. HIRLANDER, J. JOWETT, R. KERSEVAN, M. KOWALSKA, M. KRASNY, F. KROEGER, M. LAMONT, T. LEFEVRE, D. MANGLUNKI, B. MARSH, A. MARTENS, J. MOLSON, D. NUTARELLI, L. NEVAY, A. PETRENKO, V. PETRILLO, S. RADAELLI, S. PUSTELNY, S. ROCHESTER, M. SAPINSKI, M. SCHAUMANN, L. SERAFINI, V. SHEVELKO, T. STOEHLKER, A. SURZHYKOV, I. TOLSTIKHINA, F. VELOTTI, G. WEBER, Y. WU, C. YIN-VALLGREN, M. ZANETTI, F. ZIMMERMANN, M. ZOLOTOREV, AND F. ZOMER

Gamma Factory at CERN - Novel Research Tools Made of Light

Acta Physica Polonica B **50**, 1191 (2019).

P. POLYNKIN, Z. SAMSONOVA, A. ENGLSBE, A. LUCERO, J. ELLE, AND A. SCHMITT-SODY

Channeling the dielectric breakdown of air by a sequence of laser-generated plasma filaments

Journal of the Optical Society of America B **36**, 3024 (2019).

J. POLZ, A. P. L. ROBINSON, A. KALININ, G. A. BECKER, R. FRAGA, M. HELLWING, M. HORNING, S. KEPPLER, A. KESSLER, D. KLÖPFEL, H. LIEBETRAU, F. SCHORCHT, J. HEIN, M. ZEPF, R. E. GRISENTI, AND M. C. KALUZA

Efficient Laser-Driven Proton Acceleration from a Cryogenic Solid Hydrogen Target

Scientific Reports **9**, 16534 (2019).

Z. SAMSONOVA, S. HÖFER, V. KAYMAK, S. ALIŠAUSKAS, V. SHUMAKOVA, A. PUGŽLYS, A. BALTUŠKA, T. SIEFKE, S. KROKER, A. PUKHOV, O. ROSMEJ, I. USCHMANN, C. SPIELMANN, AND D. KARTASHOV

Relativistic Interaction of Long-Wavelength Ultrashort Laser Pulses with Nanowires

Physical Review X **9**, 021029 (2019).

T. SAULE, S. HEINRICH, J. SCHÖTZ, N. LILIENFEIN, M. HÖGNER, O. DEVRIES, M. PLÖTNER, J. WEITENBERG, D. ESSER, J. SCHULTE, P. RUSSBUELDT, J. LIMPET, M. F. KLING, U. KLEINEBERG, AND I. PUPEZA

High-flux ultrafast extreme-ultraviolet photoemission spectroscopy at 18.4 MHz pulse repetition rate

Nature Communications **10**, 458 (2019).

H. SAWADA, Y. SENTOKU, T. YABUCHI, U. ZASTRAU, E. FÖRSTER, F. N. BEG, H. CHEN, A. J. KEMP, H. S. McLEAN, P. K. PATEL, AND Y. PING

Monochromatic 2D $K\alpha$ Emission Images Revealing Short-Pulse Laser Isochoric Heating Mechanism

Physical Review Letters **122**, 155002 (2019).

V. A. SCHANZ, C. BRABETZ, D. J. POSOR, D. REEMTS, M. ROTH, AND V. BAGNOUD

High dynamic range, large temporal domain laser pulse measurement

Applied Physics B **125**, 61 (2019).

V. A. SCHANZ, M. ROTH, AND V. BAGNOUD

Picosecond contrast degradation by surface imperfections in chirped-pulse-amplification stretchers

Journal of the Optical Society of America A **36**, 1735 (2019).

D. N. SCHIMPF, H. T. OLGUN, A. KALAYDZHIAN, Y. HUA, N. H. MATLIS, AND F. X. KÄRTNER

Frequency-comb-based laser system producing stable optical beat pulses with picosecond durations suitable for high-precision multi-cycle terahertz-wave generation and rapid detection

Optics Express **27**, 11037 (2019).

L. SCHMIDL, G. SCHMIDL, A. GAWLIK, J. DELLITH, U. HÜBNER, V. TYMPEL, F. SCHMIDL, J. PLENTZ, C. GEIS, AND H. HASELMANN

Combining super-resolution microscopy with neuronal network recording using magnesium fluoride thin films as cover layer for multi-electrode array technology

Scientific Reports **9**, 16110 (2019).

S.-L. SCHULZ, S. FRITZSCHE, R. A. MÜLLER, AND A. SURZHYKOV

Modification of multipole transitions by twisted light

Physical Review A **100**, 043416 (2019).

J.-P. SCHWINKENDORF, S. BOHLEN, J. P. COUPERUS CABADAĞ, H. DING, A. IRMAN, S. KARSCH, A. KÖHLER, J. M. KRÄMER, T. KURZ, S. KUSCHEL, J. OSTERHOFF, L. F. SCHAPER, D. SCHINKEL, U. SCHRAMM, O. ZARINI, AND R. D'ARCY

Charge calibration of DRZ scintillation phosphor screens

Journal of Instrumentation **14**, P09025 (2019).

D. SEIPT, V. KHARIN, AND S. RYKOVANOV

Optimizing Laser Pulses for Narrow-Band Inverse Compton Sources in the High-Intensity Regime

Physical Review Letters **122**, 204802 (2019).

X. F. SHEN, B. QIAO, H. ZHANG, Y. XIE, S. KAR, M. BORGHESI, M. ZEPF, C. T. ZHOU, S. P. ZHU, AND X. T. HE

Electrostatic capacitance-type acceleration of ions with an intense few-cycle laser pulse

Applied Physics Letters **114**, 144102 (2019).

E. SHESTAEV, C. GAIDA, T. HEUERMAN, M. GEBHARDT, T. BUTLER, D. GERZ, N. LILIENFEIN, P. SULZER, M. FISCHER, R. HOLZWAR, A. LEITENSTORFER, I. PUPEZA, AND J. LIMPET

High power frequency comb delivered by a Tm-doped fiber laser

Proceedings of SPIE **10897**, 17 (2019).

H. STARK, J. BULDT, M. MÜLLER, A. KLENKE, A. TÜNNERMANN, AND J. LIMPET

23 mJ high-power fiber CPA system using electro-optically controlled divided-pulse amplification

Optics Letters **44**, 5529 (2019).

H. STARK, J. BULDT, M. MUELLER, A. KLENKE, A. TÜNNERMANN, AND J. LIMPET

High-power electro-optically controlled divided-pulse amplification

Proceedings of SPIE **10897**, 45 (2019).

A. STEINKOPFF, C. JAUREGUI, F. STUTZKI, J. NOLD, C. HUPEL, N. HAARLAMMERT, J. BIERLICH, A. TÜNNERMANN, AND J. LIMPERS

Transverse single-mode operation in a passive large pitch fiber with more than 200 μm mode-field diameter

Optics Letters **44**, 650 (2019).

A. STEINKOPFF, C. JAUREGUI-MISAS, F. STUTZKI, J. NOLD, C. HUPEL, N. HAARLAMMERT, J. BIERLICH, A. TÜNNERMANN, AND J. LIMPERS

Single-mode propagation with 205 μm mode-field diameter in a passive large pitch fiber

Proceedings of SPIE **10897**, 31 (2019).

C. STIHLER, C. JAUREGUI-MISAS, A. TÜNNERMANN, AND J. LIMPERS

The impact of pump-power noise on transverse mode instabilities

Proceedings of SPIE **10897**, 2 (2019).

L. STOYANOV, G. MALESHKOV, M. ZHEKOVA, I. STEFANOV, G. G. PAULUS, AND A. DREISCHUH

Controllable beam reshaping by mixing square-shaped and hexagonal optical vortex lattices

Scientific Reports **9**, 2128 (2019).

L. STOYANOV, G. MALESHKOV, M. ZHEKOVA, I. STEFANOV, G. G. PAULUS, AND A. DREISCHUH

Multi-spot focal pattern formation and beam reshaping by mixing square-shaped and hexagonal vortex lattices

Proceedings of SPIE **11332**, 18 (2019).

Z. SUN, F. TUITJE, AND C. SPIELMANN

Toward high contrast and high-resolution microscopic ghost imaging

Optics Express **27**, 33652 (2019).

J. SZERYPO, W. MA, G. BOTHMANN, D. HAHNER, M. HAUG, P. HILZ, CH. KREUZER, R. LANGE, S. SEUFERLING, M. SPEICHER, F. STEHR, S. STORK, P. G. THIROLF, J. SCHREIBER, AND H.-F. WIRTH

Target fabrication for laser-ion acceleration research at the Technological Laboratory of the LMU Munich

Matter and Radiation at Extremes **4**, 035201 (2019).

G. TADESSE, W. ESCHEN, R. KLAS, M. TSCHERNAJEV, T. FREDERIK, M. STEINERT, M. ZILK, V. SCHUSTER, M. ZÜRCH, T. PERTSCH, C. SPIELMANN, J. LIMPERS, AND J. ROTHHARDT

Wavelength-scale ptychographic coherent diffractive imaging using a high-order harmonic source

Scientific Reports **9**, 1735 (2019).

I. TAMER, S. KEPPLER, J. KÖRNER, M. HORNING, M. HELLWING, F. SCHORCHT, J. HEIN, AND M. KALUZA

Modeling of the 3D spatio-temporal thermal profile of joule-class Yb^{3+} -based laser amplifiers

High Power Laser Science and Engineering **7**, E42 (2019).

G. TORGRIMSSON

Perturbative methods for assisted nonperturbative pair production

Physical Review D **99**, 096002 (2019).

G. TORGRIMSSON

Thermally versus dynamically assisted Schwinger pair production

Physical Review D **99**, 096007 (2019).

F. TUITJE, T. HELK, M. ZÜRCH, AND C. SPIELMANN

Extreme ultraviolet lensless imaging of biological specimen

Proceedings of SPIE **10890**, 80 (2019).

F. TUITJE, T. HELK, M. ZÜRCH, J. GAUTIER, F. TISSANDIER, J.-P. GODDET, E. OLIVA, A. GUGGENMOS, U. KLEINEBERG, S. SEBBAN, AND C. SPIELMANN

Following the plasma dynamics in a seeded soft x-ray laser with lensless imaging

Proceedings of SPIE **10903**, 9 (2019).

M. VOCKERT, G. WEBER, H. BRÄUNING, A. SURZHYKOV, C. BRANDAU, S. FRITZSCHE, S. GEYER, S. HAGMANN, S. HESS, C. KOZHUHAROV, R. MÄRTIN, N. PETRIDIS, R. HESS, S. TROTSENKO, YU. A. LITVINOV, J. GLORIUS, A. GUMBERIDZE, M. STECK, S. LITVINOV, T. GASSNER, P.-M. HILLENBRAND, M. LESTINSKY, F. NOLDEN, M. S. SANJARI, U. POPP, C. TRAGESER, D. F. A. WINTERS, U. SPILLMANN, T. KRINGS, AND TH. STÖHLKER

Radiative electron capture as a tunable source of highly linearly polarized x rays

Physical Review A **99**, 052702 (2019).

A. V. VOLOTKA, M. BILAL, R. BEERWERTH, X. MA, TH. STÖHLKER, AND S. FRITZSCHE

QED radiative corrections to the $^2P_{1/2}$ - $^2P_{3/2}$ fine structure in fluorinelike ions

Physical Review A **100**, 010502 (2019).

A. WALLNER, M. BICHLER, L. COQUARD, I. DILLMANN, O. FORSTNER, R. GOLSER, M. HEIL, F. KÄPPELER, W. KUTSCHERA, C. LEDERER-WOODS, M. MARTSCHINI, A. MENGONI, S. MERCHEL, L. MICHLMAYR, A. PRILLER, P. STEIER, AND M. WIESCHER

Stellar and thermal neutron capture cross section of ^9Be

Physical Review C **99**, 015804 (2019).

J. W. WANG, M. ZEPF, AND S. RYKOVANOV

Intense attosecond pulses carrying orbital angular momentum using laser plasma interactions

Nature Communications **10**, 5554 (2019).

M. K. WEIKUM, T. AKHTER, D. ALESINI, A. S. ALEXANDROVA, M. P. ANANIA, N. E. ANDREEV, I. A. ANDRIYASH, A. ASCHIKHIN, R. W. ASSMANN, T. AUDET, A. BACCI, I. F. BARNA, A. BEATON, A. BECK, A. BELUZE, A. BERNHARD, S. BIELAWSKI, F. G. BISESTO, F. BRANDI, R. BRINKMANN, E. BRUENDERMANN, M. BÜSCHER, M. H. BUSSMANN, G. BUSSOLINO, A. CHANCE, M. CHEN, E. CHIADRONI, A. CIANCHI, J. A. CLARKE, J. COLE, M. E. COUPRIE, M. CROIA, B. CROS, P. A. CRUMP, G. DATTOLI, A. DEL DOTTO, N. DELERUE, S. DE NICOLA, J. M. DIAS, U. DORDA, R. FEDELE, A. FERRAN POUSA, M. FERRARIO, F. FILIPPI, G. FIORE, R. A. FONSECA, M. GALIMBERTI, A. GALLO, A. GHAITH, D. GIOVE, A. GIRIBONO, L. A. GIZZI, F. J. GRÜNER, A. F. HABIB, C. HAEFNER, T. HEINEMANN, B. HIDDING, B. J. HOLZER, S. M. HOOKER, T. HOSOKAI, M. HUEBNER, A. IRMAN, F. J. AFARINIA, D. A. JAROSZYNSKI, C. JOSHI, M. KALUZA, M. KANDO, O. S. KARGER, S. KARSCH, E. KHAZANOV, D. KHIKHLUKHA, A. KNETSCH, D. KOCON, P. KOESTER, O. S. KONONENKO, G. KORN, I. KOSTYUKOV, K. O. KRUCHININ, L. LABATE, C. LE BLANC, C. LECHNER, W. LEEMANS, A. LEHRACH, X. LI, V. LIBOV, A. LIFSCHITZ, V. LITVINENKO, W. LU, O. LUNDH, A. R. MAIER, V. MALKA, G. G. MANAHAN, S. P. D. MANGLES, B. MARCHETTI, A. MARTINEZ DE LA OSSA, J. L. MARTINS, P. D. MASON, F. MASSIMO, F. MATHIEU, G. MAYNARD, Z. MAZZOTTA, A. Y. MOLODOZHENTSEV, A. MOSTACCI, A.-S. MUELLER, C. D. MURPHY, Z. NAJMUDIN, P. A. P. NGHIEM, F. NGUYEN, P. NIKNEJADI, J. OSTERHOFF, D. OUMBAREK ESPINOS, D. N. PAPADOPOULOS, B. PATRIZI, V. PETRILLO, M. A. POCSAI, K. PODER, R. POMPILI, L. PRIBYL, D. PUGACHEVA, P. P. RAJEEV, S. ROMEO, M. ROSSETTI CONTI, A. R. ROSSI, R. ROSSMANITH, E. ROUSSEL, A. A. SAHAI, G. SARRI, L. SCHAPER, P. SCHERKL, U. SCHRAMM, C. B. SCHROEDER, J. SCIFO, L. SERAFINI, Z. M. SHENG, C. SIDERS, S. O. SILVA, T. SILVA, C. SIMON, U. SINHA, A. SPECKA, M. J. V. STREETER, E. N. SVYSTUN, D. SYMES, C. SZWAJ, G. E. TAUSCHER, D. TERZANI, N. THOMPSON, G. TOCI, P. TOMASSINI, R. TORRES, D. ULLMANN, C. VACCAREZZA, M. VANNINI, J. M. VIEIRA, F. VILLA, C.-G. WAHLSTROM, R. WALCZAK, P. A. WALKER, K. WANG, C. P. WELSCH, S. M. WIGGINS, J. WOLFENDEN, G. XIA, M. YABASHI, J. ZHU, AND A. ZIGLER

Status of the Horizon 2020 EuPRAXIA conceptual design study

Journal of Physics: Conference Series **1350**, 012059 (2019).

A. WOLDEGEORGIS, S. HERZER, M. ALMASSARANI, S. MARATHAPALLI, AND A. GOPAL

Modeling terahertz emission from the target rear side during intense laser-solid interactions

Physical Review E **100**, 053204 (2019).

D. WU, W. YU, S. FRITZSCHE, AND X. T. HE

High-order implicit particle-in-cell method for plasma simulations at solid densities

Physical Review E **100**, 013207 (2019).

D. WU, W. YU, Y. T. ZHAO, D. H. H. HOFFMANN, S. FRITZSCHE, AND X. T. HE

Particle-in-cell simulation of transport and energy deposition of intense proton beams in solid-state materials

Physical Review E **100**, 013208 (2019).

D. WU, W. YU, S. FRITZSCHE, C. Y. ZHENG, AND X. T. HE

Formation of relativistic electromagnetic solitons in over-dense plasmas

Physics of Plasmas **26**, 063107 (2019).

M. WÜNSCHE, S. FUCHS, T. WEBER, J. NATHANAEL, J. J. ABEL, J. REINHARD, F. WIESNER, U. HÜBNER, S. S. SKRUSZEWICZ, G. G. PAULUS, AND C. RÖDEL

A high resolution extreme ultraviolet spectrometer system optimized for harmonic spectroscopy and XUV beam analysis

Review of Scientific Instruments **90**, 023108 (2019).

- Y. S. YOU, J. LU, E. F. CUNNINGHAM, C. RÖDEL, AND S. GHIMIRE
Crystal orientation-dependent polarization state of high-order harmonics
Optics Letters **44**, 530 (2019).
- F. YUE, V. JAMBUNATHAN, S. P. DAVID, J. REITER, J. KÖRNER, D. KLÖPFEL, J. HEIN, M. C. KALUZA, A. LUCIANETTI, AND T. MOCEK
Diode-pumped cryogenic Tm:LiYF₄ laser
Proceedings of SPIE **11033**, 11 (2019).
- V. ZAKOSARENKO, M. SCHMELZ, T. SCHÖNAU, S. ANDERS, J. KUNERT, V. TYMPEL, R. NEUBERT, F. SCHMIDL, P. SEIDEL, TH. STÖHLKER, D. HAIDER, M. SCHWICKERT, T. SIEBER, AND R. STOLZ
Coreless SQUID-based cryogenic current comparator for non-destructive intensity diagnostics of charged particle beams
Superconductor Science and Technology **32**, 014002 (2019).
- V. A. ZAYTSEV, A. V. VOLOTKA, D. YU, S. FRITZSCHE, X. MA, H. HU, AND V. M. SHABAEV
Ab initio QED Treatment of the Two-Photon Annihilation of Positrons with Bound Electrons
Physical Review Letters **123**, 093401 (2019).
- M. ZHEKOVA, G. MALESHKOV, L. STOYANOV, I. STEFANOV, G. G. PAULUS, AND A. DREISCHUH
Formation of multi-spot focal arrays by square-shaped optical vortex lattices
Optics Communications **449**, 110 (2019).
- N. A. ZUBOVA, I. S. ANISIMOVA, M. Y. KAYGORODOV, Y. S. KOZHEDUB, A. V. MALYSHEV, V. M. SHABAEV, I. I. TUPITSYN, G. PLUNIEN, C. BRANDAU, AND T. STÖHLKER
Isotope shifts of the $1s^2 2s 2p$ (J)– $1s^2 2s^2$ transition energies in Be-like thorium and uranium
Journal of Physics B: Atomic, Molecular and Optical Physics **52**, 185001 (2019).

Theses

R. BEERWERTH

Electron Correlation in Relativistic Multiconfiguration Calculations of Isotope Shift Parameters, Hyperfine Coupling Constants and Atomic Processes

Dissertation

Friedrich-Schiller-Universität Jena, Physikalisch-Astronomische Fakultät, (2019).

B. LEI

High energy radiation from compact plasma-based sources

Dissertation

Friedrich-Schiller-Universität Jena, Physikalisch-Astronomische Fakultät, (2019).

M. BILAL

High precision many-electron calculations for multiply-charged ions

Dissertation

Friedrich-Schiller-Universität Jena, Physikalisch-Astronomische Fakultät, (2019).

M. MÄUSEZAHL

Untersuchung lasergetriebener Protonenbeschleunigung bezüglich Vorplasmaerzeugung und räumlicher Protonendetektion

Master thesis

Friedrich-Schiller-Universität Jena, Physikalisch-Astronomische Fakultät, (2019).

G. TADESSE

Nanoscale Coherent Diffractive Imaging using High-harmonic XUV Sources

Dissertation

Friedrich-Schiller-Universität Jena, Physikalisch-Astronomische Fakultät, (2019).

D. WÜRZLER

Untersuchung und Simulation der Ionisations- und Streudynamik von Photoelektronen mithilfe von Zwei-Farben-Feldern

Dissertation

Friedrich-Schiller-Universität Jena, Physikalisch-Astronomische Fakultät, (2019).

R. A. MÜLLER

Investigation of Atomic Nuclei via Electronic Processes

Dissertation

Technische Universität Carolo-Wilhelmina zu Braunschweig, Fakultät für Elektrotechnik, Informationstechnik, Physik, (2019).

D. HOFF

Elektronendynamik in fokussierten Einzelzyklenpulsen

Dissertation

Friedrich-Schiller-Universität Jena, Physikalisch-Astronomische Fakultät, (2019).

P. LUCKNER

Entwicklung, Aufbau und Charakterisierung eines optischen, hochgenauen Target-Positioniersystems

Bachelor thesis

Ernst-Abbe-Hochschule Jena, Fachbereich Feinwerktechnik, (2019).

Z. SAMSONOVA

Relativistic interaction of ultra-short laser pulses with nanostructured solids

Dissertation

Friedrich-Schiller-Universität Jena, Physikalisch-Astronomische Fakultät, (2019).

P. WUSTELT

Atome und Moleküle fundamentaler Bedeutung in intensiven Laserfeldern: He, He⁺ und HeH⁺

Dissertation

Friedrich-Schiller-Universität Jena, Physikalisch-Astronomische Fakultät, (2019).

E. MENZ

A Scintillation Particle Detector for Recombination Experiments at CRYRING@ESR

Master thesis

Friedrich-Schiller-Universität Jena, Physikalisch-Astronomische Fakultät, (2019).

H. BERNHARDT

Hochpräzise Röntgenpolarimetrie mit Diamantkristallen

Dissertation

Friedrich-Schiller-Universität Jena, Physikalisch-Astronomische Fakultät, (2019).